

Cover Page



Universiteit Leiden



The handle <http://hdl.handle.net/1887/22339> holds various files of this Leiden University dissertation.

Author: Szomoru, Daniel

Title: The extraordinary structural evolution of massive galaxies

Issue Date: 2013-11-21

THE EXTRAORDINARY STRUCTURAL EVOLUTION OF MASSIVE GALAXIES

PROEFSCHRIFT

ter verkrijging van
de graad van Doctor aan de Universiteit Leiden,
op gezag van Rector Magnificus prof. mr. C. J. J. M. Stolker,
volgens besluit van het College voor Promoties
te verdedigen op donderdag 21 november 2013
klokke 11:15 uur

door

Daniel Szomoru
geboren te Rehovot (Israel)
in 1983

Promotiecommissie

Promotores:

Prof. dr. M. Franx
Prof. dr. P. G. van Dokkum (Yale University, USA)

Overige leden:

Prof. dr. H. J. A. Röttgering
Prof. dr. J. Schaye
Prof. dr. S. Portegies-Zwart
Dr. I. Labbé
Dr. T. Naab (Max Planck Institut für Astrophysik, Duitsland)

TABLE OF CONTENTS

Nederlandse samenvatting	5
1 Introduction	9
1.1 Extragalactic astronomy	9
1.2 The Universe at $z = 0$	9
1.3 Moving to high redshift	10
1.4 Current issues	12
1.5 This thesis	13
2 Confirmation of the compactness of a $z = 1.91$ quiescent galaxy with HST/WFC3	17
2.1 Introduction	18
2.2 Observations and sample	19
2.3 Fitting and size	19
2.4 Low surface brightness sensitivity	22
2.5 Discussion	22
3 Morphological evolution of galaxies from ultradeep HST WFC3 imaging: the Hubble sequence at $z \sim 2$.	29
3.1 Introduction	30
3.2 Morphologies at $z \sim 2$	31
3.3 Color gradients at $z \sim 2$	33
3.4 The Hubble sequence from $z \sim 2$ to $z = 0$	35
3.5 Discussion	36
4 Sizes and surface brightness profiles of quiescent galaxies at $z \sim 2$	41
4.1 Introduction	42
4.2 Data and sample selection	43
4.3 Measuring surface brightness profiles	46
4.4 Missing flux in compact quiescent $z \sim 2$ galaxies	49
4.5 The mass growth of $z \sim 2$ quiescent galaxies	52
4.6 Summary and conclusions	57

5	The stellar mass structure of massive galaxies from $z = 0$ to $z = 2.5$; surface density profiles and half-mass radii	61
5.1	Introduction	62
5.2	Data and sample selection	63
5.3	Analysis	64
5.4	Mass-weighted sizes	68
5.5	Summary and conclusions	77
6	Insights into galaxy size growth from semi-analytic models	81
6.1	Introduction	82
6.2	Galaxy sizes in semi-analytic models	83
6.3	Galaxy selection	84
6.4	Galaxy growth	86
6.5	The fate of quenched galaxies	91
6.6	Conclusions	95
	Conclusions	99
	Curriculum vitae	101
	Acknowledgements	103

NEDERLANDSE SAMENVATTING

Sinds het ontstaan van de moderne sterrenkunde hebben observaties van verre sterrenstelsels een grote rol gespeeld in het testen van kosmologische modellen en in het blootleggen van gebreken in ons begrip van het heelal. Sterrenstelsels volgen de verdeling van (donkere) materie in het heelal, en kunnen daarom gebruikt worden om informatie te verkrijgen over de inhoud van het heelal. Ze worden omringd door grote hoeveelheden gas, donkere materie, en kleine satellietstelsels; in feite fungeren ze als vuurtorens die de drukke gebieden in het heelal aangeven. Omdat ze gevoelig zijn voor een grote variëteit aan fysieke processen vervullen ze een rol als kosmische laboratoria, waar deze processen in detail kunnen worden bestudeerd.

Vroege klassificaties van sterrenstelsels in de buurt van onze Melkweg waren grotendeels gebaseerd op het uiterlijk van deze stelsels. Sterrenstelsels kunnen grofweg worden opgedeeld in platte schijfstelsels aan de ene kant, en bolvormige ("elliptische") stelsels aan de andere kant. Tussen deze twee extremen ligt een verscheidenheid aan tussenvormen die een combinatie van een schijfcomponent en een bolcomponent bevatten. Al sinds lange tijd is het duidelijk dat de structuur van een sterrenstelsel sterk samenhangt met het soort sterren in het stelsel; schijfstelsels vormen over het algemeen veel nieuwe sterren, terwijl elliptische stelsels overwegend oude sterren bevatten. Correlaties tussen de verschillende eigenschappen van sterrenstelsels kunnen waardevolle informatie geven over de processen die hebben bijgedragen aan hun vorming.

Observaties van de huidige staat van sterrenstelsels geven echter een onvolledig beeld; het heelal bestaat immers al bijna 14 miljard jaar. Om het ontstaan en de groei van sterrenstelsels te kunnen begrijpen is het daarom belangrijk om ook naar het vroege heelal te kijken. Sinds een paar decennia is het mogelijk om dit op grote schaal te doen. In die tijd is duidelijk geworden dat sterrenstelsels tijdens hun leven behoorlijk wat veranderingen ondergaan, bijvoorbeeld door nieuwe sterren te vormen of door te botsen met andere sterrenstelsels. Deze processen hebben veel invloed op de structuur van sterrenstelsels en op hun inhoud (bijvoorbeeld de verhouding tussen gas en sterren, of de hoeveelheid zware elementen).

Verre sterrenstelsels zijn moeilijk te bestuderen; vanwege hun grote afstand lijken ze erg klein en zijn ze lichtzwak. Zeer gevoelige detectoren met hoge resolutie zijn nodig om nauwkeurige metingen te kunnen maken, en zelfs dan zijn de resultaten erg gevoelig voor fouten. Het hoofdthema van dit proefschrift - de groei van sterrenstelsels in de laatste 10 miljard jaar - heeft al een aantal jaren veel aandacht gekregen, omdat de snelheid waarmee stelsels lijken te groeien veel groter is dan in eerste instantie was verwacht. Vooral de snelle groei van "passieve" sterrenstelsels, waarin vrijwel geen nieuwe sterren worden gevormd, heeft veel vragen opgeroepen: hoe kunnen deze stelsels zo snel groeien? Hoe past dit in ons idee van structuurvorming in het heelal, en hoe is deze groei gekoppeld aan kosmologische veranderingen? Maar even belangrijk is de vraag: kloppen de observaties wel, en weten we

eigenlijk wat we precies meten?

Het onderzoek dat in dit proefschrift is beschreven is hoofdzakelijk uitgevoerd met data van de Wide Field Camera 3 (WFC3), een nabij-infrarood-detector op de Hubble Space Telescope. Dit instrument is gevoelig voor licht met golflengtes tussen 1000 - 2000 nanometer. Dit is van belang omdat het licht van verre sterrenstelsels zo sterk wordt roodverschoven (vergelijkbaar met het Doppler-effect voor geluid), dat gewone detectoren maar een beperkt deel van het licht van deze stelsels kunnen detecteren. Sinds de montage van WFC3 op de Hubble Space Telescope zijn er een aantal grote observatieprogramma's mee uitgevoerd, waarvan de data vrij te verkrijgen is. In dit proefschrift wordt uitvoerig gebruik gemaakt van deze data, met name van de allerdiepste opnames.

In dit proefschrift worden drie onderwerpen behandeld. Allereerst wordt gekeken naar de groottes van passieve sterrenstelsels, en de veranderingen tussen nu en 10 miljard jaar geleden. Vanwege de grote afstand tussen ons en de vroegste sterrenstelsels is het zeer moeilijk om betrouwbare metingen te doen. Met name de groottes van deze stelsels zouden door meerdere effecten kunnen worden onderschat. Uit het onderzoek in dit proefschrift blijkt dat dit niet het geval is, en dat sterrenstelsels in het vroege heelal gemiddeld bijna 4 keer zo klein waren als vergelijkbare stelsels nu zijn. Echter, in veel opzichten waren passieve sterrenstelsels 10 miljard jaar geleden al heel vergelijkbaar met huidige stelsels: ze waren bolvormig, hadden een egale verdeling van sterren, en produceerden vrijwel geen nieuwe sterren. De structuur van de kernen van huidige elliptische stelsels toont sterke overeenkomsten met vroegere elliptische stelsels. Dit suggereert dat deze stelsels van binnen naar buiten groeien; gedurende hun leven trekken ze materiaal uit hun omgeving aan, dat als uien schillen rondom de oude kern komt te liggen.

Ten tweede wordt op een meer algemene manier gekeken naar het vroege heelal, door de structuur van alle soorten sterrenstelsels te bestuderen - zowel stervormende als passieve stelsels. De correlaties die in het nabije universum zo bekend zijn blijken vroeg in het heelal al tot stand te zijn gekomen. De actiefst stervormende stelsels waren 10 miljard jaar geleden ook al blauwer, groter, en meer schijfvormig dan passieve stelsels. Het belangrijkste resultaat van dit deel van het proefschrift is dat sterrenstelsels - zowel vroeger als nu - vrijwel altijd relatief rode kernen hebben. Dit betekent dat de oudste sterren altijd in het centrale gedeelte van sterrenstelsels liggen, en ondersteunt het idee dat de kernen van sterrenstelsels vroeg ontstaan, waarna extra materiaal er geleidelijk omheen komt te liggen.

Dit resultaat heeft belangrijke consequenties voor de structuur van sterrenstelsels. Om de opbouw van sterrenstelsels goed te begrijpen is het belangrijk om te weten hoe de massadistributie binnen sterrenstelsels eruit ziet. Jonge sterren stralen over het algemeen meer licht uit dan oude sterren, maar dragen niet evenveel bij aan de totale massa van een stelsel. Aangezien de kernen van sterrenstelsels over het algemeen veel oude sterren bevatten zullen ze relatief veel bijdragen aan de totale massa van het stelsel, maar relatief weinig aan het totale licht. Dit zorgt ervoor dat de lichtdistributie die wij meten minder geconcentreerd is dan de massadistributie, en dus geen goed beeld geeft van de werkelijke structuur van een sterrenstelsel. Gemiddeld is de massadistributie van sterrenstelsels maar liefst 25% compacter dan de lichtdistributie.

Tenslotte worden de voorspellingen van theoretische modellen vergeleken met observaties, om licht te werpen op de processen die de groei van sterrenstelsels veroorzaken. Eenvoudige modellen blijken de relatieve groei van sterrenstelsels goed te reproduceren. In deze modellen ontstaan sterrenstelsels als platte ronddraaiende schijven, en kunnen ze door botsingen met andere stelsels of door interne instabiliteit omgevormd worden tot bolvormige stelsels. Zo blijkt dat de groei van sterrenstelsels volgt uit een paar eenvoudige principes en dat veel van de details van de modellen hier vrij weinig invloed op hebben.

INTRODUCTION

1.1 EXTRAGALACTIC ASTRONOMY

Since the formulation of the earliest cosmological models, observations of distant stars and galaxies have served a crucial role in constraining these models or bringing new, unknown issues to light. Galaxies are tracers of the overall matter distribution in the Universe, and as such can be used to obtain crucial information regarding the content of the Universe. Surrounded by reservoirs of gas and dark matter, and by orbiting satellite galaxies, they effectively serve as "signposts" which mark high-density regions of space. They are formed by - and sensitive to - a rich variety of physical processes, and thus serve as laboratories where these processes can be studied in detail.

In the early days of modern astronomy, as the structure of the Milky Way was being mapped out, thousands of faint, nebulous objects were discovered (e.g., Messier 1781; Herschel 1786). These mysterious clouds - now known to be distant galaxies - were not resolvable into individual stars, and it took a long time for the nature of these objects to become clear. Important clues regarding their properties were found in the 19th century, as new, larger telescopes became available (e.g., the 72-inch "Leviathan" built by the Earl of Rosse in 1845). A large fraction of nebulae were observed to have flat, disk-like morphologies, often with bright spiral arms, while many others were relatively featureless blobs. This morphological division marks the beginning of the study of galaxy structure.

Early classifications of galaxies based on their morphologies were greatly expanded once telescopes became powerful enough to resolve smaller structures. Furthermore, spectroscopic observations showed that galaxies not only looked different, but contained different stellar populations as well (e.g., Slipher 1918). Over the next years it became clear that many galaxy properties, such as total brightness, central concentration, or color, were connected in some way (e.g., Hubble 1926). In fact, the structure of galaxies holds key information regarding their assembly history and their interactions with other galaxies, and is closely tied to the properties of the underlying dark matter distribution. Galaxy structure therefore provides an extremely rich source of information with which to inform and challenge physical theory.

1.2 THE UNIVERSE AT $Z = 0$

Studies of the properties of individual galaxies and of the galaxy population as a whole can provide an effective tool to understand the contents and behaviour of the Universe. Correlations between different galaxy properties are used extensively in order to uncover the underlying physics. One of the most fundamental is the correlation between galaxy morphology and age, which results in a sequence of galaxy types that ranges from strongly starform-

ing spiral galaxies to passive elliptical galaxies. This correlation implies that the processes which transform galaxies from disks to spheroids (such as galaxy mergers) may also trigger quenching mechanisms that cause a shutdown in star formation. It provides a fundamental connection between the stellar populations within galaxies and their overall structure.

Structural scaling relations have been known to exist for many decades: the properties of bulge-dominated galaxies are related through the fundamental plane, which connects galaxy size, average surface brightness, and central velocity dispersion, and can be interpreted as an expression of dynamic equilibrium (e.g., Faber & Jackson 1976; Djorgovski & Davis 1987). Similarly, disk-dominated galaxies follow the Tully-Fisher relation (Tully & Fisher, 1977), which relates galaxy luminosity and rotation velocity. These and other relations can be used to gain valuable information about the interplay of different physical processes and their relative importance. However, until fairly recently progress was significantly impeded by a lack of large samples of galaxies with well-understood statistical properties.

An important change in this situation came a decade ago as a consequence of the Sloan Digital Sky Survey (SDSS; York et al. 2000). This survey provided imaging in five filters over more than 8000 square degrees of the sky, as well as spectra of more than two million galaxies. The spectra enabled accurate redshift measurements and the determination of stellar population parameters (e.g., Kauffmann et al. 2003; Brinchmann et al. 2004), while the multi-band imaging was useful for measurements of properties such as galaxy sizes, bulge fractions, and color gradients (e.g., Shen et al. 2003; Blanton et al. 2005). This rich source of data has allowed astronomers to study galaxy properties in a systematic and statistically sound way, unearthing correlations and pinpointing important physical processes (e.g., Kauffmann et al. 2003; Balogh et al. 2004; Baldry et al. 2004). The importance of SDSS for extragalactic studies is evident given the fact that SDSS-derived quantities are still used as benchmarks today.

However, the findings that have resulted from SDSS and other large-scale low-redshift surveys are based on observations that cover a very limited range in time. Measurements of the nearby universe provide an important baseline, and can be used to partially reconstruct a historical timeline. But our understanding of the history of the universe will remain incomplete without actual observations at high-redshift. In particular, the era around $z \sim 2$, when most of the stellar matter in the universe was formed (Madau et al., 1996), can provide a wealth of useful information.

1.3 MOVING TO HIGH REDSHIFT

In order to form an accurate picture of the evolution of the universe, it is essential to have observations which sample a range of cosmic epochs. Unfortunately, accurately determining galaxy properties at high redshift is difficult, as measurements become subject to a number of important observational and theoretical uncertainties. Three issues which are particularly problematic for structure measurements are outlined below.

Firstly, galaxies become very faint as their distance increases. In order to get high

signal-to-noise, exposure times need to be very long. As a result of this, spectroscopy of high-redshift galaxies is prohibitively time-consuming for all but the brightest galaxies. The most important consequence of this lack of spectroscopy is that it becomes very difficult to accurately determine the distances of galaxies. High-redshift surveys must depend instead on multi-band photometry in order to obtain approximate spectral energy distributions (SEDs). The resulting photometric redshifts are subject to much larger uncertainties than spectroscopic redshifts.

The lack of high-redshift spectra also prevents the determination of dynamic masses from observed velocity dispersions. Instead, stellar mass estimates are made, based on fits of stellar population models to the observed SED. This involves many assumptions regarding, e.g., the initial mass function, the distribution of dust in galaxies, and the star formation histories of galaxies. Typical systematic errors of photometrically derived stellar masses are estimated to be as large as a factor 6 (Conroy et al., 2009).

Thus, at high redshift two centrally important quantities - the distance to a galaxy and its total mass - can only be measured with large and difficult to quantify uncertainties. Comparison studies between stellar masses determined from SED fitting and dynamical masses from velocity dispersions indicate that, on average, SED-determined masses seem to agree fairly well with dynamical masses (e.g., Taylor et al. 2010; van de Sande et al. 2011; Martinez-Manso et al. 2011). However, these analyses are subject to other, equally problematic effects, such as uncertainties regarding the initial mass function of galaxies.

A second important problem for observations of high-redshift galaxies is the fact that their light is strongly redshifted. The emission from galaxies is a strong function of wavelength: young stars emit strongly at bluer wavelengths, while old stars (which represent the majority of mass in most galaxies) dominate the redder parts of the spectrum. This introduces problems when comparing the properties of galaxies at different redshifts, as care must be taken to always observe at the same rest-frame wavelength. Furthermore, for studies of galaxy structure it is particularly important to observe galaxies at very red wavelengths, in order to trace the mass distribution. Due to the relative inefficiency of infrared detectors (compared to optical CCDs) it is very difficult to do this effectively.

Finally, as one moves to higher redshift, galaxies of a given physical size subtend smaller angles on the sky. Atmospheric seeing becomes critically important as galaxy sizes become comparable to the size of the atmospheric point-spread function (PSF). Space-based telescopes such as HST partially alleviate this problem. However, even using these state-of-the-art facilities measurements at $z > 1$ are not straightforward. A physical distance of 1 kpc at these redshifts is comparable to the PSF full-width at half-maximum (FWHM) of the HST ACS camera, and detectors at redder wavelengths typically perform more poorly.

High-redshift observations come nowhere near $z = 0$ observations in terms of resolvable detail, and determinations of some of the most important galaxy properties suffer from large systematic uncertainties. This situation is inconvenient in many respects, but a positive side effect is that these limitations have forced high-redshift astronomers to reconsider common low-redshift approaches and to find novel ways to probe galaxy properties. One important corollary has been a stronger focus on robust observables and average prop-

erties of galaxy (sub)populations, which has led to a greater emphasis on the identification of connections between these populations.

1.4 CURRENT ISSUES

Despite observational difficulties, an enormous amount of information can be recovered from high-redshift observations by combining high-quality facilities with sophisticated analysis techniques. HST has played a major role in this respect, as it allowed astronomers to measure spatially resolved galaxy properties, and opened the door to detailed quantification of high-redshift galaxy structure.

Early studies of high-redshift galaxy structure which utilized the UV-optical ACS camera on HST revealed a universe that was significantly different from the present-day situation: galaxies were observed to be much bluer and more strongly starforming, and generally had very clumpy morphologies (e.g., Dickinson 2000; Papovich et al. 2005). These findings suggested that at $z \sim 2$ the Universe was in a turbulent phase of galaxy formation that stood in stark contrast to the ordered state of equilibrium of most galaxies today. Although at high redshift the average star formation is significantly higher, and more starforming galaxies exist, this effect was overestimated in early studies due to several causes. The first of these was selection bias; early galaxy catalogs were constructed based on selections in observed-frame optical light. At high redshift this is equivalent to a rest-frame UV selection, which will strongly bias the results towards starforming galaxies. Furthermore, since measurements of structure and morphology were often based on rest-frame ultraviolet photometry, the results mostly revealed the structure of starforming regions within galaxies, which are known to be extended and clumpy.

While it was not yet clear what the dominant morphology was of galaxies at $z \sim 2$, it had become clear that the universe already contained very old galaxies at this time. In fact, quiescent galaxies make up almost half the galaxy population at high stellar masses (e.g., Franx et al. 2003; Daddi et al. 2005; Kriek et al. 2006). Stellar population fits to the SEDs of these galaxies indicate that they contain very old (~ 1 Gyr) stellar populations. This finding came as a surprise, as it implied that the first galaxies must have formed on very short timescales and at extremely early redshifts. How early the first galaxies assembled remains an unanswered question, as old galaxies continue to be found at higher redshifts (e.g., Eyles et al. 2005; Mobasher et al. 2005; Wiklind et al. 2008; Richard et al. 2011).

Further research into these very old systems has revealed that they have properties which are very different from similarly old galaxies at $z=0$. The most apparent of these are their drastically smaller sizes and higher implied velocity dispersions: typical sizes are of the order of 1 kpc, a factor 4 smaller than similar-mass galaxies at low redshift (e.g., Daddi et al. 2005; van Dokkum et al. 2008). Only a very small number of possible counterparts to these objects have been found at low redshift (e.g., Taylor et al. 2010; Cassata et al. 2011; Poggianti et al. 2013), raising the question of how galaxies with no significant star formation could evolve so strongly between $z = 2$ and $z = 0$. Over the past years the subject of galaxy size

growth (as well as evolution in related quantities such as velocity dispersion, concentration, and surface density) has received a lot of attention; it is one of the main themes of this thesis.

Although much attention has been given to the structural evolution of passive galaxies, the population of starforming galaxies undergoes similarly rapid changes. Measurements of the cosmic star formation rate density indicate that the amount of star formation in the Universe increases from $z = 0$ to $z \sim 2$, after which it plateaus or rises slightly (e.g., Noeske et al. 2007; González et al. 2010; Bouwens et al. 2012; Stark et al. 2013). As a result of this both starforming and quiescent galaxies at high redshift have bluer colors than their low-redshift counterparts. Furthermore, star forming galaxies evolve in size (and surface density) at a rate similar to passive galaxies (Williams et al., 2010), and through a variety of processes can build up massive central bulges (e.g., Bell et al. 2012). All these changes in the average properties of the galaxy population are closely tied to one another and to the evolving properties of the universe (such as the average matter density or the cold gas fraction in halos). In order to use such measurements to constrain theoretical models of galaxy formation it is therefore of great importance to obtain accurate and robust results at all redshifts.

1.5 THIS THESIS

This thesis addresses several of these issues, focusing on how to measure galaxy mass distributions, what such measurements can reveal about the structure and morphology of high-redshift galaxies, and how their properties evolve with time. The results presented in this thesis are primarily based on data from HST, both at optical wavelengths (using ACS) and at near-infrared wavelengths (using WFC3). The installation of WFC3 in 2009 has been a strong driver of progress over the past few years, as it represents a significant jump in the efficiency of HST in the near-infrared. Both the sensitivity and resolution are comparable to ACS, resulting in consistently high-quality photometry over a wide wavelength range (300 - 1800 nm). Since the installation of WFC3 several significant legacy surveys have been carried out, most notably the HUDF09 (Bouwens et al. 2010; Oesch et al. 2010) and CANDELS (Grogin et al. 2011; Koekemoer et al. 2011). These two surveys provide extremely deep data over a small area (HUDF09) as well as shallower data over a larger portion of the sky (CANDELS). Combined with deep K-band selected galaxy catalogs, this data enables detailed analysis of large numbers of galaxies.

In **Chapter 2** we utilize the extreme depth of the HUDF09 to address important questions regarding galaxy size measurements at high redshift. We focus on one particular extremely compact massive quiescent galaxy. Using sophisticated techniques we measure this galaxy's radial surface brightness profile and investigate the likelihood of measurement biases being the cause of small measured galaxy sizes.

In **Chapter 3** we extend our structural measurements to the overall galaxy population, analyzing the structure of the most massive galaxies in the HUDF09. Galaxies at low redshift follow a relation between morphology and star formation activity (i.e., the Hubble sequence). Using a combination of optical and NIR data we assess whether this relation

between structure and stellar populations already existed at $z \sim 2$, and what this implies for galaxy formation mechanisms.

In **Chapter 4** we revisit the population of high-redshift quiescent galaxies. We take advantage of the large area of CANDELS to measure the structure of a larger sample of galaxies. The high-resolution capabilities of HST enable a very precise analysis of these galaxies' structure. We closely analyze the light distributions of these galaxies and the properties of similar galaxies at different redshifts, in order to address the validity of different evolutionary scenarios.

Measurements of galaxy structure are by necessity based on the light distribution within these galaxies. However, galaxies contain gradients of stellar populations, with corresponding gradients in stellar mass-to-light ratios. This suggests that properties derived from light distributions may not accurately reflect the properties of the underlying mass distribution. If this effect is redshift-dependent it could drastically affect conclusions regarding the mass assembly of galaxies. In **Chapter 5** we address this issue by measuring the stellar mass surface density profiles of a large sample of galaxies over a range of redshifts.

Finally, galaxy growth trends are placed in a theoretical context in **Chapter 6**, by comparing them to predictions from analytical models. These models contain simple prescriptions for the growth of stellar disks and bulges. By comparing several different models we attempt to robustly unearth the dominant underlying physical mechanisms.

REFERENCES

- Baldry, I. K., Glazebrook, K., Brinkmann, J., et al. 2004, *ApJ*, 600, 681
- Balogh, M. L., Baldry, I. K., Nichol, R., et al. 2004, *ApJ*, 615, L101
- Bell, E. F., van der Wel, A., Papovich, C., et al. 2012, *ApJ*, 753, 167
- Blanton, M. R., Schlegel, D. J., Strauss, M. A., et al. 2005, *AJ*, 129, 2562
- Brinchmann, J., Charlot, S., White, S. D. M., et al. 2004, *MNRAS*, 351, 1151
- Bouwens, R. J., et al. 2010, *ApJ*, 709, L133
- Bouwens, R. J., Illingworth, G. D., Oesch, P. A., et al. 2012, *ApJ*, 754, 83
- Cassata, P., Giavalisco, M., Guo, Y., et al. 2011, *ApJ*, 743, 96
- Conroy, C., Gunn, J. E., & White, M. 2009, *ApJ*, 699, 486
- Daddi, E., et al. 2005, *ApJ*, 626, 680
- Dickinson, M. 2000, *Philosophical Transactions of the Royal Society of London, Series A*, 358, 2001
- Djorgovski, S., & Davis, M. 1987, *ApJ*, 313, 59
- Eyles, L. P., Bunker, A. J., Stanway, E. R., Lacy, M., Ellis, R. S., & Doherty, M. 2005, *MNRAS*, 364, 443
- Faber, S. M., & Jackson, R. E. 1976, *ApJ*, 204, 668
- Franx, M., et al. 2003, *ApJ*, 587, L79
- González, V., Labbé, I., Bouwens, R. J., et al. 2010, *ApJ*, 713, 115
- Grogin, N. A., Kocevski, D. D., Faber, S. M., et al. 2011, *ApJ*, 197, 35
- Herschel, W. 1786, *Royal Society of London Philosophical Transactions Series I*, 76, 457
- Hubble, E. P. 1926, *ApJ*, 64, 321
- Kauffmann, G., Heckman, T. M., White, S. D. M., et al. 2003, *MNRAS*, 341, 33
- Kauffmann, G., Heckman, T. M., White, S. D. M., et al. 2003, *MNRAS*, 341, 54
- Koekemoer, A. M., Faber, S. M., Ferguson, H. C., et al. 2011, *ApJ*, 197, 36
- Kriek, M., et al. 2006, *ApJ*, 649, L71
- Madau, P., Ferguson, H. C., Dickinson, M. E., et al. 1996, *MNRAS*, 283, 1388
- Martinez-Manso, J., Guzman, R., Barro, G., et al. 2011, *ApJ*, 738, L22
- Messier, C. 1781, *Connaissance des Temps for 1784*, p. 227-267, 227
- Mobasher, B., et al. 2005, *ApJ*, 635, 832
- Noeske, K. G., Weiner, B. J., Faber, S. M., et al. 2007, *ApJ*, 660, L43
- Oesch, P. A., et al. 2010, *ApJ*, 709, L16
- Papovich, C., Dickinson, M., Giavalisco, M., Conselice, C. J., & Ferguson, H. C. 2005, *ApJ*, 631, 101
- Poggianti, B. M., Calvi, R., Bindoni, D., et al. 2013, *ApJ*, 762, 77
- Richard, J., Kneib, J.-P., Ebeling, H., Stark, D., Egami, E., & Fiedler, A. K. 2011, *MNRAS*, 414, L31
- Shen, S., Mo, H. J., White, S. D. M., et al. 2003, *MNRAS*, 343, 978
- Slipher, V. M. 1918, *Publications of the American Astronomical Society*, 3, 98
- Stark, D. P., Schenker, M. A., Ellis, R., et al. 2013, *ApJ*, 763, 129

- Taylor, E. N., Franx, M., Brinchmann, J., van der Wel, A., & van Dokkum, P. G. 2010, ApJ, 722, 1
- Taylor, E. N., Franx, M., Glazebrook, K., et al. 2010, ApJ, 720, 723
- Tully, R. B., & Fisher, J. R. 1977, A&A, 54, 661
- van de Sande, J., et al. 2011, ApJ, 736, L9
- van Dokkum, P. G., et al. 2008, ApJ, 677, L5
- Wiklind, T., Dickinson, M., Ferguson, H. C., Giavalisco, M., Mobasher, V., Grogin, N. A., & Panagia, N. 2008, ApJ, 676, 781
- Williams, R. J., Quadri, R. F., Franx, M., et al. 2010, ApJ, 713, 738
- York, D. G., Adelman, J., Anderson, J. E., Jr., et al. 2000, AJ, 120, 1579

**CONFIRMATION OF THE COMPACTNESS OF A
Z = 1.91 QUIESCENT GALAXY WITH HST/WFC3**

We present very deep WFC3 photometry of a massive, compact galaxy located in the HUDF. This quiescent galaxy has a spectroscopic redshift $z = 1.91$ and has been identified as an extremely compact galaxy by Daddi et al. (2005). We use new H_{F160W} imaging data obtained with HST/WFC3 to measure the deconvolved surface brightness profile to $H \approx 28$ mag arcsec $^{-2}$. We find that the surface brightness profile is well approximated by a $n = 3.7$ Sérsic profile. Our deconvolved profile is constructed by a new technique which corrects the best-fit Sérsic profile with the residual of the fit to the observed image. This allows for galaxy profiles which deviate from a Sérsic profile. We determine the effective radius of this galaxy: $r_e = 0.42 \pm 0.14$ kpc in the observed H_{F160W} -band. We show that this result is robust to deviations from the Sérsic model used in the fit. We test the sensitivity of our analysis to faint "wings" in the profile using simulated galaxy images consisting of a bright compact component and a faint extended component. We find that due to the combination of the WFC3 imaging depth and our method's sensitivity to extended faint emission we can accurately trace the intrinsic surface brightness profile, and that we can therefore confidently rule out the existence of a faint extended envelope around the observed galaxy down to our surface brightness limit. These results confirm that the galaxy lies a factor ~ 10 off from the local mass-size relation.

Daniel Szomoru, Marijn Franx, Pieter G. van Dokkum, Michele Trenti, Garth D. Illingworth,
Ivo Labbé, Rychard J. Bouwens, Pascal A. Oesch, C. Marcella Carollo
The Astrophysical Journal, 714, L244-L248, 2010

2.1 INTRODUCTION

A significant fraction of massive galaxies at $z \approx 2$ are early-type galaxies containing quiescent stellar populations (e.g., Franx et al. 2003; Daddi et al. 2005; Kriek et al. 2006). These galaxies must have formed very early in the universe's history and can therefore provide important constraints on galaxy formation and evolution models. Many of these quiescent galaxies have been found to be extremely compact, with effective radii a factor ~ 6 smaller than their low- z counterparts (e.g., Daddi et al. 2005; Trujillo et al. 2006; van Dokkum et al. 2008). This is quite puzzling, since these compact galaxies are passively evolving and are therefore not expected to change strongly in size or mass if they do not merge. We note that Mancini et al. (2010) find some large massive quiescent galaxies at $z \sim 1.5$, showing that not all massive quiescent galaxies at high redshift are compact.

Within the context of current models, galaxy mergers play an important role in galaxy evolution (e.g., White & Frenk 1991). These mergers may cause compact $z \sim 2$ galaxies to grow "inside-out", i.e., the mergers would increase the size of the galaxies (e.g., van Dokkum et al. 2010; Hopkins et al. 2009b). Whether the resulting size growth is large enough, however, is uncertain (e.g., Bezanson et al. 2009).

Several authors have emphasised that there are several systematic uncertainties that affect both radius and mass determinations. Firstly, effective radii may be underestimated due to complex morphologies. Specifically, an extended low surface brightness component could remain undetected due to low signal-to-noise (S/N), thereby lowering the observed size (e.g., Hopkins et al. 2009a; Mancini et al. 2010, but see van Dokkum et al. 2008; van der Wel et al. 2008). Secondly, mass-to-light gradients may result in a luminosity-weighted effective radius that is smaller than the mass-weighted effective radius (e.g., Hopkins et al. 2009a; Hopkins et al. 2009b). Such gradients arise in certain models for the formation of massive ellipticals (e.g., Robertson et al. 2006; Naab et al. 2007). Lastly, the inferred stellar masses may be affected by incorrect assumptions regarding the initial mass function (IMF) and stellar evolution models (e.g., Muzzin et al. 2009, and references therein).

In this Letter we use new very deep near-infrared (NIR) imaging data from the Hubble Space Telescope's Wide Field Camera 3 (HST/WFC3) to investigate the possibility of size underestimation due to lack of S/N. We examine the possibility of a "hidden" faint extended component being present in $z \approx 2$ compact quiescent galaxies, focusing on the most massive quiescent galaxy in the Hubble Ultra Deep Field (HUDF), which has previously been studied by Daddi et al. (2005). We adopt the following values for cosmological parameters: $H_0 = 70 \text{ km s}^{-1} \text{ Mpc}^{-1}$, $\Omega_m = 0.3$, and $\Omega_\Lambda = 0.7$. All stellar masses are derived assuming a Kroupa IMF (Kroupa, 2001). All effective radii are circularized, unless noted otherwise.

2.2 OBSERVATIONS AND SAMPLE

Our study utilises new WFC3/IR H_{F160W} -band imaging data taken within the HUDF. This data is part of the first of three ultra-deep pointings which will be completed over the next year as part of the HUDF09 HST Treasury program (GO11563). The current WFC3 imaging consists of 78600 seconds of exposure time in the H_{F160W} band, leading to a limiting magnitude of 28.8. The PSF FWHM is ~ 0.16 arcsec. Details of the data reduction can be found in Bouwens et al. (2010).

Since the WFC3 data does not cover the complete HUDF, most of the compact massive $z \approx 2$ galaxies from e.g. Daddi et al. (2005) and Cimatti et al. (2008) fall outside of the observed area. From the compact $z \approx 2$ galaxies inside the WFC3 HUDF image area we select the most massive one, located at $\alpha = 3:32:38.12$, $\delta = -27:47:49.63$. This galaxy has a spectroscopic redshift $z = 1.91$ (Daddi et al., 2005), stellar mass $M_* = 0.56 \times 10^{11} M_\odot$ (Wuyts et al. 2008; Förster Schreiber et al. 2009), and effective radius $r_e < 1$ kpc in the observed z band (Daddi et al. 2005; Cimatti et al. 2008). It was identified by Daddi et al. (2005) as passively evolving based on the BzK criterion. A summary of the galaxy's structural parameters is given in Table 2.1. An image of the galaxy is shown in Figure 2.1. It is sufficiently separated from its neighbors to prevent contamination of its surface brightness profile.

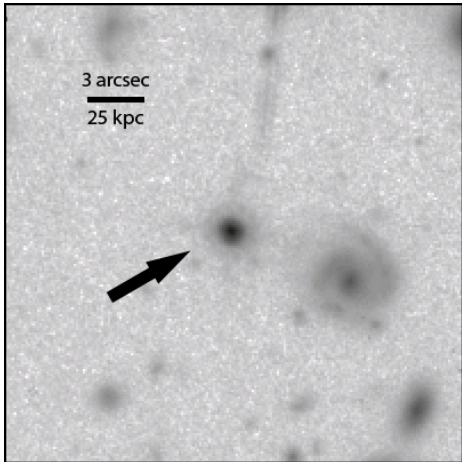


Figure 2.1: The WFC3 H_{F160W} -band image of the galaxy. It is well-separated from its nearest neighbors.

2.3 FITTING AND SIZE

We use the GALFIT package (Peng et al., 2002) to fit two-dimensional Sérsic (1968) model profiles convolved with the PSF to the observed surface brightness distribution. This is an essential step in deriving the structure of the galaxy, as the FWHM of the PSF of the WFC3 images is significant compared to the size of the galaxy. We use a PSF extracted from a nearby unsaturated star and base our masking image on a SExtractor (Bertin & Arnouts 1996) segmentation map. We fit nine different models with fixed Sérsic index ($n = 1, 2, \dots, 9$), as well as a model where n is a free parameter.

The effective radii from the Sérsic fits range between 0.42 and 0.48 for Sérsic indices varying between $n = 1$ and $n = 9$, with the free- n fit producing a value of 0.43 kpc (at $n = 3.7$). The best-fit Sérsic profiles are shown in Figure 2.2. Despite the fact that the effective radii are rather similar, it is clear that the derived profiles vary significantly with n .

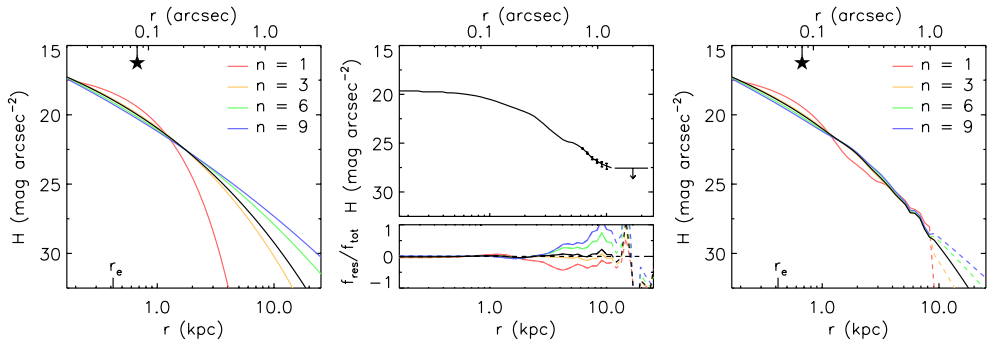


Figure 2.2: Our method of correcting the observed surface brightness profile for the effects of the HST WFC3 PSF and incorrect profile modeling. In the left panel the best-fitting Sérsic models, derived from a 2D fit using a star as the PSF, are shown for different values of n . The black curve indicates the free- n fit, with $n = 3.7$. The profiles show large variations. In the top center panel the observed profile is shown. The residual fluxes from the Sérsic fits are shown in the bottom panel as a fraction of the observed flux. In the right panel the profiles derived using our "residual-correction" method are shown. At large radii, where uncertainties in the sky determination become significant, the profile is extrapolated. This is indicated by dashed curves. The residual-corrected profiles are much more robust to modeling errors than the uncorrected profiles. The derived effective radius is indicated on the bottom x-axis, the PSF size (FWHM) is indicated by the star symbol on the top x-axis. The solid horizontal line in the middle panel indicates the 3σ sky noise level. As can be seen, the surface brightness profile can be robustly measured to a surface brightness of $28 \text{ mag arcsec}^{-2}$.

There is no intrinsic reason why galaxies should have "perfect" Sérsic profiles. Although locally the surface brightness profiles of elliptical galaxies are well fitted by single Sérsic profiles over a large range of radii (e.g., Kormendy et al. 2009), at high redshift very few radial profiles have been measured directly; in most cases PSF-convolved model fits have been performed to the imaging. Moreover, if elliptical galaxies grow by an inside-out process (e.g., Hopkins et al. 2009a; Feldmann et al. 2009), the surface brightness profiles of their progenitors may deviate from Sérsic profiles. We therefore developed a method to derive more robust intensity profiles, which depend less on the Sérsic n parameter used for the fit.

Our approach is the following: for each Sérsic fit, we calculate the residual image, which is an image of the observed flux minus the PSF-convolved model. We derive a profile of the residual flux measured along circles centered on the galaxy. We add this residual profile to the deconvolved model Sérsic profile. We note that the intrinsic profile is deconvolved for PSF, but the residuals are not. This procedure is similar to how the CLEAN deconvolution method employed in radioastronomy handles residuals (Högbom, 1974). We thus remove or add flux at those radii where the model does not adequately describe the data, making a first order correction for errors caused by the incorrect profile choice. For large radii, where (systematic) uncertainties in the sky determination become significant, we extrapolate the residual-corrected profile by using the uncorrected Sérsic profile, scaled to the residual-corrected profile at the transition radius. These "residual-corrected" profiles are then integrated in order to determine the true half-light radius, which we refer to as

Table 2.1: Structural parameters

Source	n	r_e (kpc)	b/a	M_* ($10^{11} M_\odot$)	H_{F160W}^{tot} (AB)
This Letter	3.7 ± 0.38	0.42 ± 0.14	0.70	...	22.15 ± 0.067
Previous work	4.7 ± 0.6^1	0.79 ± 0.08^1	0.74^1	0.56^2	22.12 ± 0.03^2

¹Daddi et al. (2005), measured in z_{F850LP} band

²Wuyts et al. (2008)

$r_{e,deconv}$. The residual-corrected profiles are shown in Figure 2.2. The structural parameters of the best-fitting profile are given in Table 2.1.

It is clear from Figure 2.2 that the residual-corrected profiles are much less sensitive to the Sérsic- n value adopted for the initial modeling, especially at radii beyond a few kpc. Furthermore, deviations from the Sérsic profile are taken into account; as we show in Section 4, using the residual-corrected profile we can trace the true surface brightness profile much more accurately than using simple analytical Sérsic fits. This is due to the fact that the S/N of the faint emission at large radii is so low that the fitting procedure ignores it, even though a lot of flux can originate there. Thus the stability of the parameters derived from Sérsic fits is no guarantee for correctness. This is particularly relevant when the galaxies have complex morphologies, such as in the case of a bright, compact galaxy surrounded by a faint, extended envelope.

Uncertainties in $r_{e,deconv}$ and the total H -band magnitude are estimated from the range in values obtained from the fixed- n residual-corrected profiles. The errors given in Table 2.1 are the rms errors of the best-fit parameters from all of the fits, and give an indication of the systematic errors due to differences between the observed surface brightness profile and the Sérsic models used in the fitting procedure. The uncertainty in n is estimated using simulations: we add random sky noise to the observed galaxy image. This is repeated several times, resulting in a number of images, on each of which we perform the fitting procedure described above. The uncertainty given in Table 2.1 is two times the rms error of the best-fit parameter from all of the fits.

Our results are the following: the galaxy is best fit by a Sérsic profile with $n = 3.7$. Using the residual-corrected profile we find that the effective radius of the galaxy is $r_{e,deconv} = 0.050$ arcsec, which corresponds to $r_{e,deconv} = 0.42$ kpc. If we fix the Sérsic index to a constant value, the inferred size does not vary substantially: $r_{e,deconv}$ varies from 0.31 kpc for $n = 9$ to 0.51 kpc for $n = 1$. Thus, the deviations from the best-fitting profile are $< 20\%$. Our size estimate is therefore reasonably robust to deviations from the model profile.

We have investigated the influence of PSF uncertainties; if we use PSFs extracted from other stars in the field we find variations in $r_{e,deconv}$ of $< 10\%$. We have used the Tiny Tim software package¹ to investigate the spatial dependence of the PSF independently. We

¹<http://www.stsci.edu/software/tinytim>

find that the derived effective radius changes very little with the position of the reference star used, with a maximum of 10% in opposite corners of the field. The difference in effective radius due to the distance between the reference star and the galaxy is less than 1%. We therefore conclude that PSF errors do not present a significant problem in our analysis.

2.4 LOW SURFACE BRIGHTNESS SENSITIVITY

We now determine whether faint extended emission would be detected using our data. To this end we construct several simulated galaxy images which consist of two components; a compact component, described by a $n = 4$ Sérsic profile with an effective radius roughly equal to the observed galaxy (see Table 2.1), and an extended component, described by a Sérsic profile with either $n = 4$, $r_e \approx 3.5$ kpc or $n = 1$, $r_e \approx 15$ kpc. The extended component has a flux that is either 10% or 50% of the compact component's flux. The compact component's flux is chosen such that the total flux of the two components is equal to the observed galaxy's total flux. The images are convolved with the PSF, and sky and readout noise are added. The images are then fit with a single Sérsic profile using GALFIT, and a residual-corrected profile is constructed. By comparing the half-light radii obtained in this way to the intrinsic half-light radii we can quantify the sensitivity of our data to low surface brightness components.

The results of our simulated galaxy fits are shown in Figure 2.3. The residual-corrected profiles closely follow the intrinsic profiles. The effective radii derived from the residual-corrected profiles are very close to the intrinsic effective radii: in three of the cases the difference is less than 5%. For the $n = 1$ extended component with a total flux equal to half of the compact component's flux the inferred radius is 10% smaller than the intrinsic radius, comparable to the systematic error due to modeling uncertainties (see Section 2.3). We also tested $n = 4$ and $n = 1$ models with effective radii of several kpc for the $n = 1$ extended component: these models are so well approximated by Sérsic models with higher values of n (> 4) that normal Sérsic profile fitting immediately retrieves the correct effective radii.

In conclusion, our method used on these deep data is sensitive to a faint extended component down to a surface brightness of $H \approx 28$ mag arcsec⁻², and using our method we retrieve effective radii that are within 1σ of the true value. We note that the effective radii obtained using the conventional method are, in most cases, very close to the intrinsic effective radii. However, the surface brightness profiles obtained in this way clearly deviate from the intrinsic profiles.

2.5 DISCUSSION

We have found that the galaxy under consideration is indeed remarkably small. We have fitted a Sérsic model to the observed flux distribution, and corrected the profile for the observed deviations. We have measured the galaxy's half light radius: $r_{e,deconv} = 0.42 \pm 0.14$ kpc. This result is robust to changes in the imposed Sérsic profile. As a check of our data's

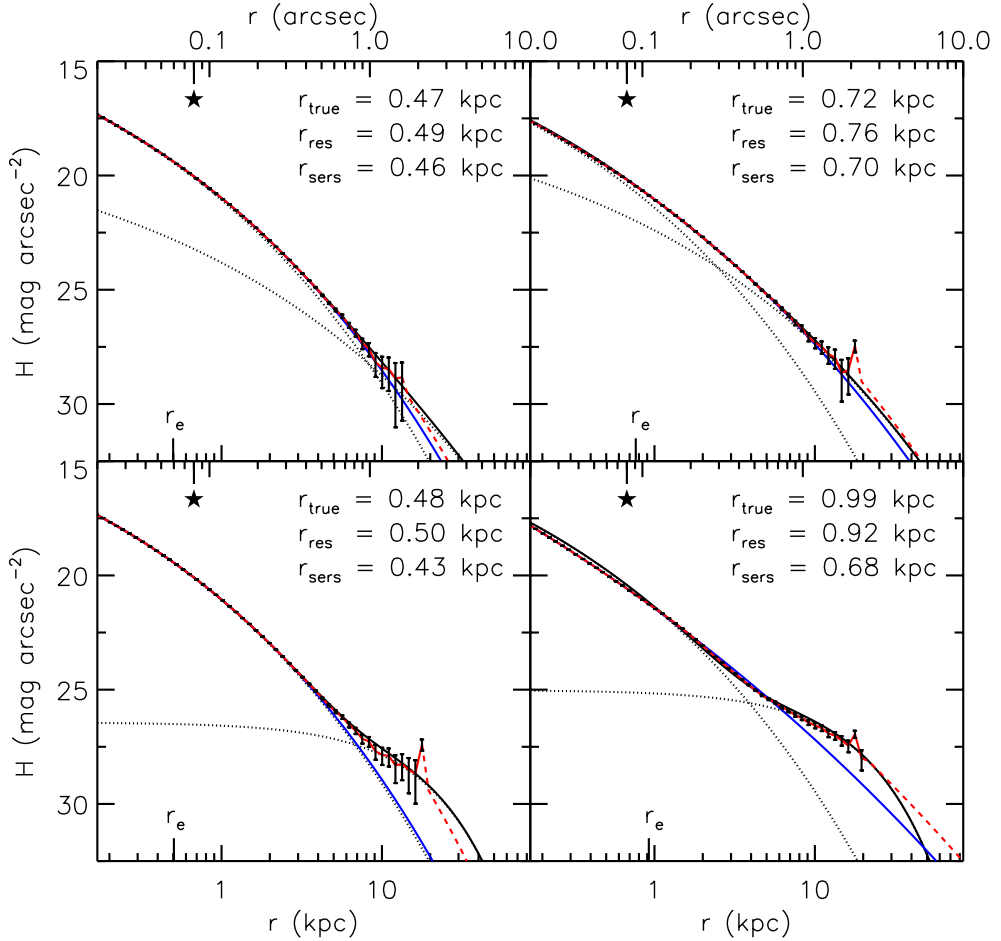


Figure 2.3: Residual-corrected fits to simulated galaxy images (red curves). *Top*: compact $n = 4$ profile and extended $n = 4$ profile, with flux ratios 10 : 1 (*left*) and 2 : 1 (*right*). *Bottom*: compact $n = 4$ profile and extended $n = 1$ profile, with the same flux ratios as in the top panels. At large radii, where uncertainties in the sky determination become significant, the profile is extrapolated. This is indicated by dashed curves. The solid black curves indicate the total intrinsic surface brightness profiles, the dotted black curves indicate the individual components that make up these profiles. The best-fit uncorrected Sérsic profiles are shown as blue curves. These deviate strongly from the true profiles at large radii. The residual-corrected profiles (red curves) follow the intrinsic profiles extremely well, demonstrating that our method recovers the intrinsic profiles accurately; the derived effective radii, indicated on the bottom x-axes, are within 10% of the true effective radii. The PSF size (HWHM) is indicated by the star symbols on the top x-axes.

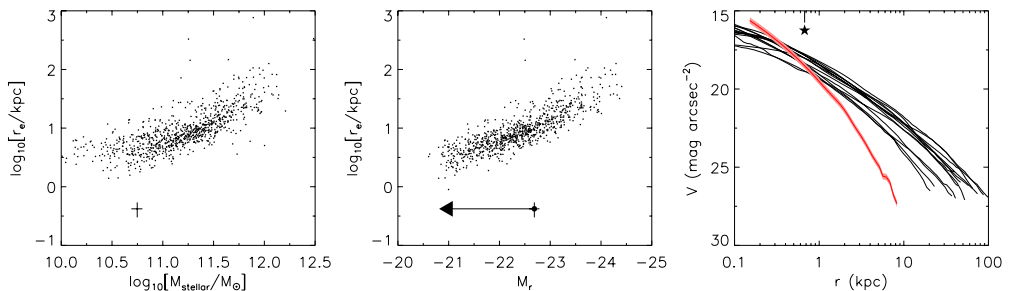


Figure 2.4: Relations between size and stellar mass (*left*) and size and rest-frame r -band luminosity (*middle*) for a sample of low-redshift galaxies, taken from Guo et al. (2009). The large symbol with error bars indicates the position of our galaxy. Low-redshift galaxies are much larger at similar stellar masses and luminosities. The arrow in the middle plot indicates the change in luminosity due to passive evolution to $z = 0$. The size of the galaxy is smaller than the local equivalents by a factor of 10. *Right*: comparison of best-fit residual-corrected rest-frame V-band surface brightness profile to elliptical galaxies in the Virgo cluster, from Kormendy et al. (2009). Virgo galaxies are plotted in different colors, corresponding to the following mass bins: black: $M_*/M_{\odot} > 10^{11}$; blue: $10^{10} < M_*/M_{\odot} < 10^{11}$. The observed high- z surface brightness profile has been corrected for cosmological surface dimming and passive M/L evolution from $z = 1.91$ to $z = 0$ (see text). Assuming the galaxy has a mass $> 10^{11} M_{\odot}$ at $z = 0$ its profile at large radii will evolve very strongly over the next 10 Gyr. The central surface brightness profile, on the other hand, shows much less evolution between $z \approx 2$ and $z = 0$.

sensitivity to a low surface brightness component we have constructed simulated galaxy images which include a faint extended component. We can reproduce the effective radii to 10% using our technique.

A possible cause for concern is that the galaxy might deviate strongly from a Sérsic profile. We have incorporated the residuals in our fit to compensate for such errors, and we note that the residuals from our best Sérsic model fit are quite low ($< 10\%$). This implies that our model profile is close to the real profile. This, and the fact that varying n has little influence on the derived half-light radius, suggests that our results are not strongly affected by this source of error.

Thus, our findings indicate that the small effective radius that has been found is not due to oversimplified modeling or a lack of S/N, and gives additional evidence that a strong evolution in size occurs from $z \approx 2$ to $z = 0$. It should be noted that our derived effective radius is 1.6 times smaller than the radii derived by Daddi et al. (2005) in the i and z bands. When we repeat our analysis on the ACS z -band data we obtain a slightly different value, $r_{e,deconv} \approx 0.65$ kpc (uncircularized), closer to the deep H -band imaging, and somewhat smaller than the value derived by Daddi et al. (2005) (but consistent within the errors). Hence all bands indicate a very small size.

Figure 2.4 illustrates the difference in size and mass between our galaxy and the $z = 0$ elliptical population; plotted in the first two panels are the compact galaxy we have studied and a sample of low-redshift central galaxies from groups and clusters in the Sloan Digital Sky Survey, analyzed by Guo et al. (2009). The compact $z \approx 2$ galaxy lies far off from

the $z = 0$ mass-size relation. The middle panel shows the galaxy on the mass-luminosity relation. We estimated the luminosity evolution of the compact galaxy from $z = 1.91$ to $z = 0$ in two ways: we first used the rest-frame $B - I$ color difference between low and high redshift to estimate the difference in mass-to-light ratio. Second we used the Fundamental Plane to estimate the evolution from $z = 0$ to $z = 1$ from van der Wel et al. (2005), and used the average evolution of the mass-to-light ratios of early-types in the CDFS at $z = 1$ and the $z = 1.91$ galaxy, both from Förster Schreiber et al. (in preparation). The resulting evolution is 1.8-2.2 magnitudes. As a result, the galaxy still lies off from the size-magnitude relation after correcting for evolution.

In the third panel of Figure 2.4 we compare the surface brightness profile of this galaxy to those of elliptical galaxies in the Virgo cluster. The profile shown has been corrected for cosmological surface brightness dimming and passive luminosity evolution from $z = 1.91$ to $z = 0$. The total correction is $-3.5 + 2 \approx -1.5$ magnitudes. Even though the galaxy has an average density > 100 times larger than the average $z = 0$ elliptical of the same mass, its surface brightness profile in the central kpc is actually rather similar to those of the most massive galaxies at $z = 0$ - the average density measured at fixed physical radius is not that different. This is consistent with results obtained by other authors (e.g., Bezanson et al. 2009; Hopkins et al. 2009a; Feldmann et al. 2009; van Dokkum et al. 2010). Thus, the main difference between $z = 0$ and this $z \approx 2$ galaxy is at larger radii where the $z \approx 2$ galaxy has much lower surface brightness. Such a result could be explained by inside-out growth.

We note also that there may be significant errors in the mass determination of $z \approx 2$ compact galaxies, due to e.g. incorrect assumptions about the IMF. Changes in the low mass end of the IMF affect both the masses of the high redshift and low redshift galaxies, and are nearly irrelevant. However, changes in the slope of the IMF will affect the derived passive evolution between $z = 2$ and $z = 0$, and will increase or decrease the size evolution. Changes in the IMF could thus have important consequences for evolution. Future deep NIR spectroscopic data should provide direct information on the kinematics of these objects and will allow us to confirm their high masses (see e.g., van Dokkum et al. 2009).

Finally, it will be interesting to obtain similar deep data on other compact massive galaxies, so that their profiles can be analyzed to the same surface brightness limit. We note that stacking can also lead to a great increase in imaging depth; e.g., Cassata et al. (2009), van Dokkum et al. (2008), and van der Wel et al. (2008) stack samples of compact galaxies and obtain very good constraints on their average surface brightness profile. However, with the new WFC3 data available in the coming years many more compact massive galaxies can be studied on an individual basis.

REFERENCES

- Beckwith, S. V. W., Stiavelli, M., Koekemoer, A. M., Caldwell, J. A. R., Ferguson, H. C., Hook, R., Lucas, R. A., Bergeron, L. E., Corbin, M., Jodge, S., Panagia, N., Robertson, M., Royle, P., Somerville, R. S., Sosey, M. 2006, *AJ*, 132, 1729
- Bertin, E., Arnouts, S. 1996, *A&AS*, 117, 393
- Bezanson, R., van Dokkum, P. G., Tal, T., Marchesini, D., Kriek, M., Franx, M., Coppi, P. 2009, *ApJ*, 697, 1290
- Bouwens, R. J., Illingworth, G. D., Oesch, P. A., Stiavelli, M., van Dokkum, P. G., Trenti, M., Magee, D., Labbé, I., Franx, M., Carollo, C. M. 2010, *ApJ*, 709, L133
- Cassata, P., Giavalisco, M., Guo, Y., Ferguson, H., Koekemoer, A., Renzini, A., Fontana, A., Salimbeni, S., Dickinson, M., Casertano, S., Conselice, C. J., Grogin, N., Lotz, J. M., Papovich, C., Lucas, R. A., Straughn, A., Gardner, J. P., Moustakas, L. 2009, arXiv:0911.1158
- Cimatti, A., Cassata, P., Pozzetti, L., Kurk, J., Mignoli, M., Renzini, A., Daddi, E., Bolzonella, M., Brusa, M., Rodighiero, G., Dickinson, M., Franceschini, A., Zamorani, G., Berta, S., Rosati, P., Halliday, C. 2008, *A&A*, 482, 21
- Daddi, E., Renzini, A., Pirzkal, N., Cimatti, A., Malhotra, S., Stiavelli, M., Xu, C., Pasquali, A., Rhoads, J. E., Brusa, M., di Serego Alighieri, S., Ferguson, H. C., Koekemoer, A. M., Moustakas, L. A., Panagia, N., Windhorst, R. A. 2005, *ApJ*, 626, 680
- van Dokkum, P. G. 2005, *ApJ*, 130, 2647
- van Dokkum, P. G., Franx, M., Kriek, M., Holden, B., Illingworth, G. D., Magee, D., Bouwens, R., Marchesini, D., Quadri, R., Rudnick, G., Taylor, E. N., Toft, S. 2008, *ApJ*, 677, L5
- van Dokkum, P. G., Whitaker, K. R., Brammer, G., Franx, M., Kriek, M., Labbé, I., Marchesini, D., Quadri, R., Bezanson, R., Illingworth, G. D., Muzzin, A., Rudnick, G., Tal, T., Wake, D. 2010, *ApJ*, 709, 1018
- van Dokkum, P. G., Kriek, M., Franx, M. 2009, *Nature*, 460, 717
- Eggen, O. J., Lynden-Bell, D., Sandage, A. R. 1962, *ApJ*, 136, 748
- Feldmann, R., Carollo, C. M., Mayer, L., Renzini, A., Lake, G., Quinn, T., Stinson, G. S., Yepes, G. 2009, *ApJ*, 709, 218
- Franx, M., Labbé, I., Rudnick, G., van Dokkum P. G., Daddi, E., Förster Schreiber, N. M., Moorwood, A., Rix, H.-W., Röttgering, H., van de Wel, A., van der Werf, P., van Starkenburg, L. 2003, *ApJ*, 587, L79
- Guo, Y., McIntosh, D. H., Mo, H. J., Katz, N., van den Bosch, F. C., Weinberg, M., Weinmann, S. M., Pasquali, A., Yang, X. 2009, *MNRAS*, 398, 1129
- Högbom, J. A. 1974, *A&AS*, 15, 417
- Hopkins, P. F., Bundy, K., Murray, N., Quataert, E., Lauer, T. R., Ma, C.-P. 2009a, *MNRAS*, 398, 898
- Hopkins, P. F., Bundy, K., Hernquist, L., Wuyts, S., Cox, T. J. 2009b, *MNRAS*, 401, 1099
- Kormendy, J., Fisher, D. B., Cornell, M. E., Bender, R. 2009, *ApJS*, 182, 216

- Kriek, M., van Dokkum, P. G., Franx, M., Quadri, R., Gawiser, E., Herrera, D., Illingworth, G. D., Labbé, I., Lira, P., Marchesini, D., Rix, H.-W., Rudnick, G., Taylor, E. N., Toft, S., Urry, M. C., Wuyts, S. 2006, *ApJ*, 649, 71
- Kroupa, P. 2001, *MNRAS*, 322, 231
- Mancini, C., Daddi, E., Renzini, A., Salmi, F., McCracken, H. J., Cimatti, A., Onodera, M., Salvato, M., Koekemoer, A. M., Aussel, H., Le Floch, E., Willott, C., Capak, P. 2010, *MNRAS*, 401, 933
- Muzzin, A., van Dokkum, P. G., Franx, M., Marchesini, D., Kriek, M., Labbé, I. 2009, *ApJ*, 706, L188
- Naab, T., Johansson, P. H., Ostriker, J. P., Efstathiou, G. 2007, *ApJ*, 658, 710
- Peng, C. Y., Ho, L. C., Impey, C. D., Rix, H.-W. 2000, *AJ*, 124, 266
- Robertson, B., Bullock, J. S., Cox, T. J., Di Matteo, T., Hernquist, L., Springel, V., Yoshida, N. 2006, *ApJ*, 645, 986
- Sérsic, J. L. 1968, *Atlas de Galaxias Australes* (Cordoba: Obs. Astron.)
- Trujillo, I., Feulner, G., Goranova, Y., Hopp, U., Longhetti, M., Saracco, P., Bender, R., Braitto, V., Della Ceca, R., Drory, N., Mannucci, F., Severgnini, P. 2006, *MNRAS*, 373, L36
- van der Wel, A., Franx, M., van Dokkum, P. G., Rix, H.-W., Illingworth, G. D., Rosati, P. 2005, *ApJ*, 631, 145
- van der Wel, A., Holden, B. P., Zirm, A. W., Franx, M., Rettura, A., Illingworth, G. D., Ford, H. C. 2008, *ApJ*, 688, 48
- White, S. D. M., Frenk, C. S. 1991, *ApJ*, 379, 52
- Wuyts, S., Labbé, I., Förster Schreiber, N. M., Franx, M., Rudnick, G., Brammer, G. B., van Dokkum, P. G. 2008, *ApJ*, 682, 985

MORPHOLOGICAL EVOLUTION OF GALAXIES FROM ULTRADEEP HST WFC3 IMAGING: THE HUBBLE SEQUENCE AT $z \sim 2$.

We use ultra-deep HST WFC3/IR imaging of the HUDF to investigate the rest-frame optical morphologies of a mass-selected sample of galaxies at $z \sim 2$. We find a large variety of galaxy morphologies, ranging from large, blue, disk-like galaxies to compact, red, early-type galaxies. We derive rest-frame $u-g$ color profiles for these galaxies and show that most $z \sim 2$ galaxies in our sample have negative color gradients such that their cores are red. Although these color gradients may partly be caused by radial variations in dust content, they point to the existence of older stellar populations in the centers of $z \sim 2$ galaxies. This result is consistent with an "inside-out" scenario of galaxy growth. We find that the median color gradient is fairly constant with redshift: $(\Delta(u - g_{\text{rest}})/\Delta(\log r))_{\text{median}} = -0.47, -0.33$ and -0.46 for $z \sim 2, z \sim 1$ and $z = 0$, respectively. Using structural parameters derived from surface brightness profiles we confirm that at $z \sim 2$ galaxy morphology correlates well with specific star formation rate. At the same mass, star forming galaxies have larger effective radii, bluer rest-frame $u-g$ colors and lower Sérsic indices than quiescent galaxies. These correlations are very similar to those at lower redshift, suggesting that the relations that give rise to the Hubble sequence at $z = 0$ are already in place for massive galaxies at this early epoch.

Daniel Szomoru, Marijn Franx, Rychard J. Bouwens, Pieter G. van Dokkum, Ivo Labbé,
Garth D. Illingworth, Michele Trenti
The Astrophysical Journal, 735, L22-L27, 2011

3.1 INTRODUCTION

Since the description of the Hubble sequence (e.g., Hubble 1926; de Vaucouleurs 1959; Sandage & Tammann 1981) we have learned that position along the Hubble sequence correlates with parameters like color, stellar age, and gas fraction (e.g., Roberts & Haynes 1994). However, morphologies by themselves provide very limited information, as they are scale free and do not include physical parameters such as surface brightnesses, sizes, luminosities and masses. Using the Sloan Digital Sky Survey (SDSS, York et al. 2000), Kauffmann et al. (2003) showed that the main parameter driving galaxy properties is stellar mass. High-mass galaxies are generally red, have old stellar populations and low specific star formation rates (SSFRs), while low-mass galaxies are generally blue, have young stellar populations and high SSFRs.

A key question is what the structure was of the progenitors of low-redshift galaxies. Hubble Space Telescope studies out to redshift $z \sim 1$ indicate that the morphological variation is comparable to that at low redshift (e.g., Bell et al. 2004). More recent studies of $z > 2$ galaxies using the HST NICMOS camera have yielded varying results, largely due to different selection criteria. For example, Papovich et al. (2005) studied the rest-frame optical morphologies of a flux-limited sample of galaxies at $z \approx 2.3$ and found that they are generally irregular. Toft et al. (2005), on the other hand, investigated the rest-frame optical and UV morphologies of distant red galaxies (DRGs) in the Hubble Ultra Deep Field (HUDF), and found both galaxies with irregular morphologies and galaxies with smooth morphologies. Additionally, they showed that the rest-frame optical morphologies of these galaxies are much more regular and centrally concentrated than the rest-frame UV morphologies.

With the advent of the Wide Field Camera 3 (WFC3), with its vastly improved sensitivity and resolution compared to NICMOS, it has become possible to analyze the rest-frame optical structure of high-redshift galaxies with an unprecedented level of detail. Cameron et al. (2010) have used data from the first year of observations of the HUDF and the Early Release Science Field to classify the rest-frame UV and optical morphologies of galaxies up to $z \sim 3.5$. These authors confirm results by e.g. Kriek et al. (2009), who showed that massive galaxies at $z \approx 2.3$ can be separated into two distinct classes: blue star-forming galaxies with irregular morphologies on the one hand, and red quiescent galaxies with smoother morphologies on the other.

In this Letter, we extend the previous results using the full two-year ultradeep near-infrared imaging of the HUDF taken with the HST WFC3. These data are the deepest ever obtained in the near-infrared and make it possible to analyze the morphologies, colors and structure of galaxies to $z \sim 3$ in the rest-frame optical. Using the incredible sensitivity and angular resolution of the WFC3 images we analyze the rest-frame optical surface brightness profiles of a mass-selected sample of galaxies at $z \sim 2$. We use these profiles to derive structural parameters such as size and profile shape, and obtain rest-frame color profiles. We study the correlations between these parameters as a function of redshift in order to investigate the Hubble sequence at different epochs in the history of the Universe. Throughout the Letter, we assume a Λ CDM cosmology with $\Omega_m = 0.3$, $\Omega_\Lambda = 0.7$ and $H_0 = 70 \text{ km s}^{-1} \text{ Mpc}^{-1}$.

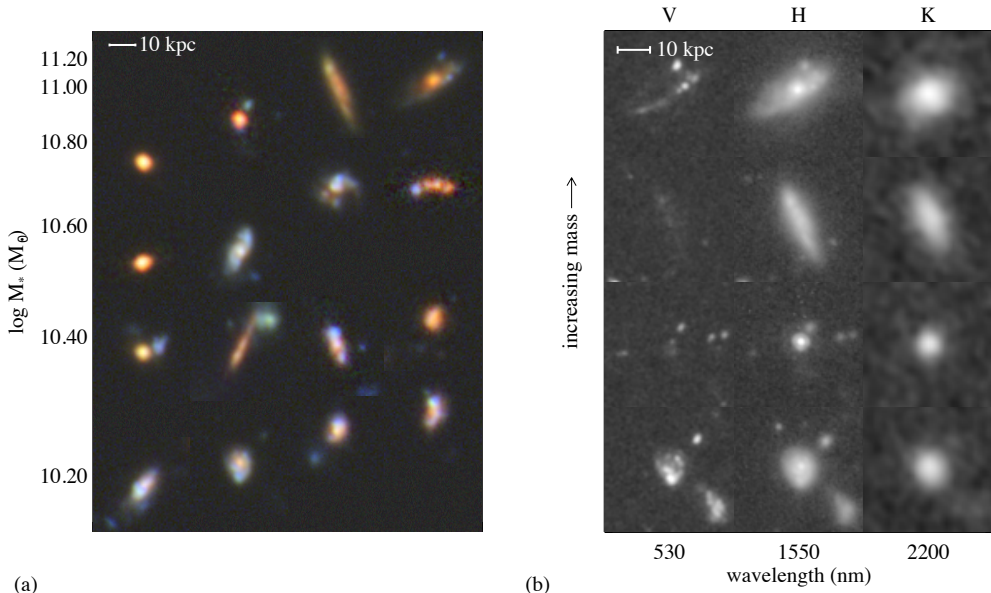


Figure 3.1: (a) Morphologies of $z \sim 2$ galaxies in the HUDF. The blue, green and red color channels are composed of PSF-matched HST/ACS i_{775} , HST/WFC3 Y_{105} and HST/WFC3 H_{160} images, respectively. Mass increases upwards. The galaxies exhibit a very large range in morphologies: from very compact, nearly unresolved spheroids with red colors, to large, extended disk-like galaxies with blue colors. Most of the galaxies have a well-defined center, which is usually redder than the outer parts of the galaxy. (b) Four massive galaxies at $z \sim 2$. From left to right, the galaxies are shown as observed in the HST/ACS V_{606} band, the HST/WFC3 H_{160} band, and the (ground-based) K_s band. The difference between the (PSF matched) V_{606} band and H_{160} band images is large: whereas the galaxies exhibit very regular morphologies and have well-defined centers in the H_{160} band, they are very clumpy and irregular in the V_{606} band, and in some cases are nearly undetected. These complex, wavelength-dependent morphologies suggest that $z \sim 2$ galaxies may be composed of multiple components with very different stellar ages.

3.2 MORPHOLOGIES AT $Z \sim 2$

We use the full two-year data taken with WFC3/IR of the HUDF, obtained in 2009-2010 as part of the HUDF09 HST Treasury program (GO11563). It consists of 24 orbits of Y_{105} imaging, 34 orbits of J_{125} imaging, and 53 orbits of H_{160} imaging. These images were reduced using an adapted pipeline (Bouwens et al. 2010, Oesch et al. 2010). The FWHM of the PSF is ≈ 0.16 arcsec. The images are combined with very deep ACS images of the HUDF (Beckwith et al., 2006) to construct color images of the massive galaxies in the field.

We use the K_s -selected catalog of Wuyts et al. (2008) to select galaxies in the HUDF for which WFC3 imaging is available. This catalog combines observations of the Chandra Deep Field South ranging from ground-based U band data to Spitzer $24\mu\text{m}$ data, and includes spectroscopic redshifts where available, as well as photometric redshifts derived using EAZY (Brammer et al., 2008). Stellar masses were estimated from spectral energy distribu-

Table 3.1: Galaxy properties.

Source	ID ^a	mag _{app} ^b (AB)	r_e^b (kpc)	n^b	$M_{stellar}^c$ (M_\odot)	$u - g_{rest}$	$\log \Sigma_{ave}$ ($M_\odot \text{ kpc}^{-2}$)	z^c
HUDF09	3203	21.81	3.49	1.15	10.65	0.49	8.77	1.998
HUDF09	3239	23.11	0.32	2.06	10.51	1.18	10.72	1.980
HUDF09	3242	22.10	0.44	3.21	10.76	1.18	10.67	1.910
HUDF09	3254	23.31	1.96	1.31	10.25	0.85	8.87	1.887*
HUDF09	3391	23.28	2.13	0.44	10.37	-0.04	8.92	1.919*
HUDF09	3421	23.79	2.12	0.90	10.59	0.19	9.14	2.457*
HUDF09	3463	22.47	1.80	1.20	10.09	0.59	8.78	1.659*
HUDF09	3486	22.43	2.78	0.65	10.22	0.88	8.53	1.628*
HUDF09	3595	22.39	3.67	0.41	10.98	0.87	9.06	1.853*
HUDF09	3653	23.85	1.94	0.95	10.27	1.24	8.90	1.776*
HUDF09	3721	22.02	3.00	1.16	10.54	0.63	8.79	1.843
HUDF09	3757	23.10	1.25	5.04	10.28	1.20	9.29	1.674*
HUDF09	3799	24.59	2.93	1.50	10.62	0.87	8.89	2.492*
HUDF09	6161	21.58	6.70	3.51	11.08	1.22	8.63	1.552
HUDF09	6225	23.26	2.58	0.56	10.33	0.72	8.71	2.401*
HUDF09	6237	23.51	< 0.10	> 10.00	10.72	1.30	14.40	1.965*
...

This is a sample of the full table, shown for illustrative purposes.

^aIDs correspond to NYU-VAGC IDs (Blanton et al., 2005) for the SDSS galaxies, and FIREWORKS IDs (Wuyts et al., 2008) for the HUDF galaxies

^bDerived from the SDSS g band imaging for the SDSS galaxies, and from the HST/WFC3 H_{160} band imaging for the HUDF09 galaxies

^cObtained from the Guo et al. (2009) catalog for the SDSS galaxies, and the Wuyts et al. (2008) catalog for the HUDF galaxies. Masses are corrected to account for the difference between the catalog magnitude and our measured magnitude.

*No spectroscopic redshifts are available for these galaxies; photometric redshifts are listed instead

tion fits to the full photometric data set (Förster Schreiber et al., in preparation), assuming a Kroupa IMF and the stellar population models of Bruzual & Charlot (2003). To study the morphological variation at $z \sim 2$, we select the 16 most massive galaxies with $1.5 < z < 2.5$. These galaxies have stellar masses between $1.2 \times 10^{10} M_\odot$ and $1.3 \times 10^{11} M_\odot$. Color images of these galaxies are shown in Figure 3.1a. A summary of their properties is given in Table 3.1.

From Figure 3.1a it is apparent that galaxies at $z \sim 2$ show a large variation in morphology, size and color. One can distinguish red, smooth, compact galaxies; blue galaxies with disk-like structures, some even with apparent spiral arms; and other star forming galaxies which appear more irregular. Most of the galaxies have a well-defined, red center. This is further illustrated in Figure 3.1b, where galaxy morphology is shown as a function of wavelength. Four massive galaxies are shown in the observed HST/ACS V_{606} band (Beckwith et al., 2006), HST/WFC3 H_{160} band and K_s band (based on ground-based imaging by Labbé et al., in preparation). The morphology of the sources differs strongly as a function of wavelength. The rest-frame UV morphology is more clumpy and extended than the rest-frame

optical morphology. In addition, the rest-frame optical images show well-defined centers for all sources, whereas these are often lacking in the rest-frame UV images. This confirms that the mass distribution of $z \sim 2$ galaxies is smoother and more centrally concentrated than would be concluded from rest-frame UV imaging (see e.g., Labbé et al. 2003b; Toft et al. 2005).

3.3 COLOR GRADIENTS AT $Z \sim 2$

In order to quantify the morphological properties of $z \sim 2$ galaxies we measure their surface brightness profiles. In contrast to conventional model-fitting techniques where a simple model is used to approximate the intrinsic surface brightness profile (e.g., using the GALFIT package of Peng et al. 2002), we measure the actual profile using the approach of Szomoru et al. (2010). The intrinsic profile is derived by fitting a Sérsic model profile convolved with the PSF to the observed flux, and then adding the residuals from this fit to the unconvolved model profile. Effectively, the model profile is used to deconvolve the majority of the observed flux, after which this deconvolved profile is combined with the residuals to account for deviations from the assumed model. Szomoru et al. (2010) have shown that it is thus possible to accurately measure the true intrinsic profiles out to large radii and very low surface brightness, even in cases where galaxies comprise a bright compact bulge and a faint extended disk.

In addition to the $z \sim 2$ galaxies we measure the profiles of galaxies at $z \sim 1$ and $z = 0$. The $z \sim 1$ sample is taken from the same dataset as the $z \sim 2$ sample, whereas the $z = 0$ galaxies are taken from the Guo et al. (2009) SDSS catalog of central galaxies. The galaxies are selected to lie in the same mass interval as the $z \sim 2$ sample: $1.2 \times 10^{10} M_{\odot} < M_{\text{stellar}} < 1.3 \times 10^{11} M_{\odot}$. The SDSS redshifts are required to be $z = 0.03 \pm 0.015$ and the $z \sim 1$ galaxies have $0.5 < z < 1.5$. This results in a sample of 27 galaxies at $z \sim 1$ and 84 galaxies at $z = 0$. Stellar masses and SSFRs for the SDSS sample are obtained from the MPA/JHU data release¹ (see Brinchmann et al. 2004; Salim et al. 2007 for details). A summary of the properties of the $z \sim 1$ and $z = 0$ galaxies is given in Table 3.1.

In Figure 3.2 we show surface density profiles, $u - g_{\text{rest}}$ color profiles, and $u - g_{\text{rest}}$ color gradients for galaxies in all three redshift bins. The surface density profiles are obtained by multiplying the surface brightness profiles in the H_{160} band (g band for the SDSS galaxies) with the galaxies' average M_{stellar}/L ratios in that band (where M_{stellar} is the total mass from the Wuyts et al. 2008 catalog (MPA/JHU catalog for the SDSS galaxies) and L is derived from the surface brightness profiles). This approach ignores gradients in the M_{stellar}/L ratios and is therefore not exact; however, it allows for a more quantitative comparison between galaxies at different redshifts and with different colors. The color gradients are derived from fits to the $u - g$ profiles between the half-width at half-maximum

¹<http://www.mpa-garching.mpg.de/SDSS/>

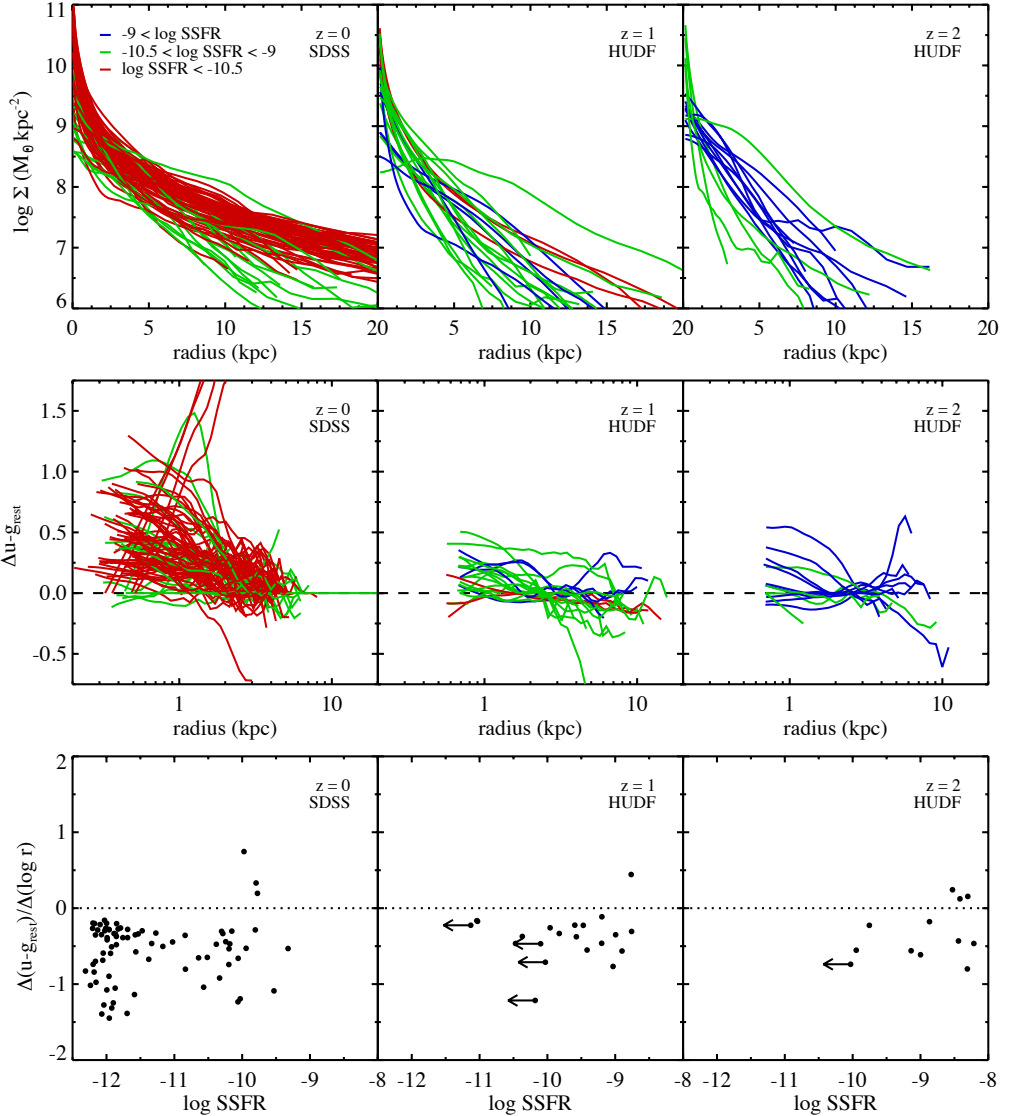


Figure 3.2: *Top panels:* surface density profiles of galaxies at $z = 0$, $z \sim 1$ and $z \sim 2$, color-coded according to specific star formation rate. The profiles are plotted up to the radius where uncertainties in the sky determination become significant. Surface density has been calculated from the average M/L_H (M/L_r for the SDSS galaxies) of the galaxy multiplied by the observed H_{160} (r_{625}) band surface brightness profile, ignoring gradients in the mass-to-light ratio. It is clear that a large diversity of profiles exists, with some close to exponential profiles and others close to $r^{1/4}$ profiles. This diversity extends to $z \sim 2$. *Middle panels:* $u - g_{\text{rest}}$ color profiles of the same galaxies. The profiles are normalized so that $\Delta u - g_{\text{rest}} = 0$ at $r = r_e$. The color profiles are plotted from the PSF HWHM (~ 0.6 arcsec for the SDSS galaxies, ~ 0.08 arcsec for the HUDF galaxies) to the radius where the errors in the flux measurement reach 20%. The color profiles show an overall trend of redder colors at smaller radii, in all redshift intervals. *Bottom panels:* $u - g_{\text{rest}}$ color gradients. Arrows indicate upper limits. Most $z \sim 2$ galaxies have negative color gradients. Color gradients do not seem to evolve very strongly between $z \sim 2$ and $z = 0$, for galaxies in the mass range considered here.

(HWHM) of the PSF (~ 0.6 arcsec for the SDSS galaxies, ~ 0.08 arcsec for the HUDF galaxies) and the radius where the errors in the flux measurement reach 20%.

The majority of $z \sim 2$ galaxies in our sample have negative color gradients, which do not vary strongly with redshift: $(\Delta(u - g_{rest})/\Delta(\log r))_{\text{median}} = -0.47_{-0.56}^{+0.20}$, $-0.33_{-0.23}^{+0.19}$ and $-0.46_{-0.28}^{+0.58}$ for $z \sim 2$, $z \sim 1$ and $z = 0$, respectively (where the errors give the $1\text{-}\sigma$ interval around the median). Thus, galaxy color gradients seem to be remarkably constant with redshift, both for quiescent and star-forming galaxies. It should be noted that this is not a comparison of low-redshift galaxies to their high-redshift progenitors; the $z \sim 2$ galaxies are expected to evolve into more massive galaxies at low redshift, due to mergers and accretion. Since we use mass-limited samples, the $z \sim 2$ galaxies we consider may fall outside of our mass-limits at low redshift. Selection by number density is better suited to trace the same population of galaxies across cosmic time (see, e.g., van Dokkum et al. 2010).

3.4 THE HUBBLE SEQUENCE FROM $Z \sim 2$ TO $Z = 0$

Finally, we study the relations between structure, color and SSFR as a function of redshift in Figure 3.3. In the top row we show Sérsic index against SSFR for the $z = 0$, $z \sim 1$ and $z \sim 2$ samples. In the bottom row we show Sérsic index against rest-frame $u - g$ color for the same galaxies. The Sérsic indices are derived from fits to the residual-corrected H_{160} -band (g -band for the $z = 0$ galaxies) surface brightness profiles. There is a clear relation between these parameters at all redshifts: star-forming galaxies have "diskier" (lower n) profiles and bluer colors than quiescent galaxies. There is a large variation in the SSFRs, colors and Sérsic indices of $z \sim 2$ galaxies, and the spread in these parameters is of roughly the same order of magnitude in all redshift bins. The relation shows systematic evolution: the median SSFR increases with increasing redshift and the median color and Sérsic index decrease, from $\log \text{SSFR} = -11.85_{-0.22}^{+1.67} \text{ yr}^{-1}$ at $z = 0$ to $\log \text{SSFR} = -8.87_{-0.58}^{+0.50} \text{ yr}^{-1}$ at $z \sim 2$, from $u - g_{rest} = 1.62_{-0.44}^{+0.38}$ to $u - g_{rest} = 0.87_{-0.33}^{+0.34}$, and from $n = 4.25_{-2.79}^{+1.71}$ to $n = 1.20_{-0.64}^{+2.16}$ (where the errors give the $1\text{-}\sigma$ interval around the median). These results are qualitatively consistent with the trends derived in e.g., Franx et al. (2008).

The relations between structure, color and SSFR are further illustrated in Figure 3.4, which shows rest-frame $u - g$ color images of a selection of galaxies at $z = 0$, $z \sim 1$ and $z \sim 2$, as a function of SSFR. From each redshift bin we select seven galaxies, evenly spaced in $\log \text{SSFR}$. This figure very clearly illustrates the morphological variety present at $z \sim 2$. Additionally, it confirms the relations shown in Figure 3.3: star-forming galaxies are blue and extended, while quiescent galaxies are red and relatively compact. Thus we find that the variation in galaxy structure at $z \sim 2$ is as large as at $z = 0$. Furthermore, the systematic relationships between different structural parameters are very similar between $z = 0$ and $z \sim 2$. This, in addition to the lack of evolution in the $u - g_{rest}$ color gradients shown in Figure 3.2, suggests that the underlying mechanisms that give rise to the Hubble sequence at $z = 0$ may already be in place at $z \sim 2$.

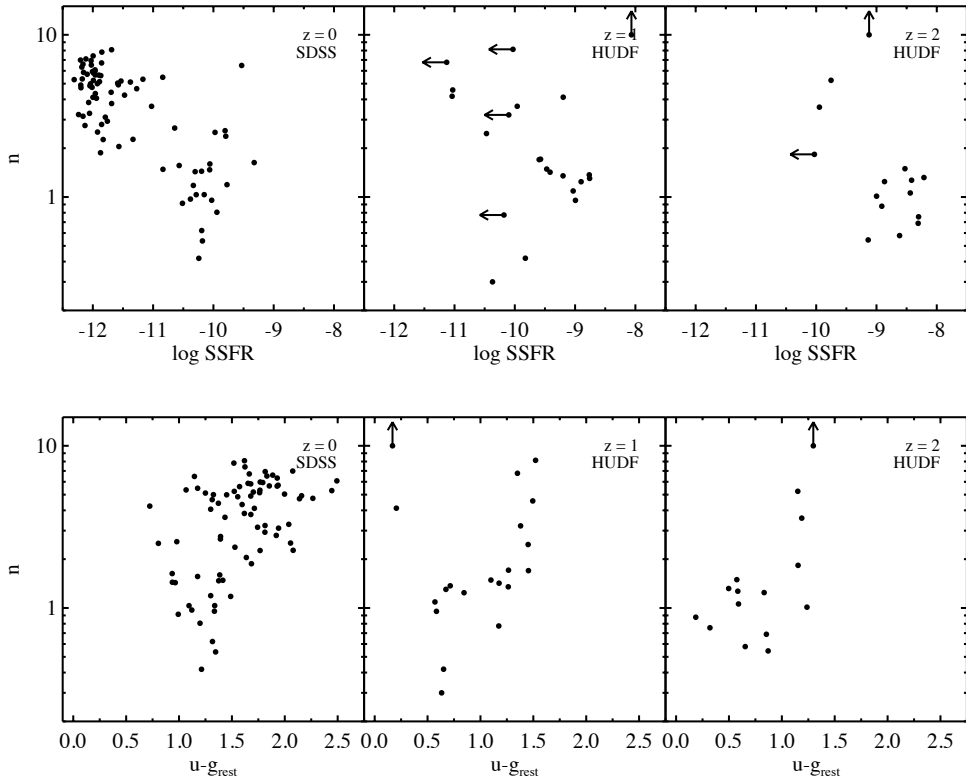


Figure 3.3: Sérsic index n plotted against SSFR (*top row*) and $u - g_{\text{rest}}$ color (*bottom row*) for galaxies with $1.2 \times 10^{10} M_{\odot} < M_{\text{stellar}} < 1.3 \times 10^{11} M_{\odot}$, at $z = 0$, $z \sim 1$ and $z \sim 2$. Arrows indicate upper or lower limits. Profile shape and SSFR are anticorrelated in all three wavelength bins, whereas profile shape and color show a positive correlation. The relations between these morphological parameters are similar in all three redshift bins, although on average galaxies are bluer and have higher SSFRs and lower Sérsic indices at high redshift. The similarity of the relations at $z = 0$ and $z \sim 2$ suggests that the Hubble sequence was already in place for massive galaxies at $z \sim 2$.

3.5 DISCUSSION

We have shown that the morphologies of massive $z \sim 2$ galaxies in the HUDF are complex and varied: from compact, apparently early-type galaxies to large star forming systems superficially similar to nearby spirals. Many of these galaxies seem to be composed of multiple components with large differences in stellar age. We conclude that the variety in morphologies which is observed at $z = 0$ also exists in galaxies at $z \sim 2$. This is confirmed by an analysis of the surface density profiles, which reveals a large range in profile shapes. The profiles of the large star forming systems are close to exponential, whereas the profiles of the quiescent systems are more concentrated. The correlations between morphology and SSFR are similar at all redshifts between $z = 0$ and $z \sim 2$.

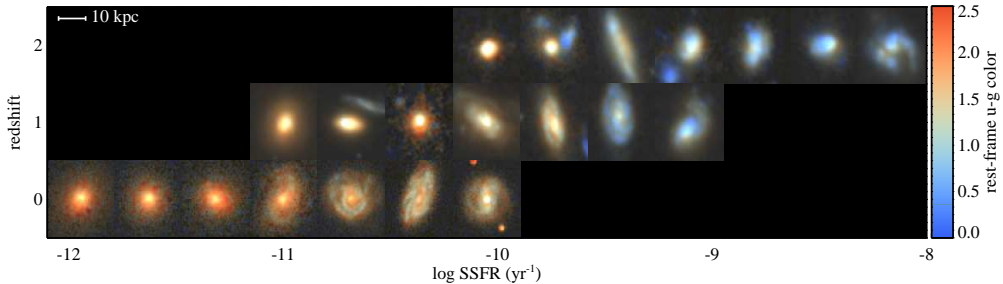


Figure 3.4: Galaxy morphologies from $z \sim 2$ to $z = 0$, as a function of SSFR. The colors of the galaxies have been obtained by scaling their rest-frame $u - g$ colors to the image's RGB space, as indicated by the color bar. The range in galaxy structure at $z \sim 2$ is very great, and is accompanied by a large range in galaxy colors. There is considerable evolution towards redder colors and lower SSFRs from $z \sim 2$ to $z = 0$. However, signs of a Hubble sequence (i.e., high-SSFR galaxies are "diskier", more extended and bluer than low-SSFR galaxies) appear to exist at $z \sim 2$.

This does not mean that morphologies and profiles are static: galaxies evolve quite strongly between $z = 2$ and $z = 0$. Quiescent galaxies are much more compact at high redshift, and cannot evolve passively into low-redshift quiescent galaxies (e.g., Daddi et al. 2005; Trujillo et al. 2006; Toft et al. 2007; van Dokkum et al. 2008). A similar size evolution is required for the star forming galaxies (e.g., Williams et al. 2010). We note that due to the evolution in the mass function of galaxies the $z \sim 2$ galaxies considered here will almost certainly not evolve into the low-redshift galaxies in this paper. It would be very informative to examine the morphologies of number density-limited galaxy samples over this redshift range, in order to investigate the evolution of the same galaxy population over time (e.g., van Dokkum et al. 2010).

Additionally, we have derived $u - g_{rest}$ color gradients of our galaxy sample, and have shown that massive $z \sim 2$ galaxies have negative color gradients that are comparable to those of low-redshift galaxies in the same mass range. These color gradients may partly be caused by radial variations in dust extinction, but radial changes in stellar populations likely play a large role (e.g., Abraham et al. 1999). This supports a galaxy growth scenario where small galaxies formed at high redshift grow by accreting material onto their outer regions. However, we lack the necessary information to rule out other possibilities; for example, if the gradients are caused by dust this might be an indication that these galaxies formed very quickly in a short burst.

The results seem to contrast with earlier analyses of galaxies at $z \sim 2$ in the HDFN (e.g., Dickinson 2000, Papovich et al. 2005). These authors concluded that all galaxies at this redshift are irregular and compact, with little difference between the rest-frame UV and optical. Field-to-field variations may play a role; as shown in Labbé et al. (2003a) the HDFN contains very few massive high-redshift galaxies. Indeed, the galaxies studied by these authors have lower masses ($M_{\text{stellar}} \lesssim 3 \times 10^{10} M_{\odot}$) than the galaxies we consider,

which could result in the difference with the study presented here. Additionally, We note that recent kinematical studies of massive $z \sim 2$ galaxies also indicate that many contain gas with ordered motion (e.g., Genzel et al. 2008, Förster Schreiber et al. 2009, Tacconi et al. 2010). The results presented in this Letter are fully consistent with those.

Our results raise the question at what redshift the first "ordered" galaxies appeared, with structures similar to the Hubble sequence. There are indications that at redshifts beyond 3 such galaxies may be much harder to find. Typical high-redshift Lyman break galaxies are very clumpy and irregular (e.g., Lowenthal et al. 1997), and differ significantly in appearance from regular spiral galaxies. Furthermore, the population of massive galaxies that are faint in the UV may be very small at redshifts beyond 3 (e.g., Brammer & van Dokkum 2007), at least in the mass regime that is considered in this paper (e.g., Marchesini et al. 2010). With current observational capabilities we are severely limited in studying the rest-frame optical properties of galaxies at redshifts beyond $z \sim 3.5$, due to rest-frame optical emission moving redward of the observers' K band. With improved capabilities it may become possible to study the red massive galaxy population at these redshifts. Several candidates have been found at $z > 5$ with significant Balmer discontinuities (Eyles et al. 2005; Mobasher et al. 2005; Wiklind et al. 2008; Richard et al. 2011), and many more are speculated to exist. These galaxies could very well be the centers of multi-component galaxies at redshifts between $z = 3$ and $z = 5$.

REFERENCES

- Abraham, R. G., Ellis, R. S., Fabian, A. C., Tanvir, N. R., & Glazebrook, K. 1999, MNRAS, 303, 641
- Beckwith, S. V. W., et al. 2006, AJ, 132, 1729
- Bell, E. F., et al. 2004, ApJ, 600, L11
- Blanton, M. R., et al. 2005, AJ, 129, 2562
- Bond, N. A., Gawiser, E., & Koekemoer, A. M. 2010, arXiv:1010.1525
- Bouwens, R. J., et al. 2010, ApJ, 709, L133
- Brammer, G. B., & van Dokkum, P. G. 2007, ApJ, 654, L107
- Brammer, G. B., van Dokkum, P. G., & Coppi, P. 2008, ApJ, 686, 1503
- Brinchmann, J., Charlot, S., White, S. D. M., Tremonti, C., Kauffmann, G., Heckman, T., & Brinkmann, J. 2004, MNRAS, 351, 1151
- Bruzual, G., & Charlot, S. 2003, MNRAS, 344, 1000
- Cameron, E., Carollo, C. M., Oesch, P. A., Bouwens, R. J., Illingworth, G. D., Trenti, M., Labbé, I., & Magee, D. 2010, arXiv:1007.2422
- Daddi, E., et al. 2005, ApJ, 626, 680
- de Vaucouleurs, G. H. 1959, Lowell Observatory Bulletin, 4, 105
- Dickinson, M. 2000, Philosophical Transactions of the Royal Society of London, Series A, 358, 2001
- Eyles, L. P., Bunker, A. J., Stanway, E. R., Lacy, M., Ellis, R. S., & Doherty, M. 2005, MNRAS, 364, 443
- Förster Schreiber, N. M., et al. 2009, ApJ, 706, 1364
- Franx, M., van Dokkum, P. G., Schreiber, N. M. F., Wuyts, S., Labbé, I., & Toft, S. 2008, ApJ, 688, 770
- Genzel, R., et al. 2008, ApJ, 687, 59
- Guo, Y., et al. 2009, MNRAS, 398, 1129
- Hubble, E. P. 1926, ApJ, 64, 321
- Kauffmann, G., et al. 2003, MNRAS, 341, 54
- Kriek, M., van Dokkum, P. G., Franx, M., Illingworth, G. D., & Magee, D. K. 2009, ApJ, 705, L71
- Labbé, I., et al. 2003a, AJ, 125, 1107
- Labbé, I., et al. 2003b, ApJ, 591, L95
- Lowenthal, J. D., et al. 1997, ApJ, 481, 673
- Marchesini, D., et al. 2010, ApJ, 725, 1277
- Mobasher, B., et al. 2005, ApJ, 635, 832
- Oesch, P. A., et al. 2010, ApJ, 709, L16
- Papovich, C., Dickinson, M., Giavalisco, M., Conselice, C. J., & Ferguson, H. C. 2005, ApJ, 631, 101
- Peng, C. Y., Ho, L. C., Impey, C. D., & Rix, H.-W. 2002, AJ, 124, 266
- Richard, J., Kneib, J.-P., Ebeling, H., Stark, D., Egami, E., & Fiedler, A. K. 2011, arXiv:1102.5092
- Roberts, M. S., & Haynes, M. P. 1994, ARA&A, 32, 115

Salim, S., et al. 2007, *ApJS*, 173, 267
Sandage, A., & Tammann, G. A. 1981, Washington: Carnegie Institution, 1981, Preliminary version
Szomoru, D., et al. 2010, *ApJ*, 714, L244
Tacconi, L. J., et al. 2010, *Nature*, 463, 781
Toft, S., van Dokkum, P., Franx, M., Thompson, R. I., Illingworth, G. D., Bouwens, R. J., & Kriek, M. 2005, *ApJ*, 624, L9
Toft, S., et al. 2007, *ApJ*, 671, 285
Trujillo, I., et al. 2006, *ApJ*, 650, 18
van Dokkum, P. G., et al. 2008, *ApJ*, 677, L5
van Dokkum, P. G., et al. 2010, *ApJ*, 709, 1018
Wiklind, T., Dickinson, M., Ferguson, H. C., Giavalisco, M., Mobasher, V., Grogin, N. A., & Panagia, N. 2008, *ApJ*, 676, 781
Williams, R. J., Quadri, R. F., Franx, M., van Dokkum, P., Toft, S., Kriek, M., & Labbé, I. 2010, *ApJ*, 713, 738
Wuyts, S., Labbé, I., Schreiber, N. M. F., Franx, M., Rudnick, G., Brammer, G. B., & van Dokkum, P. G. 2008, *ApJ*, 682, 985
York, D. G., et al. 2000, *AJ*, 120, 1579

SIZES AND SURFACE BRIGHTNESS PROFILES OF QUIESCENT GALAXIES AT $z \sim 2$

We use deep *Hubble Space Telescope* Wide Field Camera 3 near-infrared imaging obtained of the GOODS-South field as part of the CANDELS survey to investigate a stellar mass-limited sample of quiescent galaxies at $1.5 < z < 2.5$. We measure surface brightness profiles for these galaxies using a method that properly measures low surface brightness flux at large radii. We find that quiescent galaxies at $z \sim 2$ very closely follow Sérsic profiles, with $n_{median} = 3.7$, and have no excess flux at large radii. Their effective radii are a factor ~ 4 smaller than those of low-redshift quiescent galaxies of similar mass. However, there is significant spread in sizes ($\sigma_{\log_{10} r_e} = 0.24$), with the largest $z \sim 2$ galaxies lying close to the $z = 0$ mass-size relation. We compare the stellar mass surface density profiles with those of massive elliptical galaxies in the Virgo cluster and confirm that most of the mass-growth which occurs between $z \sim 2$ and $z = 0$ must be due to accretion of material onto the outer regions of the galaxies. Additionally, we investigate the evolution in the size distribution of massive quiescent galaxies. We find that the minimum size growth required for $z \sim 2$ quiescent galaxies to fall within the $z = 0$ size distribution is a factor ~ 2 smaller than the total median size growth between $z \sim 2$ and $z = 0$.

4.1 INTRODUCTION

Quiescent galaxies make up a considerable fraction of the massive galaxy population at $z = 2$ (e.g., Franx et al. 2003; Daddi et al. 2005; Kriek et al. 2006). Their structural evolution has been the subject of considerable discussion, focusing in particular on their extremely compact nature compared to low redshift galaxies of similar mass (e.g., Daddi et al. 2005; Trujillo et al. 2006; Toft et al. 2007; van der Wel et al. 2008; van Dokkum et al. 2008; Damjanov et al. 2009; Hopkins et al. 2009; Saracco et al. 2009; van Dokkum et al. 2009; Cassata et al. 2010; Mancini et al. 2010; Cassata et al. 2011). The early formation and subsequent evolution of these massive, compact objects presents a considerable challenge to current models of galaxy formation and evolution (e.g., Wuyts et al. 2010; Oser et al. 2012). It is unclear what the structure of the progenitors of these galaxies is, and the lack of extremely compact massive galaxies at low redshift implies considerable size evolution between $z = 2$ and $z = 0$ (Trujillo et al. 2009; Taylor et al. 2010). However, efforts to accurately quantify this evolution are hindered by uncertainties. The apparent compactness of $z \sim 2$ quiescent galaxies may simply be an observational effect: photometric masses may be systematically overestimated due to modeling uncertainties, and sizes may be underestimated due to a lack of imaging depth (Hopkins et al. 2009; Muzzin et al. 2009).

Due to the difficulty of obtaining high-quality spectra of quiescent galaxies at $z > 1.5$, dynamical masses have only been measured for a few such galaxies (Cappellari et al. 2009; Cenarro & Trujillo 2009; van Dokkum et al. 2009; Onodera et al. 2010; van de Sande et al. 2011). Instead, photometric stellar masses are used, which are subject to considerable uncertainties due to e.g., the quality of the stellar libraries used in modeling the spectral energy distribution (SED), or incorrect assumptions about the shape of the initial mass function (IMF). These uncertainties can result in systematic errors of up to a factor ~ 6 (Conroy et al., 2009). At low redshift there is good agreement between stellar masses determined by photometric SED fitting methods and dynamical masses (Taylor et al. 2010). Whether this is also the case at high redshift is unclear (e.g., van de Sande et al. 2011; Bezanon et al. 2011; Martinez-Manso et al. 2011).

The second large source of uncertainty lies in the size determination of these galaxies. The compact objects observed at $z \sim 2$ may be surrounded by faint extended envelopes of material, which could be undetected by all but the deepest data. Stacking studies have been used to obtain constraints on the average surface brightness profile of compact galaxies (e.g., van der Wel et al. 2008; van Dokkum et al. 2008; Cassata et al. 2010). However, detailed analysis of individual galaxies is more difficult, primarily due to the limited number of compact galaxies for which ultradeep near-infrared (NIR) data are available. Szomoru et al. (2010) carried out an analysis on a $z = 1.91$ compact quiescent galaxy in the Hubble Ultra Deep Field (HUDF) and confirmed its small size.

In this Paper we expand the analysis of Szomoru et al. (2010) using a stellar mass-limited sample of 21 quiescent galaxies. We make use of deep *Hubble Space Telescope* Wide Field Camera 3 (*HST* WFC3) data from the CANDELS GOODS-South observations to investigate the surface brightness profiles of quiescent galaxies at $z \sim 2$. These observations

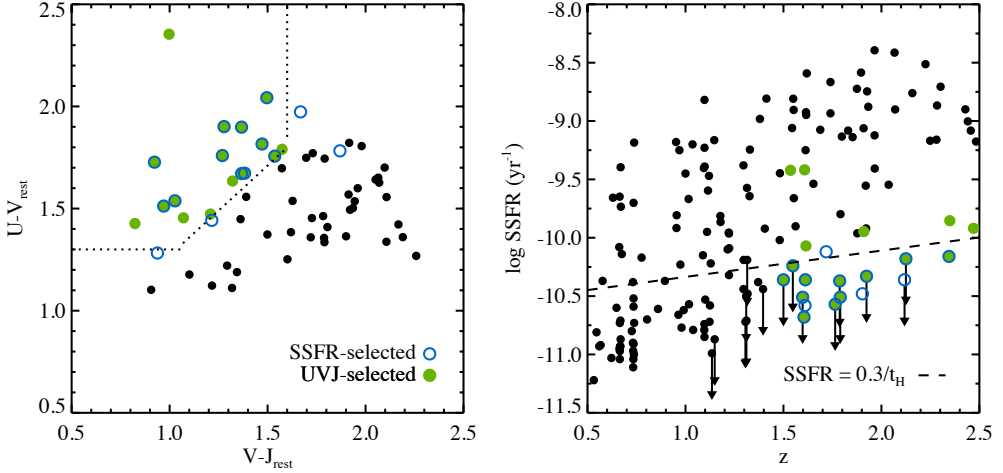


Figure 4.1: Left panel: rest-frame $U - V$ and $V - J$ colors of galaxies in the CANDELS GOODS-South deep field at $1.5 < z < 2.5$. Right panel: specific star formation rates as a function of redshift. Arrows indicate upper limits. The dashed line indicates where the specific star formation rate is equal to $0.3/t_H$. Quiescent galaxies selected using the UVJ color criterion are shown as filled green circles. Galaxies which are selected as quiescent based on their SSFRs are shown as open blue circles. There is good agreement between the two selection criteria. Both the UVJ -selected galaxies and the SSFR-selected galaxies are included in our quiescent galaxy sample.

are not as deep as the HUDF data, but cover a much larger area, allowing us to study a statistically more meaningful sample. We measure the surface brightness profile of each individual galaxy and investigate deviations from Sérsic profiles. Additionally, we compare the size distribution and profile shapes of $z \sim 2$ galaxies to those of low redshift quiescent galaxies. Throughout the Paper, we assume a Λ CDM cosmology with $\Omega_m = 0.3$, $\Omega_\Lambda = 0.7$ and $H_0 = 70 \text{ km s}^{-1} \text{ Mpc}^{-1}$. All stellar masses are derived assuming a Kroupa IMF (Kroupa, 2001). All effective radii are circularized and magnitudes are in the AB system.

4.2 DATA AND SAMPLE SELECTION

We use NIR data taken with *HST* WFC3 as part of the CANDELS survey (Grogin et al. 2011; Koekemoer et al. 2011). This survey will target approximately 700 square arcminutes to 2 orbit depth in Y_{105} , J_{125} and H_{160} (COSMOS, EGS and UDS fields), as well as ~ 120 square arcminutes to 12 orbit depth (GOODS-South and GOODS-North fields). These NIR observations are complemented with parallel *HST* ACS exposures in V_{606} and I_{814} . We use the deepest publicly available data, reduced by Koekemoer et al. (2011), which consist of I_{814} , J_{125} and H_{160} observations to 4-orbit depth of a ~ 60 square arcminute section of the GOODS-South field. The full width at half-maximum of the point-spread function (PSF) is ≈ 0.18 arcsec for the WFC3 observations and ≈ 0.11 arcsec for the ACS

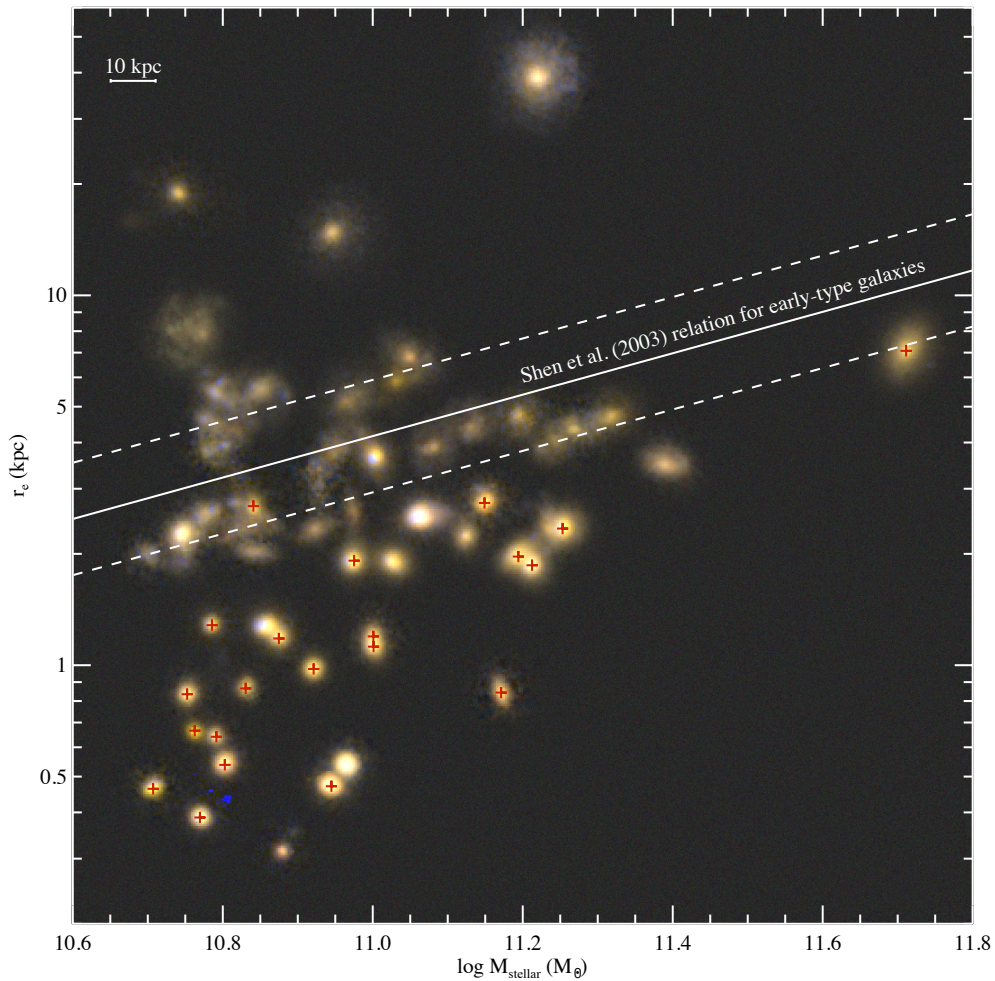


Figure 4.2: Stellar masses and sizes of galaxies at $1.5 < z < 2.5$ with $M_{stellar} > 5 \times 10^{10} M_{\odot}$. Color images are composed of rest-frame U_{336} , B_{438} and g_{475} images, obtained from observed I_{814} , J_{125} and H_{160} images. Galaxies which are included in our quiescent sample are indicated with red crosses. Although we do not select based on morphology, almost all galaxies in our quiescent sample are compact, bulge-dominated, and have red colors.

observations. The images have been drizzled to a pixel size of 0.06 arcsec for the WFC3 observations and 0.03 arcsec for the ACS observations (see Koekemoer et al. (2011) for details).

Galaxies are selected in the GOODS-South field using the K_s -selected FIREWORKS catalog (Wuyts et al., 2008). This catalog combines observations of the Chandra Deep Field South ranging from ground-based U -band data to *Spitzer* $24\ \mu\text{m}$ data, and includes spectroscopic redshifts where available, as well as photometric redshifts derived using EAZY (Brammer et al., 2008). These photometric redshifts have a median $\Delta z/(1+z) = -0.001$ with a normalized median absolute deviation of $\sigma_{\text{NMAD}} = 0.032$ (Wuyts et al., 2008). Stellar masses were estimated from SED fits to the full photometric data set (N. M. Förster Schreiber et al. 2012, in preparation), assuming a Kroupa IMF and the stellar population models of Bruzual & Charlot (2003).

We select all galaxies with $1.5 < z < 2.5$ and stellar masses above $5 \times 10^{10} M_{\odot}$, which is the completeness limit in this redshift range (Wuyts et al., 2009). In order to ensure that we include all quiescent galaxies we explore both a color-color selection (the UVJ selection described in Williams et al. (2009)) and a selection based on specific star formation rate (SSFR). In the left panel of Figure 4.1 we show the rest-frame $U - V$ and $V - J$ colors of all $z \sim 2$ galaxies in the field. The dashed lines indicate the quiescent galaxy selection limits from Williams et al. (2009). Galaxies which fall within the dashed lines (green dots) have SEDs that are consistent with red, quiescent galaxies. Patel et al. (2012) have shown that this selection method is very effective at separating dust-reddened starforming galaxies from truly quiescent galaxies. As an alternative to the UVJ selection we also select galaxies based on their SSFR. In the right-hand panel of Figure 4.1 we show the SSFRs of galaxies as a function of redshift. The SSFRs are estimated from the UV and $24\ \mu\text{m}$ fluxes, as discussed in Wuyts et al. (2009). The dashed line shows our selection limit, below which the SSFR is lower than $0.3/t_H$, where t_H is the Hubble time. There is generally very good agreement between the two selection criteria, although several galaxies that seem to be quiescent based on their SSFRs are not selected by the UVJ method, and vice versa. We find no significant difference in the distribution of structural parameters of galaxies selected by either method; the median values are equal to within 6 percent, for the effective radii, Sérsic indices and axis ratios. This is expected, given the large overlap between the two samples. Since we wish to be as complete as possible we combine the two selection methods and include all galaxies selected by either method. This results in a sample of 21 quiescent galaxies, whose properties are summarized in Table 4.1.

To illustrate the effects of our selection on galaxy morphology we show color images of all galaxies with $1.5 < z < 2.5$ and $M_{\text{stellar}} > 5 \times 10^{10} M_{\odot}$ in the stellar mass-size plane in Figure 4.2. The color images are constructed from PSF-matched rest-frame U_{336} , B_{438} and g_{475} images, obtained by interpolating between the observed I_{814} , J_{125} and H_{160} images. Although we do not select based on morphology, the galaxies in our quiescent sample (indicated with red crosses) are generally very compact, bulge-dominated systems with relatively red colors. Interestingly, all starforming systems at $z \sim 2$ appear to have a well-defined red core, as was also pointed out by Szomoru et al. (2011) (but also see, e.g.,

4.3 MEASURING SURFACE BRIGHTNESS PROFILES

Obtaining surface brightness profiles of high-redshift galaxies is difficult, in large part due to the small size of these galaxies compared to the PSF. Direct deconvolution of the observed images is subject to large uncertainties. A common approach is therefore to fit two-dimensional models, convolved with a PSF, to the observed images. Sérsic (1968) profiles are commonly used, since these have been shown to closely match the surface brightness profiles of nearby early-type galaxies (e.g., Caon et al. 1993; Graham et al. 2003; Trujillo et al. 2004; Ferrarese et al. 2006; Côté et al. 2007; Kormendy et al. 2009). However, there is no reason that high-redshift galaxies should exactly follow Sérsic profiles.

An obvious way to account for deviations from a Sérsic profile is by using double-component fits, in which the deviations are approximated by a second Sérsic profile. Although this provides a closer approximation to the true surface brightness profile than a one-component fit, it still depends on assumptions regarding the shape of the profile. We therefore use a technique which is more robust to deviations from the assumed model and accurately recovers the true intrinsic profile. This technique was first used in Szomoru et al. (2010); we summarize it here. First, we use the GALFIT package (Peng et al., 2002) to perform a conventional two-dimensional Sérsic profile fit to the observed image. For PSFs we use unsaturated stars brighter than $K = 22.86$ that are not contaminated by nearby sources. We verify the quality of our stellar PSFs by comparing their radial profiles to each other, and find that the profiles show small variations in half-light radius of order $\sim 2\%$. We find no systematic dependence of these variations with magnitude. In order to estimate the effects of PSF variations on our derived parameters we fit every galaxy using each of the stars separately. We find that the derived total magnitudes, sizes and Sérsic indices vary by about 0.1%, 3% and 7%, respectively.

After fitting a Sérsic model profile we measure the residual flux profile from the residual image, which is the difference between the observed image and the best-fit PSF-convolved model. This is done along concentric ellipses which follow the geometry of the best-fit Sérsic model. The residual flux profile is then added to the best-fit Sérsic profile, effectively providing a first-order correction to the profile at those locations where the assumed model does not accurately describe the data. The effective radius is then calculated by integrating the residual-corrected profile out to a radius of approximately 12 arcseconds (~ 100 kpc at $z \sim 2$). We note that the residual flux profile is not deconvolved for PSF; however, we show below that this does not strongly affect the accuracy of this method.

Errors in the sky background estimate are the dominant source of uncertainty when deriving surface brightness profiles of faint galaxies to large radii. Using the wrong sky value can result in systematic effects. GALFIT provides an estimate of the sky background during fitting. To ensure that this estimate is correct we inspect the residual flux profile of each galaxy at radii between 5 and 15 arcsec (approximately 40 to 120 kpc at $z = 2$). Using

Table 4.1: Galaxy properties.

ID ^a	z	R.A.	Dec	M_*^b ($\log M_\odot$)	SSFR ($\log \text{yr}^{-1}$)	U-V _{rest}	V-J _{rest}	$\text{mag}_{H\alpha, \text{pp}}^c$ (AB)	r_e^c (kpc)	n^c	b/a	P.A. ^d (deg)
1060	2.345*	53.069829	-27.880467	11.14	-10.16	1.75	0.92	22.21 ± 0.05	2.75 ± 1.60	9.21 ± 1.10	0.70 ± 0.01	-45.2 ± 1.6
1088	1.752*	53.065570	-27.878805	10.75	-10.12	1.28	0.94	21.84 ± 0.03	0.83 ± 0.11	5.50 ± 0.67	0.87 ± 0.02	-62.5 ± 13.1
1289	1.759*	53.116186	-27.871904	11.00	-10.51	2.04	1.50	22.35 ± 0.22	1.20 ± 0.22	3.26 ± 0.40	0.58 ± 0.01	-8.5 ± 0.8
1831	1.536	53.076366	-27.848700	11.25	-9.42	1.47	1.21	20.71 ± 0.02	2.34 ± 0.33	3.68 ± 0.16	0.92 ± 0.01	-44.6 ± 3.2
1971	1.608	53.150661	-27.843604	10.84	-9.42	1.63	1.32	21.71 ± 0.03	2.69 ± 0.79	5.07 ± 0.31	0.87 ± 0.01	27.0 ± 2.1
2227	1.612	53.150165	-27.834522	10.98	-10.36	1.54	1.03	21.40 ± 0.02	1.92 ± 0.26	3.76 ± 0.15	0.84 ± 0.01	-6.5 ± 2.1
2514	1.548*	53.151413	-27.825886	10.79	-10.24	1.67	1.38	21.96 ± 0.06	1.28 ± 0.29	5.73 ± 0.93	0.86 ± 0.03	7.0 ± 5.9
2531	1.598*	53.171735	-27.825672	10.87	-10.51	1.90	1.28	21.93 ± 0.02	1.18 ± 0.12	4.08 ± 0.30	0.95 ± 0.02	7.6 ± 11.6
2856	1.759*	53.216633	-27.814310	10.83	-10.37	1.76	1.54	22.90 ± 0.01	0.87 ± 0.03	1.20 ± 0.08	0.63 ± 0.02	-16.5 ± 1.0
2993	2.470	53.163233	-27.808962	10.71	-9.92	2.35	1.00	23.38 ± 0.02	0.46 ± 0.04	1.01 ± 0.09	0.32 ± 0.04	-63.1 ± 1.0
3046	2.125*	53.116519	-27.806731	10.80	-10.18	1.51	0.97	22.22 ± 0.02	0.54 ± 0.02	3.59 ± 0.34	0.70 ± 0.02	-45.8 ± 3.0
3119	2.349	53.123107	-27.803355	10.94	-9.85	1.43	0.82	21.97 ± 0.03	0.47 ± 0.06	5.09 ± 0.60	0.49 ± 0.04	79.2 ± 1.5
3242	1.910	53.158831	-27.797119	10.77	-9.95	1.45	1.07	22.10 ± 0.02	0.39 ± 0.03	4.17 ± 0.45	0.62 ± 0.03	57.1 ± 3.0
3548	1.500*	53.202356	-27.785436	10.76	-10.36	1.67	1.37	22.40 ± 0.03	0.67 ± 0.05	3.75 ± 0.48	0.65 ± 0.04	55.5 ± 2.4
3829	1.924*	53.069966	-27.768143	10.79	-10.33	1.90	1.37	22.85 ± 0.05	0.64 ± 0.14	4.24 ± 1.15	0.66 ± 0.03	44.7 ± 3.2
4850	2.118*	53.012891	-27.705730	11.17	-10.36	1.97	1.67	22.68 ± 0.02	0.84 ± 0.09	2.72 ± 0.42	0.20 ± 0.02	17.0 ± 0.3
5890	1.756*	53.174620	-27.753362	10.92	-10.57	1.76	1.27	22.09 ± 0.01	0.98 ± 0.04	1.89 ± 0.12	0.92 ± 0.02	-14.6 ± 3.6
6097	1.903	53.140997	-27.766706	11.21	-10.48	1.44	1.22	21.30 ± 0.03	1.86 ± 0.43	5.26 ± 0.56	0.79 ± 0.02	2.8 ± 2.2
6187	1.610	53.044923	-27.774363	11.71	-10.58	1.76	1.87	20.37 ± 0.01	7.08 ± 1.30	2.77 ± 0.05	0.61 ± 0.01	-30.1 ± 0.2
6194	1.605	53.052217	-27.774766	11.19	-10.68	1.82	1.47	21.18 ± 0.02	1.97 ± 0.14	2.04 ± 0.06	0.57 ± 0.01	-56.3 ± 0.4
6246	1.615	53.043813	-27.774666	11.00	-10.07	1.76	1.57	21.71 ± 0.03	1.12 ± 0.16	10.10 ± 2.38	0.64 ± 0.02	-19.6 ± 1.5

^aFIREWORKS ID (Wuyts et al., 2008)

^bMasses are corrected to account for the difference between the catalog magnitude and our measured magnitude.

^cMagnitudes, effective radii and Sérsic indices are derived from the H_{160} band residual-corrected profiles discussed in Section 4.4.

^dPosition angles are measured counterclockwise with respect to North.

* No spectroscopic redshifts are available for these galaxies; photometric redshifts are listed instead

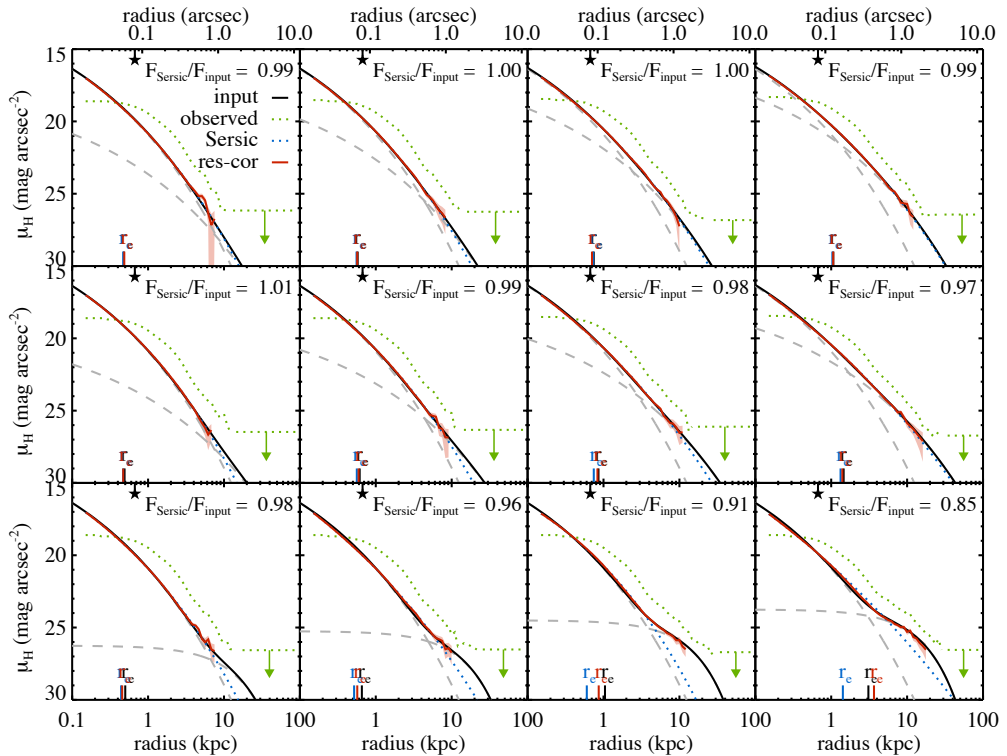


Figure 4.3: Effectiveness of the residual-correction for recovering surface brightness profiles. The method was tested on a large number of simulated galaxies, composed of two components: one compact bright component, and an extended fainter component. A small selection is shown here. The input profiles are shown in black, with the dashed grey lines indicating the two subcomponents. The PSF-convolved “observed” profiles are shown in green. Direct Sérsic fits are shown in blue, and the residual-corrected profiles are overplotted in red. The shaded light red regions indicate the $1\text{-}\sigma$ errors due to uncertainty in the sky estimation. The size of the PSF half width at half maximum (HWHM) is indicated on the top axis of each panel. Input effective radii are indicated in black on the bottom axes. Effective radii derived from the direct Sérsic fits and from the residual-corrected profiles are indicated in blue and red, respectively. The fraction of the input flux within 10 kpc recovered by the Sérsic fits $F_{\text{Sersic}}/F_{\text{input}}$ is given in each panel. The residual-corrected profiles clearly reproduce the input profiles more accurately than the simple Sérsic fits, especially at large radii.

this portion of the residual flux profile we derive a new sky value and adjust the intensity profile accordingly. We use the difference between the minimum and maximum values of the residual flux profile within this range of radii as an estimate of the uncertainty in the sky determination.

In Szomoru et al. (2010) this procedure was tested using simulated galaxies inserted into *HST* WFC3 data of the HUDF. Since the data used in this Paper are shallower we have performed new tests. We create images of simulated galaxies that consist of two components: one compact elliptical component and a larger, fainter component that ranges from disk-like

Table 4.2: Surface brightness profiles.

ID ^a	r_{arcsec} (arcsec)	r_{kpc} (kpc)	μ_H (AB mag arcsec ⁻²)	$\log \Sigma$ (log M_{\odot} kpc ⁻²)
1060	0.0180	0.147	18.413 ± 0.0010	10.843 ± 0.0004
1060	0.0198	0.162	18.548 ± 0.0011	10.789 ± 0.0005
1060	0.0216	0.177	18.673 ± 0.0013	10.739 ± 0.0005
1060	0.0240	0.196	18.826 ± 0.0015	10.678 ± 0.0006
1060	0.0264	0.216	18.966 ± 0.0019	10.622 ± 0.0007
1060	0.0288	0.235	19.095 ± 0.0021	10.570 ± 0.0008
1060	0.0318	0.260	19.244 ± 0.0024	10.510 ± 0.0010
1060	0.0348	0.285	19.382 ± 0.0027	10.455 ± 0.0011
1060	0.0384	0.314	19.534 ± 0.0032	10.395 ± 0.0013
1060	0.0426	0.348	19.696 ± 0.0037	10.330 ± 0.0015
...

This is a sample of the full table, shown for illustrative purposes.

^aFIREWORKS ID (Wuyts et al., 2008)

to elliptical. The axis ratio and position angle of the second component are varied, as are its effective radius and total magnitude. The simulated galaxies are convolved with a PSF (obtained from the data) and are placed in empty areas of the observed H_{160} band image. We then run the procedure described above to extract surface brightness profiles and compare them to the input profiles.

A selection of these simulated profiles is shown in Figure 4.3. The input profiles are shown as solid black lines. The dashed grey lines indicate the two subcomponents of each simulated galaxy. The directly measured profiles are shown in green. The best-fit Sérsic models are shown in blue, and the residual-corrected profiles are shown in red. The residual-corrected profiles are plotted up to the radius where the uncertainty in the sky determination becomes significant. The effectiveness of the residual-correction method is clear: whereas a simple Sérsic fit in many cases under- or overpredicts the flux at $r > 5$ kpc, the residual-corrected profiles follow the input profiles extremely well up to the sky threshold (~ 10 kpc). The recovered flux within 10 kpc is on average 95% of the total input flux, with a 1- σ spread of 2%. Recovered effective radii are less accurate, as this quantity depends quite strongly on the extrapolation of the surface brightness profile to radii beyond 10 kpc. However, effective radii derived from the residual-corrected profiles are generally closer to the true effective radii than those derived from simple Sérsic fits.

4.4 MISSING FLUX IN COMPACT QUIESCENT $z \sim 2$ GALAXIES

We now use the residual-correction method to derive the surface brightness profiles of the $z \sim 2$ quiescent galaxies. The results are shown in Figures 4.4 and 4.4. The SEDs, shown in the top row, illustrate the low levels of UV and IR emission of the quiescent galaxies in our sample. Rest-frame color images are shown in the second row. These images indicate that the

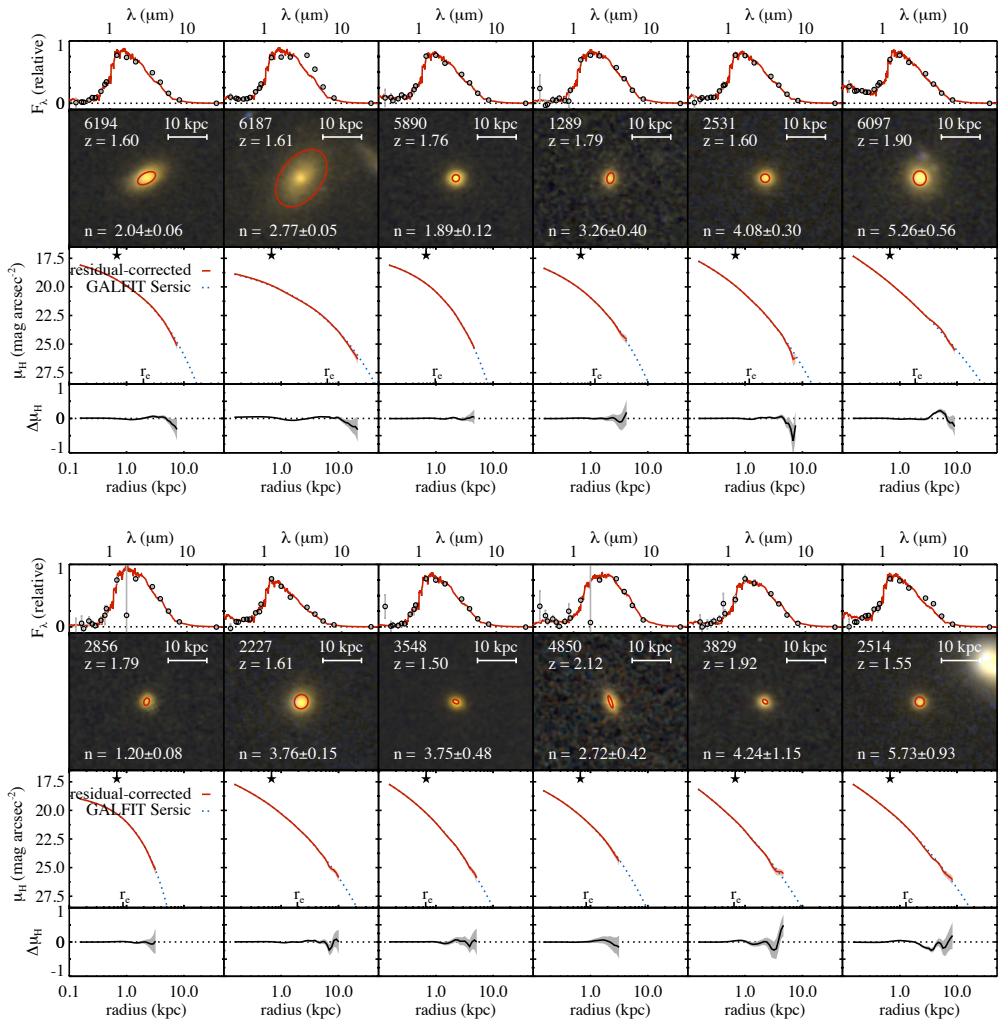


Figure 4.4: Broadband SEDs, color images and PSF-corrected surface brightness profiles of $z \sim 2$ quiescent galaxies. The SEDs, obtained with FAST (Kriek et al., 2009), are based on photometry from the FIREWORKS catalog. The color images are composed of rest-frame U_{336} , B_{438} and g_{475} images, obtained from the observed I_{814} , J_{125} and H_{160} data. The red ellipses are constructed from the best-fitting effective radii, axis ratios, and position angles. The best-fit Sérsic profiles, obtained using GALFIT, are indicated by blue dotted curves. Residual-corrected surface brightness profiles are shown in red. Effective radii and the PSF HWHM are indicated at the bottom and top axes, respectively. We are able to measure the true surface brightness profiles of these galaxies down to approximately $26 \text{ mag arcsec}^{-2}$ and out to $r \approx 10 \text{ kpc}$. In the bottom row we show the difference between the best-fit Sérsic profile and the residual-corrected profile. Individual residual-corrected profiles show deviations from simple Sérsic profiles, although these deviations are consistent with zero within the errors.

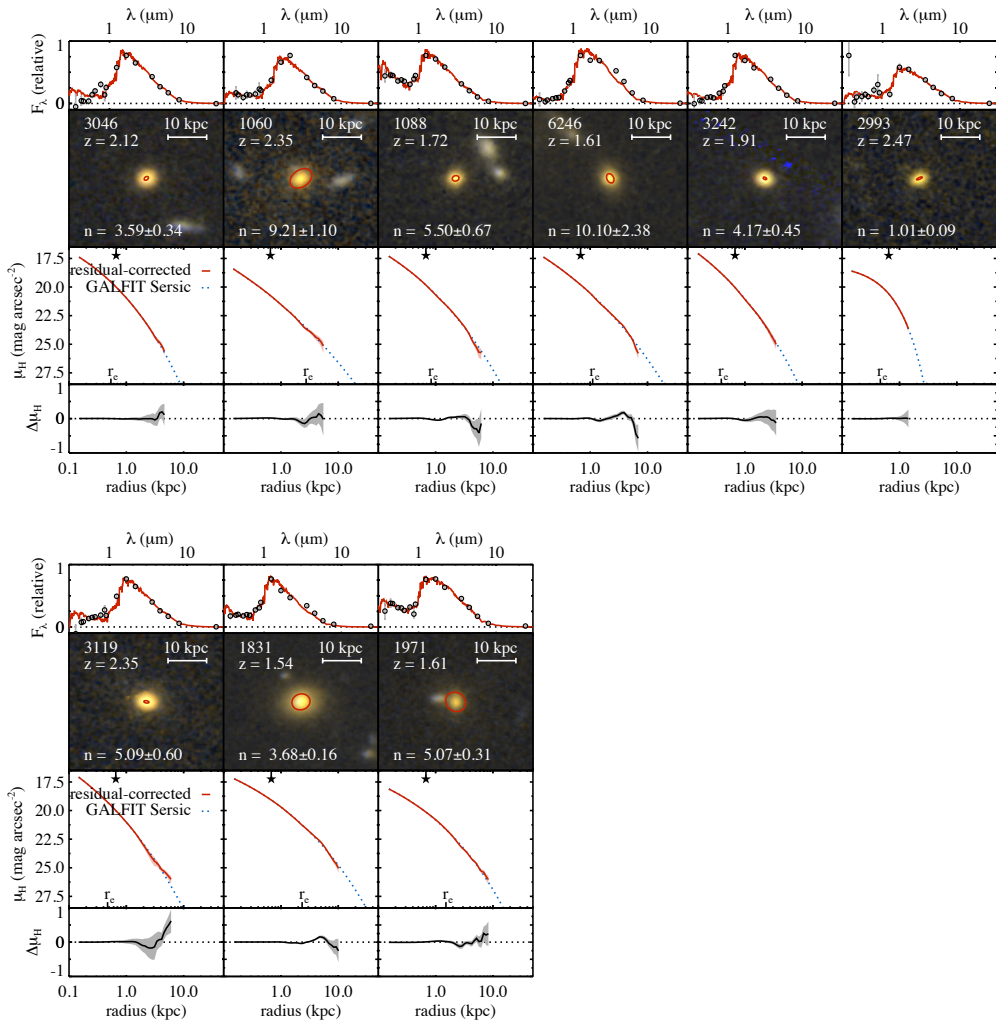


Figure 4.4: Continued.

galaxies in this sample generally have compact elliptical morphologies. Some galaxies have a nearby neighbor; in these cases we simultaneously fit both objects to account for possible contamination by flux from the companion object. In the third row, best-fit Sérsic profiles are shown in blue and residual-corrected profiles in red. The residual-corrected profiles follow the Sérsic profiles remarkably well. Most galaxies deviate slightly at large radii. The difference between the best-fit Sérsic profiles and the residual-corrected profiles are shown in the bottom row. The deviations are generally small within $2r_e$; for some galaxies larger deviations occur at larger radii, but in these cases the uncertainty is very high due to the uncertain sky. Overall, the profiles are consistent with simple Sérsic profiles. The profiles are given in Table 4.2, and can also be downloaded from <http://www.strw.leidenuniv.nl/~szomoru/>

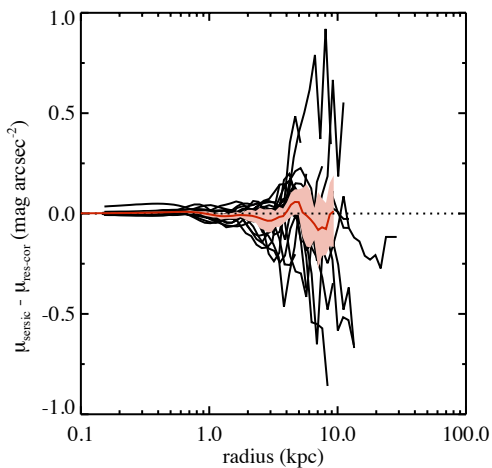


Figure 4.5: Deviations of galaxy profiles from Sérsic profiles. The difference between the best-fit Sérsic profile and the residual-corrected profile is plotted as a function of radius for all galaxies in our sample (black lines). The mean profile is shown in red, with the shaded light red region indicating the $1 - \sigma$ spread in the distribution. Although individual galaxy profiles deviate from Sérsic profiles, on average the difference is consistent with zero.

In order to investigate whether the profiles of $z \sim 2$ quiescent galaxies deviate systematically from Sérsic profiles we plot the difference between the best-fit Sérsic profile and the residual-corrected flux profile in Figure 4.5, for all galaxies. Black lines indicate the deviation profiles of individual galaxies, and their mean is indicated by the red line. The light red area shows the $1 - \sigma$ spread around the mean. The mean profile is consistent with zero at all radii; the surface brightness profiles of quiescent galaxies at $z \sim 2$ seem to be well described by Sérsic profiles. On average the residual correction increases or decreases the total flux of each galaxy in our sample by only a few percent, with an upper limit of 7%. The mean contribution of the residual flux to the total flux for all galaxies in our sample is -0.7% . Thus, we do not find evidence that indicates that there is missing low surface brightness emission around compact quiescent $z \sim 2$ galaxies, and we therefore conclude that the small sizes found for these galaxies are correct.

4.5 THE MASS GROWTH OF $Z \sim 2$ QUIESCENT GALAXIES

In the previous Section we have shown that the surface brightness profiles of $z \sim 2$ quiescent galaxies closely follow Sérsic profiles, and that their sizes are not systematically underestimated due to a lack of sensitivity. We now compare their size distribution and surface

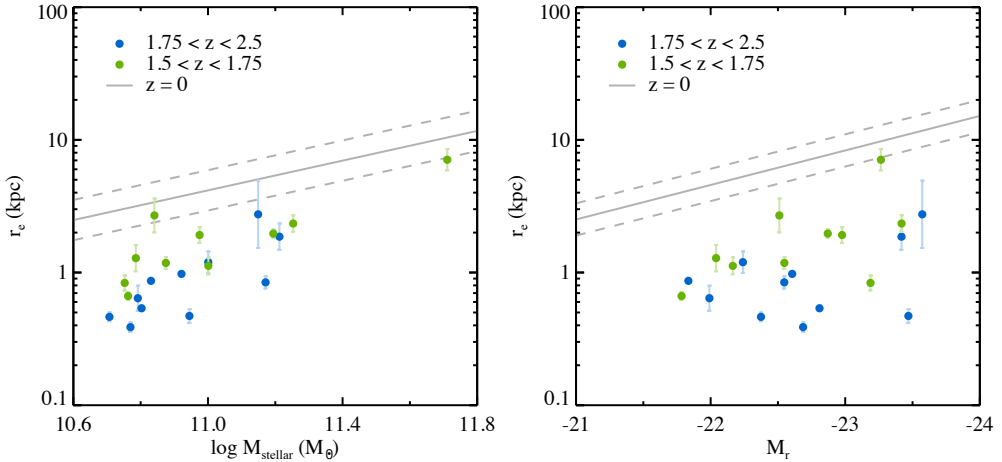


Figure 4.6: Relations between size and stellar mass (left panel) and size and rest-frame r -band absolute magnitude (right panel). Grey lines indicate the low-redshift mass-size and magnitude-size relations from Shen et al. (2003), green and blue points indicate the $z \sim 2$ sample (divided into low and high redshift bins, respectively). The $z \sim 2$ galaxies are, on average, almost an order of magnitude smaller than low-redshift galaxies of similar mass and luminosity. However, there is a significant range in sizes at both redshifts. The largest $z \sim 2$ galaxies lie very close to the $z = 0$ mass-size relation.

brightness profiles to those of low-redshift galaxies. In Figure 4.6 we show the mass-size and magnitude-size relations for the $z \sim 2$ galaxies and for low-redshift massive elliptical galaxies, taken from Shen et al. (2003). The $z \sim 2$ sample has been split into two redshift bins: $1.75 < z < 2.5$ and $1.5 < z < 1.75$ (shown in blue and green, respectively). The low-redshift sample is shown in grey. Galaxies at $z \sim 2$ are significantly smaller than those at $z = 0$. We fit a power law of the form $r_e \propto (1+z)^\alpha$ and find $\alpha = -0.94 \pm 0.16$, which is comparable to e.g., van der Wel et al. (2008) and van de Sande et al. (2011), but slightly steeper than Newman et al. (2010) and significantly shallower than Buitrago et al. (2008).

However, the $z \sim 2$ galaxies span a large range in size; some are supercompact, while others are as large as $z = 0$ galaxies. Following Shen et al. (2003), we quantify this range using $\sigma_{\log_{10} r_e}$, which is defined as the $1\text{-}\sigma$ spread in $\log_{10} r_e$ around the median mass-size relation, which we fix to the $z = 0$ slope. Note that we define the scatter in \log_{10} basis, not the natural logarithm as used by Shen et al. (2003). It is equal to 0.24 ± 0.06 for our entire sample, while Shen et al. (2003) find values around $\sigma_{\log_{10} r_e} = 0.16$ for early-type galaxies at $z = 0.1$ in the same mass range. The values for the two high-redshift subsamples are 0.21 ± 0.11 at $1.5 < z < 1.75$ and 0.19 ± 0.07 at $1.75 < z < 2.5$. These values are upper limits, since they include the errors on individual size measurements; however, if our error estimates are correct, their effect on the scatter is $\lesssim 0.01$ dex. The scatter we measure is comparable to that found in ?. These authors find $\sigma_{\log_{10} r_e} \approx 0.25$ for galaxies with $10^{10.7} M_\odot < M_{\text{stellar}} \lesssim 10^{11.7} M_\odot$ at $z \sim 2$. We note that our sample contains

several galaxies that are part of an overdensity at $z = 1.6$ (e.g., Gilli et al. 2003; Castellano et al. 2007; Kurk et al. 2009). In particular, the two largest galaxies in our sample are part of this overdensity. Excluding the $z = 1.6$ galaxies from our analysis does not significantly alter the spread in galaxy sizes in the $1.5 < z < 1.75$ redshift bin: $\sigma_{\log_{10} r_e} = 0.21 \pm 0.14$.

The size measurements used in Shen et al. (2003) have been shown to suffer from systematic errors due to background oversubtraction (Guo et al., 2009). As a result of this, the mass-size relation measured by Shen et al. (2003) is significantly shallower than that found by, e.g., Guo et al. (2009). We therefore repeat our determination of the scatter around the $z \sim 2$ mass-size relation using the Guo et al. (2009) measurements. This results in a decrease in the scatter by only ~ 0.03 dex, and does not affect our conclusions.

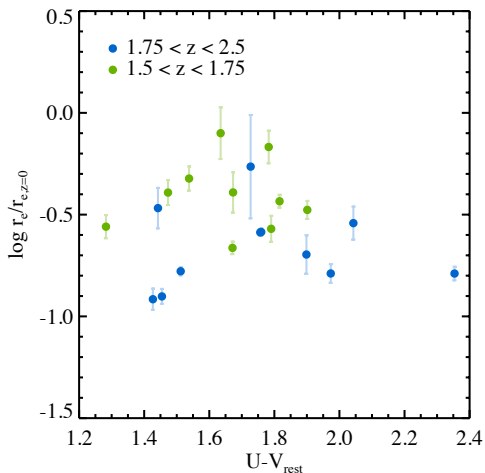


Figure 4.7: Offset from the $z = 0$ mass-size relation as a function of rest-frame $U - V$ color for galaxies at $1.5 < z < 1.75$ (green points) and $1.75 < z < 2.5$ (blue points). The offset is calculated by dividing the effective radius of each galaxy by the median effective radius of $z = 0$ quiescent galaxies with the same mass, using the $z = 0$ mass-size relation from Shen et al. (2003). The galaxies are split into two redshift bins. Assuming that rest-frame $U - V$ color is a good proxy for the mean stellar age of galaxies, we find no evidence for a correlation between galaxy compactness and galaxy age for $z \sim 2$ quiescent galaxies.

We note that, even within the limited redshift range under consideration, differences in redshift play a role: the galaxies in the $1.75 < z < 2.5$ subsample are clearly smaller than the $1.5 < z < 1.75$ galaxies. This may explain some of the disagreement between studies of high-redshift quiescent galaxies. In particular, the large effective radii found by Mancini et al. (2010) for some high-redshift quiescent galaxies could be due to the fact that they select galaxies with $1.4 < z < 1.75$. In this context, part of the size evolution between $z \sim 2$ and $z = 0$ could be due to the appearance of young, relatively large quiescent galaxies after $z \sim 2$ (e.g., van Dokkum et al. 2008; Franx et al. 2008; Saracco et al. 2009; van der Wel et al. 2009; Cassata et al. 2011). We note that Saracco et al. (2009) find evidence for a correlation of galaxy compactness with stellar age, such that the most compact high-redshift quiescent galaxies contain older stellar populations than quiescent galaxies that lie close to the $z = 0$ mass-size relation. We investigate this correlation in Figure 4.7, using rest-frame $U - V$ color as a proxy for galaxy age. We define galaxy compactness as the offset between the $z \sim 2$ galaxy sizes and

the $z = 0$ mass-size relation of Shen et al. (2003): $r_e/r_{e,z=0} = r_e/(2.88 \times 10^{-6} \times M^{0.56})$. We find no evidence for a correlation between galaxy compactness and galaxy age in our data.

In Figure 4.8 we compare the stellar mass surface density profiles of the $z \sim 2$ galaxies to those of low redshift galaxies. Based on their masses and number densities, we expect $z \sim 2$ quiescent galaxies to evolve into the most massive low-redshift galaxies (e.g., van Dokkum et al. 2010). As a comparison sample we therefore use surface brightness profiles of elliptical galaxies with equal or higher mass in the Virgo cluster from Kormendy et al. (2009). These authors used a combination of space-based and ground-based observations to obtain surface brightness profiles with very high resolution and dynamic range, covering almost three orders of magnitude in radius. The surface brightness profiles have been converted to stellar mass surface density profiles using the total stellar mass-to-light ratios. We have ignored radial color gradients, which are known to exist at low and high redshift (e.g., van Dokkum et al. (2010); Szomoru et al. (2011); Guo et al. (2011)). These profiles are shown in grey, with the profiles of the $z \sim 2$ galaxies overplotted in blue and green.

What is most apparent in Figure 4.8 is that the central ($r < 1 - 3$ kpc) surface densities of the $z \sim 2$ galaxies are very similar to those of the $z = 0$ galaxies, while at larger physical radii (in kpc) the high-redshift galaxies have lower surface densities than the low-redshift galaxies. The profiles are in close agreement with previous studies (e.g., Bezanson et al. 2009; Carrasco et al. 2010). We compare the change in radial mass density profiles to the mass evolution of quiescent galaxies described in Brammer et al. (2011). These authors show that galaxies with a number density of 10^{-4} Mpc^{-3} have grown in mass by a factor ~ 2 since $z = 2$. As mentioned above, the mass contained within 3 kpc changes very little from $z \sim 2$ to $z = 0$; we find an increase on the order of 10%. However, the mass contained outside 3 kpc is approximately ten times higher for the $z = 0$ galaxies than for the $z \sim 2$ galaxies, and is equal to 58% of their total mass. Thus, slightly more than half of the total mass of the $z = 0$ ellipticals is located at $r > 3$ kpc, whereas the $z \sim 2$ galaxies contain nearly no mass at these radii. This is consistent with the Brammer et al. (2011) result, and suggests that compact $z \sim 2$ quiescent galaxies may survive intact as the cores of present-day massive ellipticals, with the bulk of

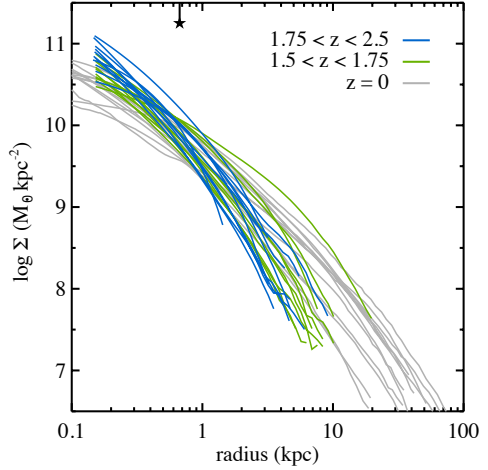


Figure 4.8: Comparison of stellar mass surface density profiles of $z \sim 2$ galaxies (blue and green curves) to elliptical galaxies in the Virgo cluster (Kormendy et al. 2009; grey curves). The Virgo galaxies are selected to have masses equal to or higher than those of the high-redshift galaxies. Radial color gradients are ignored when calculating the mass density profiles. The star, top left, indicates the PSF HWHM at $z = 2$. The central densities of the $z \sim 2$ galaxies are very similar to those of the $z = 0$ galaxies. At larger radii, however, significant evolution must occur if the $z \sim 2$ galaxies are to evolve into massive low-redshift elliptical galaxies.

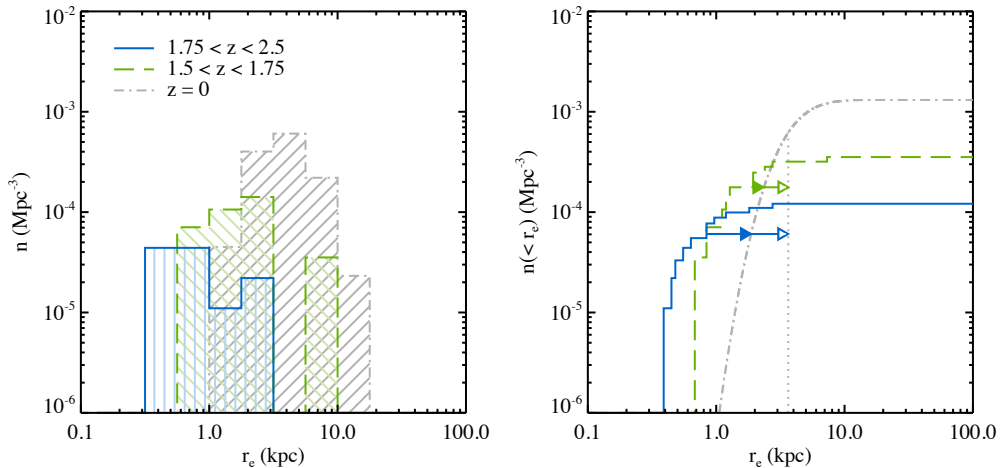


Figure 4.9: Comoving number density (left panel) and cumulative comoving number density (right panel) as a function of effective radius r_e , for galaxies at $1.75 < z < 2.5$, $1.5 < z < 1.75$, and $z = 0$ (solid blue, dashed green, and dot-dashed grey lines, respectively). The $z = 0$ number densities are obtained by combining the stellar mass function of Bell et al. (2003) with the mass-size relation of Shen et al. (2003). The $z \sim 2$ number densities have been scaled such that the total number density corresponds to the results of Brammer et al. (2011). Both the median effective radius and the total number density of quiescent galaxies show a strong increase from $z \sim 2$ to $z = 0$. The solid arrows in the right-hand panel indicate the minimum size growth required for high-redshift galaxies to grow into the smallest galaxies at $z = 0$. The open arrows indicate the size growth required for high-redshift galaxies to grow to the same median size as galaxies at $z = 0$. The minimum size growth required for $z \sim 2$ quiescent galaxies is approximately a factor 2 smaller than the median size growth between $z \sim 2$ and $z = 0$.

mass accretion since $z \sim 2$ occurring at large radii. This is consistent with an inside-out scenario of galaxy growth, as described in e.g., van Dokkum et al. (2010). We note that this discussion ignores transformations of star forming galaxies to the quiescent population.

Finally, we compare the comoving number densities and comoving cumulative number densities of our $z \sim 2$ sample to the number densities of $z = 0$ galaxies in Figure 4.9. To obtain the $z = 0$ number densities we combine the $z = 0$ mass function for early-type galaxies from Bell et al. (2003) with the mass-size relation of Shen et al. (2003): we use the relations appropriate for early-type galaxies and evaluate over the mass range $5 \times 10^{10} M_\odot < M_{\text{stellar}} < 5 \times 10^{11} M_\odot$. Given our small field size we cannot determine number densities accurately. We therefore adopt the number densities measured by Brammer et al. (2011). These authors used data covering a much larger field of view (approximately 25 times larger than the CANDELS GOODS-South field), and as such their results are less sensitive to cosmic variance. We scale our (cumulative) number density distributions such that the total number density corresponds to the Brammer et al. (2011) results. We note that our measured number densities are approximately a factor 2 smaller than those in Brammer et al. (2011), consistent with expectations from field-to-field varia-

tions (Somerville et al., 2004). We first consider the comoving number density distributions, plotted in the left panel of Figure 4.9. As expected, the median radius and the total number density increase with time, as existing galaxies grow in size and new quiescent galaxies appear. $r_{e,median} = 0.84 \pm 0.20$ kpc, 1.92 ± 0.45 kpc, and 3.82 ± 0.03 kpc at $1.75 < z < 2.5$, $1.5 < z < 1.75$ and $z = 0$, respectively.

We can place constraints on the minimum size growth of $z \sim 2$ galaxies by considering comoving cumulative number densities, shown in the right-hand panel of Figure 4.9. We assume that the population of $z \sim 2$ quiescent galaxies grows just enough to fall within the $z = 0$ size distribution, but doesn't necessarily grow to the same median size as $z = 0$. This results in a shift of the $z \sim 2$ cumulative number density distribution, indicated by the filled arrows in Figure 4.9. This shift is approximately a factor ~ 2 smaller than the size growth required for the $z \sim 2$ quiescent galaxy population to match the median size at $z = 0$ (indicated by the open arrows). Thus, in this minimal-growth scenario, half of the observed size evolution between $z \sim 2$ and $z = 0$ is due to the growth of existing galaxies, while the other half results from the appearance of new, larger quiescent galaxies at intermediate redshifts. These results are consistent with e.g., Cassata et al. (2011) and ?.

4.6 SUMMARY AND CONCLUSIONS

In this Paper we have demonstrated that the small measured sizes of $z \sim 2$ massive quiescent galaxies are not caused by a lack of sensitivity to low surface brightness flux. Using deep data and a method which is sensitive to excess emission at large radii, we have shown that the surface brightness profiles of these galaxies are well described by Sérsic profiles. The median Sérsic index is $n_{median} = 3.7$, similar to low-redshift quiescent galaxies.

The sizes of $z \sim 2$ quiescent galaxies span a large range; although the median effective radius is small ($r_{e,median} = 1.1$ kpc), values up to ~ 7 kpc are observed. The scatter in $\log r_e$ is 0.24 at $z \sim 2$, approximately 1.5 times as large as at $z = 0$. This indicates that the "dead" population of galaxies is very diverse at $z \sim 2$. We note that the size evolution between $z = 1.5$ and $z = 2.5$ is significant, which suggests that the cause of discrepancies in the results of different studies of the measured sizes of quiescent galaxies around $z = 2$ could be due to small differences in the redshift ranges considered.

Additionally, we have compared the stellar mass surface density profiles of $z \sim 2$ galaxies to those of massive early-type galaxies in the Virgo cluster. Although the densities within ~ 1 kpc are comparable, at larger radii the $z \sim 2$ galaxies show a clear deficit of mass. This puts strong constraints on models of galaxy formation and evolution. Firstly, most of the size buildup of $z \sim 2$ quiescent galaxies must occur at large radii (> 1 kpc). Secondly, a significant contribution from major gas-rich mergers since $z \sim 2$ seems to be ruled out, as this would disturb the inner density profiles of these galaxies. Minor, dry merging and slow accretion of matter seems to be the most viable method of evolving these galaxies into their $z = 0$ descendants.

Finally, we have investigated the evolution in the size distribution of massive quies-

cent galaxies. We conclude that the median size of massive quiescent galaxies changes by a factor ~ 4 between $z \sim 2$ and $z = 0$, and is accompanied by an increase in number density of a factor ~ 7 . However, it is important to note that the size growth of individual galaxies is likely to be significantly smaller. The minimum required size growth for the $z \sim 2$ quiescent galaxy population is approximately a factor ~ 2 smaller than the median overall size growth. In this scenario the stronger overall size growth may be caused by the appearance of new, larger quiescent galaxies at intermediate redshifts.

One of the main observational uncertainties pertaining to the size evolution of massive quiescent galaxies now appears to be resolved; robust sizes, measured at high resolution and using very deep rest-frame optical data, indicate that galaxies at $z \sim 2$ were significantly smaller than equally massive galaxies at $z = 0$. However, the mechanisms driving this evolution and their precise effects on the structure of individual galaxies, as well as on the characteristics of the population as a whole, are still not entirely understood. Most studies seem to point towards gas-poor galaxy merging as the dominant growth process (e.g., Bezanson et al. 2009; Naab et al. 2009; Hopkins et al. 2010); however, it is unclear whether this can account for all the observed size growth. A complicating factor in such studies is that tracing the same group of galaxies across cosmic time is very difficult, since their masses, sizes and stellar population properties are not constant; selecting the same population of galaxies at different epochs is therefore not trivial. Studies at fixed (cumulative) number density may provide a solution to this problem, though only for relatively massive galaxies.

REFERENCES

- Bell, E. F., McIntosh, D. H., Katz, N., & Weinberg, M. D. 2003, *ApJS*, 149, 289
- Bezanson, R., van Dokkum, P. G., Tal, T., Marchesini, D., Kriek, M., Franx, M., & Coppi, P. 2009, *ApJ*, 697, 1290
- Bezanson, R., et al. 2011, *ApJ*, 737, L31
- Brammer, G. B., van Dokkum, P. G., & Coppi, P. 2008, *ApJ*, 686, 1503
- Brammer, G. B., Whitaker, K. E., van Dokkum, P. G., et al. 2011, *ApJ*, 739, 24
- Bruzual, G., & Charlot, S. 2003, *MNRAS*, 344, 1000
- Buitrago, F., Trujillo, I., Conselice, C. J., et al. 2008, *ApJ*, 687, L61
- Caon, N., Capaccioli, M., & D'Onofrio, M. 1993, *MNRAS*, 265, 1013
- Cappellari, M., et al. 2009, *ApJ*, 704, L34
- Carrasco, E. R., Conselice, C. J., & Trujillo, I. 2010, *MNRAS*, 405, 2253
- Cassata, P., et al. 2010, *ApJ*, 714, L79
- Cassata, P., Giavalisco, M., Guo, Y., et al. 2011, *ApJ*, 743, 96
- Castellano, M., Salimbeni, S., Trevese, D., et al. 2007, *ApJ*, 671, 1497
- Cenarro, A. J., & Trujillo, I. 2009, *ApJ*, 696, L43
- Conroy, C., Gunn, J. E., & White, M. 2009, *ApJ*, 699, 486
- Côté, P., Ferrarese, L., Jordán, A., et al. 2007, *ApJ*, 671, 1456, *ApJ*, 699, 486
- Daddi, E., et al. 2005, *ApJ*, 626, 680
- Damjanov, I., et al. 2009, *ApJ*, 695, 101
- Ferrarese, L., Côté, P., Jordán, A., et al. 2006, *ApJS*, 164, 334
- Förster Schreiber, N. M., Shapley, A. E., Erb, D. K., et al. 2011, *ApJ*, 731, 65
- Förster Schreiber, N. M., Shapley, A. E., Genzel, R., et al. 2011, *ApJ*, 739, 45
- Franx, M., et al. 2003, *ApJ*, 587, L79
- Franx, M., van Dokkum, P. G., Schreiber, N. M. F., et al. 2008, *ApJ*, 688, 770
- Gilli, R., Cimatti, A., Daddi, E., et al. 2003, *ApJ*, 592, 721
- Graham, A. W., Erwin, P., Trujillo, I., & Asensio Ramos, A. 2003, *AJ*, 125, 2951
- Grogin, N. A., Kocevski, D. D., Faber, S. M., et al. 2011, *ApJS*, 197, 35
- Guo, Y., McIntosh, D. H., Mo, H. J., et al. 2009, *MNRAS*, 398, 1129
- Guo, Y., Giavalisco, M., Cassata, P., et al. 2011, *ApJ*, 735, 18
- Hopkins, P. F., Bundy, K., Murray, N., Quataert, E., Lauer, T. R., & Ma, C.-P. 2009, *MNRAS*, 398, 898
- Hopkins, P. F., Croton, D., Bundy, K., et al. 2010, *ApJ*, 724, 915
- Koekemoer, A. M., Faber, S. M., Ferguson, H. C., et al. 2011, *ApJS*, 197, 36
- Kormendy, J., Fisher, D. B., Cornell, M. E., & Bender, R. 2009, *ApJS*, 182, 216
- Kriek, M., et al. 2006, *ApJ*, 649, L71
- Kriek, M., van Dokkum, P. G., Labbé, I., et al. 2009, *ApJ*, 700, 221
- Kroupa, P. 2001, *MNRAS*, 322, 231
- Kurk, J., Cimatti, A., Zamorani, G., et al. 2009, *A&A*, 504, 331
- Mancini, C., et al. 2010, *MNRAS*, 401, 933
- Martinez-Manso, J., Guzman, R., Barro, G., et al. 2011, *ApJ*, 738, L22

Muzzin, A., van Dokkum, P., Franx, M., et al. 2009, *ApJ*, 706, L188
 Naab, T., Johansson, P. H., & Ostriker, J. P. 2009, *ApJ*, 699, L178
 Newman, A. B., Ellis, R. S., Treu, T., & Bundy, K. 2010, *ApJ*, 717, L103
 Newman, A. B., Ellis, R. S., Bundy, K., & Treu, T. 2012, *ApJ*, 746, 162
 Onodera, M., et al. 2010, *ApJ*, 715, L6
 Oser, L., Naab, T., Ostriker, J. P., & Johansson, P. H. 2012, *ApJ*, 744, 63
 Patel, S. G., Holden, B. P., Kelson, D. D., et al. 2011, arXiv:1107.3147
 Peng, C. Y., Ho, L. C., Impey, C. D., & Rix, H.-W. 2002, *AJ*, 124, 266
 Saracco, P., Longhetti, M., & Andreon, S. 2009, *MNRAS*, 392, 718
 Sérsic, J. L. 1968, *Atlas de galaxias australes* (Cordoba, Argentina: Observatorio Astronómico, 1968)
 Shen, S., Mo, H. J., White, S. D. M., et al. 2003, *MNRAS*, 343, 978
 Somerville, R. S., Lee, K., Ferguson, H. C., et al. 2004, *ApJ*, 600, L171
 Szomoru, D., et al. 2010, *ApJ*, 714, L244
 Szomoru, D., Franx, M., Bouwens, R. J., et al. 2011, *ApJ*, 735, L22
 Toft, S., et al. 2007, *ApJ*, 671, 285
 Taylor, E. N., Franx, M., Glazebrook, K., et al. 2010, *ApJ*, 720, 723
 Taylor, E. N., Franx, M., Brinchmann, J., van der Wel, A., & van Dokkum, P. G. 2010, *ApJ*, 722, 1
 Trujillo, I., Erwin, P., Asensio Ramos, A., & Graham, A. W. 2004, *AJ*, 127, 1917
 Trujillo, I., et al. 2006, *MNRAS*, 373, L36
 Trujillo, I., Cenarro, A. J., de Lorenzo-Cáceres, A., et al. 2009, *ApJ*, 692, L118
 van der Wel, A., Holden, B. P., Zirm, A. W., Franx, M., Rettura, A., Illingworth, G. D., & Ford, H. C. 2008, *ApJ*, 688, 48
 van der Wel, A., Bell, E. F., van den Bosch, F. C., Gallazzi, A., & Rix, H.-W. 2009, *ApJ*, 698, 1232
 van de Sande, J., et al. 2011, *ApJ*, 736, L9
 van Dokkum, P. G., et al. 2008, *ApJ*, 677, L5
 van Dokkum, P. G., Kriek, M., & Franx, M. 2009, *Nature*, 460, 717
 van Dokkum, P. G., et al. 2010, *ApJ*, 709, 1018
 Williams, R. J., Quadri, R. F., Franx, M., van Dokkum, P., & Labbé, I. 2009, *ApJ*, 691, 1879
 Wuyts, S., Labbé, I., Schreiber, N. M. F., Franx, M., Rudnick, G., Brammer, G. B., & van Dokkum, P. G. 2008, *ApJ*, 682, 985
 Wuyts, S., Franx, M., Cox, T. J., et al. 2009, *ApJ*, 700, 799
 Wuyts, S., Cox, T. J., Hayward, C. C., et al. 2010, *ApJ*, 722, 1666

THE STELLAR MASS STRUCTURE OF MASSIVE GALAXIES FROM $Z = 0$ TO $Z = 2.5$; SURFACE DENSITY PROFILES AND HALF-MASS RADII

We present stellar mass surface density profiles of a mass-selected sample of 177 galaxies at $0.5 < z < 2.5$, obtained using very deep HST optical and near-infrared data over the GOODS-South field, including recent CANDELS data. Accurate stellar mass surface density profiles have been measured for the first time for a complete sample of high-redshift galaxies more massive than $10^{10.7} M_{\odot}$. The key advantage of this study compared to previous work is that the surface brightness profiles are deconvolved for PSF smoothing, allowing accurate measurements of the structure of the galaxies. The surface brightness profiles account for contributions from complex galaxy structures such as rings and faint outer disks. Mass profiles are derived using radial rest-frame $u-g$ color profiles and a well-established empirical relation between these colors and the stellar mass-to-light ratio. We derive stellar half-mass radii from the mass profiles, and find that these are on average $\sim 25\%$ smaller than rest-frame g band half-light radii. This average size difference of 25% is the same at all redshifts, and does not correlate with stellar mass, specific star formation rate, effective surface density, Sérsic index, or galaxy size. Although on average the difference between half-mass size and half-light size is modest, for approximately 10% of massive galaxies this difference is more than a factor two. These extreme galaxies are mostly extended, disk-like systems with large central bulges. These results are robust, but could be impacted if the central dust extinction becomes high. ALMA observations can be used to explore this possibility. These results provide added support for galaxy growth scenarios wherein massive galaxies at these epochs grow by accretion onto their outer regions.

Daniel Szomoru, Marijn Franx, Pieter G. van Dokkum, Garth D. Illingworth, Michele Trenti,
Ivo Labbé, Pascal Oesch
The Astrophysical Journal, **763**, 73-83, 2013

5.1 INTRODUCTION

Over the past decades quantitative studies of high-redshift galaxy structure have advanced tremendously. Sensitive, high resolution instruments such as the Hubble Space Telescope's (*HST*) Advanced Camera for Surveys (ACS) and the Wide Field Camera 3 (WFC3) have made it possible to measure the structure of faint high-redshift galaxies at sub-kpc scales. Furthermore, the availability of easy-to-use photometric redshift and stellar population fitting packages has made it possible to straightforwardly measure a wide variety of parameters for ever-increasing numbers of galaxies.

Since a small amount of recent star formation can have a disproportionately large contribution to a galaxy's light compared to its mass, galaxies are usually observed at the reddest wavelengths, where emission from young stars is weakest. At low redshift, this can be done quite effectively, since rest-frame near-infrared (NIR) data is available at high enough resolution. At higher redshifts, however, it is impossible to observe at such long wavelengths with sufficiently high angular resolution. Until recently, the Hubble Space Telescope (*HST*) Advanced Camera for Surveys (ACS) was the only wide-field instrument capable of measuring the structure of high-redshift galaxies in any detail. At $z = 2$, the reddest filter available on ACS, Z_{850} , corresponds to rest-frame near-ultraviolet (NUV) wavelengths. Use of such short-wavelength data has been shown to result in drastically different conclusions about galaxy structure and morphology, compared to rest-frame optical data (e.g., Labbé et al. 2003; Toft et al. 2005; Cameron et al. 2011).

With the introduction of the *HST* Wide Field Camera 3 (WFC3) it has become possible to measure rest-frame optical light of $z \sim 2$ galaxies at a resolution approaching that of the ACS. The redder light detected by this instrument provides a much better proxy for stellar mass. However, color gradients are known to exist to some extent in all types of galaxies at redshifts up to at least $z \sim 3$, such that most galaxies contain a relatively red core and blue outer regions (e.g., van Dokkum et al. 2010; Szomoru et al. 2011; Guo et al. 2011). These color variations are caused by a combination of varying dust content, metallicity and stellar age, and imply that the stellar mass-to-light ratio (M_*/L) of a given galaxy varies with position within that galaxy. Thus, even though rest-frame optical light is a better tracer of stellar mass than rest-frame NUV light, neither accounts for the complexity of stellar population variations within galaxies.

By fitting stellar population models to resolved galaxy photometry, it is in principle possible to infer spatial variations in stellar mass, age, metallicity, dust content, and other parameters. This approach is currently somewhat limited by the lack of high-resolution data at infrared wavelengths, but can nonetheless be used to measure several basic stellar population properties. An example of this technique is presented in Wuyts et al. (2012), who have performed stellar population modeling on resolved *HST* data, using integrated IR observations as constraints on the overall properties of their galaxies. In this approach the integrated photometry serves as an important tool to constrain the overall spectral energy distribution (SED) of a galaxy, while the *HST* data provide information regarding the spatial variation of the stellar populations within these constraints.

In this Paper we explore an alternative method to recover M_*/L variations, using a simple empirical relation between rest-frame $u - g$ color and M_*/L . Using this method we construct stellar mass surface density profiles corrected for the effects of the PSF, for a mass-selected sample of galaxies between $z = 0$ and $z = 2.5$. We compare the resulting half-mass radii to half-light radii based on rest-frame optical imaging. All sizes presented in this Paper are circularized sizes: $r_e = r_{e,a} \sqrt{b/a}$. Throughout the Paper we assume a Λ CDM cosmology with $\Omega_m = 0.3$, $\Omega_\Lambda = 0.7$, and $H_0 = 70 \text{ km s}^{-1} \text{ Mpc}^{-1}$.

5.2 DATA AND SAMPLE SELECTION

HST IMAGING

We make use of deep near-IR imaging of the GOODS-South field, obtained with *HST*/WFC3 as part of the Cosmic Assembly Near-infrared Deep Extragalactic Legacy Survey (CANDELS; Grogin et al. 2011, Koekemoer et al. 2011). When completed, this survey will cover $\sim 700 \text{ arcmin}^2$ to 2 orbit depth in I_{814} , J_{125} and H_{160} (COSMOS, EGS and UDS fields), as well as $\sim 120 \text{ arcmin}^2$ to 12 orbit depth (GOODS-South and GOODS-North fields). We use the deepest currently available data, which consist of 9 orbits in J_{125} and H_{160} taken over GOODS-South. These NIR data are combined with deep *HST*/ACS data in the B_{435} , V_{606} , I_{775} and Z_{850} filters from the Great Observatories Origins Deep Survey (GOODS ACS v2.0; Giavalisco et al. 2004). The full width at half-maximum (FWHM) of the point-spread function (PSF) is $\approx 0.12 - 0.18 \text{ arcsec}$ for the WFC3 observations and $\approx 0.1 \text{ arcsec}$ for the ACS observations. The WFC3 and ACS images have been drizzled to pixel scales of 0.06 and 0.03 arcsec pixel $^{-1}$, respectively (see Koekemoer et al. 2011 for a detailed description of the CANDELS data reduction, and Giavalisco et al. 2004 for details of the ACS reduction).

We select galaxies using the K_s -selected FIREWORKS catalog (Wuyts et al., 2008). This catalog combines observations of the Chandra Deep Field South (CDFs) ranging from ground-based U -band data to *Spitzer* $24 \mu\text{m}$ data. It includes spectroscopic redshifts where available, as well as photometric redshifts derived using EAZY (Brammer et al., 2008). The photometric redshifts have a median $\Delta z / (1 + z) = -0.001$ with a normalized median absolute deviation of $\sigma_{NMAD} = 0.032$ (Wuyts et al., 2008). Stellar masses are estimated from SED fits to the full photometric data set (N.M. Förster Schreiber et al. 2012, in preparation), assuming a Kroupa IMF and the stellar population models of Bruzual & Charlot (2003). Star formation rates have been calculated using the UV and $24 \mu\text{m}$ fluxes (Wuyts et al., 2009).

We limit our analysis to galaxies with redshifts between $z = 0.5$ and $z = 2.5$; within this wavelength range we have the wavelength coverage needed to measure rest-frame u and g band photometry. We select galaxies with stellar masses above $10^{10.7} M_\odot$, which is the completeness limit in this redshift range (Wuyts et al., 2009). This redshift and mass cut results in a sample of 177 galaxies, of which 110 are at $0.5 < z < 1.5$ and 67 at $1.5 < z < 2.5$.

SDSS IMAGING

We compare our high-redshift galaxies to low-redshift galaxies observed as part of the Sloan Digital Sky Survey (SDSS; Abazajian et al. 2009). In order to obtain the deepest possible galaxy photometry we limit our analysis to data from SDSS stripe 82 (Annis et al., 2011). This region of the sky has been repeatedly imaged by SDSS, resulting in data which are ~ 2 magnitudes deeper compared to standard SDSS imaging. The PSF FWHM is ≈ 0.6 arcsec, and the images have a pixel scale of 0.396 arcsec pixel $^{-1}$.

We base our galaxy selection on the NYU Value-Added Galaxy Catalog (Blanton et al. 2005); stellar masses and star formation rates are taken from the MPA-JHU catalogs¹ (Brinchmann et al., 2004). We select galaxies with spectroscopically measured redshifts in a narrow redshift range $z = 0.06 \pm 0.005$ and with stellar masses above $10^{10.7} M_{\odot}$. This results in a sample of 220 galaxies.

5.3 ANALYSIS

REST-FRAME SURFACE BRIGHTNESS PROFILES

Most studies of galaxy structure at high redshift are based on parametrized two-dimensional surface brightness profile fits (e.g., using the GALFIT package of Peng et al. 2002). However, such methods do not account for deviations from the assumed model profile, which is generally an $r^{1/n}$ Sérsic profile. The technique used in this paper, which is described in more detail in Szomoru et al. (2010) and Szomoru et al. (2012), is different in the sense that these deviations are explicitly included in the measurement process. The intrinsic profile is derived by first fitting a Sérsic model profile convolved with the PSF to the observed flux, using a PSF constructed from unsaturated bright stars in the image. The residuals from this fit are then measured in radially concentric ellipses which follow the geometry of the best-fit Sérsic profile. By adding these residuals to the best-fit Sérsic profile, we effectively perform a first-order correction for deviations from the model profile and are able to account for complex substructures such as rings and faint outer disks. The resulting profiles closely follow the true intrinsic galaxy profiles, as shown in Szomoru et al. (2010) and Szomoru et al. (2012).

The surface brightness profiles of all galaxies in the high-redshift sample are measured in the B_{435} , V_{606} , I_{775} , Z_{850} , J_{125} and H_{160} filter; this ensures sufficient wavelength coverage to accurately measure rest-frame $u - g$ colors. The SDSS galaxy profiles are measured in the u , g , r and z bands. Errors in the flux profiles are calculated by adding the formal flux errors, sky variance, and the estimated error in the sky background determination. The radial extent of the profiles is mostly limited by uncertainties in the sky background estimation; typically, the profiles are accurate out to radii of approximately 10 kpc. At larger radii the

¹See http://www.mpa-garching.mpg.de/SDSS/DR7/mass_comp.html for a comparison between these masses and masses based on spectral indices

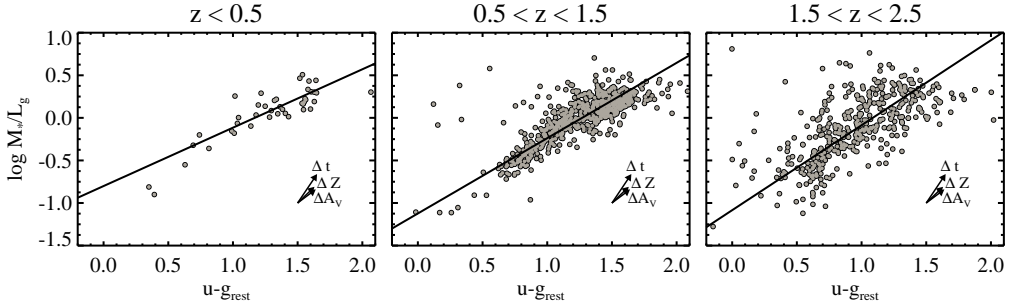


Figure 5.1: The relationship between rest-frame $u - g$ color and stellar mass-to-light ratio in three redshift bins. Grey circles denote integrated colors and mass-to-light ratios of individual galaxies in the Chandra Deep Field South, based on data from the FIREWORKS catalog (Wuyts et al., 2008). The best-fit linear relations are indicated by black lines. The slope of the relation is close to unity at high redshift, and flattens off at lower redshifts. The effects of age, dust extinction and metallicity on $u - g$ and M_*/L_g are indicated by the arrows labeled Δt , ΔA_V and ΔZ , respectively. The length of the vectors indicate the shift caused by an increase in stellar age from 1 Gyr to 5 Gyr, $1A_V$ of dust extinction, and an increase in metallicity from 0.02 to 2.5 times solar metallicity. Increases in stellar age, dust content, and metallicity all result in a shift roughly parallel to the best-fit relation, and are thus implicitly included in our empirical relation.

profiles are extrapolated using the Sérsic model profile. The extrapolated part of the profile typically contains $\sim 5 - 10\%$ of the total flux, depending on the galaxy profile shape.

Rest-frame u and g band profiles are derived by interpolating between the observed fluxes at each radius, using the SED-based interpolation package InterRest (Taylor et al., 2009). This package uses a set of template SEDs to interpolate between observed fluxes. The resulting rest-frame fluxes thus take into account the shape of a galaxy's SED and the filter throughputs of both the observed and rest-frame filters.

FROM COLORS TO MASS-TO-LIGHT RATIOS

Stellar mass-to-light ratios are estimated using an empirical relation between $u_{336} - g_{475}$ and M_*/L_g . The u and g filters straddle the Balmer and 4000\AA breaks; $u - g$ color is therefore sensitive to changes in stellar age, dust, and metallicity. Our empirical $u - g \rightarrow M_*/L_g$ relation is based on FIREWORKS photometry of galaxies in the CDFS, shown in Figure 5.1 (Wuyts et al., 2008). In this Figure we plot the integrated rest-frame $u - g$ colors and $\log M_*/L_g$ of galaxies in three redshift bins (grey circles). Rest-frame colors have been calculated using InterRest (Taylor et al., 2009), and the mass-to-light ratios are obtained from the SED fits described in Section 5.2. The black lines indicate the best-fit linear relation at each redshift. The slope of the relation is 1.0 at $z \sim 2$, 0.9 at $z \sim 1$, and 0.7 at $z \sim 0$. The uncertainty in $\log M_*/L_g$, given a value for $u - g$, is approximately 0.28 at $z \sim 2$, and 0.13 at lower redshifts.

The reason that these relations exist is due to the fact that stellar population variations (i.e., changes in stellar age, metallicity, and dust content) all produce roughly the same effects

in the $u - g$ --- M_*/L_g plane (Bell & de Jong (2001)). This is indicated by the arrows in each panel of Figure 5.1, which all point roughly in the same direction. Due to this degeneracy we can not distinguish between dust, age, and metallicity effects, but M_*/L_g can be determined quite robustly. It should also be noted that the axes in Figure 5.1 are not completely independent, since the rest-frame $u - g$ color enters into the stellar population fit from which M_*/L_g is determined.

There is significant scatter around the empirical relation used to convert $u - g$ color to M_*/L . Although age, metallicity, and dust variations produce similar shifts in the color- M/L plane, their effects are not exactly parallel to our empirical relation. This could lead to a systematic underestimate of the mass-to-light ratios in galaxy regions that are relatively metal-rich or old, and an overestimate in regions that are relatively metal-poor or young. Since the central regions of galaxies generally contain older stars, the inferred M_*/L gradients would then be too shallow. This effect is likely small, since the vectors shown in Figure 5.1 do not diverge very strongly, and the magnitude of the shift is small for moderate stellar population differences.

MASS PROFILE DERIVATION

The process of deriving stellar mass surface density profiles is illustrated for four galaxies in Figure 5.2. The galaxies are selected to show a range of color gradients. For each galaxy we show, from top to bottom, a rest-frame ubg color image, the observed-frame and rest-frame surface brightness profiles, the rest-frame $u - g$ color profile, and the resulting stellar mass surface density profile. The extent of the PSF half width at half-maximum (HWHM) is indicated by grey hatched areas.

The observed-frame residual-corrected surface brightness profiles, shown in grey-scale in the second row, are generally of high quality. The profiles deteriorate somewhat in the bluer bands for the highest-redshift galaxies. However, the profiles that are used for interpolating to rest-frame u and g wavelengths (i.e., measured in the bands directly red- and blueward of the rest-frame u and g wavelengths) have high signal-to-noise. The observed surface brightness profiles, and by extension the rest-frame $u - g$ profiles, are generally accurate out to ~ 10 kpc.

In the third row of Figure 5.2 we plot the observed $u - g$ color profiles as well as the average $u - g$ colors for the entire galaxy (in red and blue, respectively). The color gradients range from very steep ($\Delta(u - g)/\Delta \log r = -1$) to very shallow. At large radii ($r \gtrsim 10$ kpc) the color profiles become extremely uncertain. Due to the low surface brightness at these radii, the ratio of u band to g band flux is very sensitive to small errors in either flux profile. This can result in colors that become unrealistically blue or red. We therefore limit the color profiles to radii where the error in $u - g$ is smaller than 0.2 dex; the $u - g$ color at larger radii is fixed to the value at the threshold radius. This should not have a strong effect on the resulting stellar mass surface density profile, since the surface densities at these large radii are so low that they contribute very little to the total mass, even for high M_*/L_g .

The resulting mass profiles are shown in the fourth row, with the same color coding

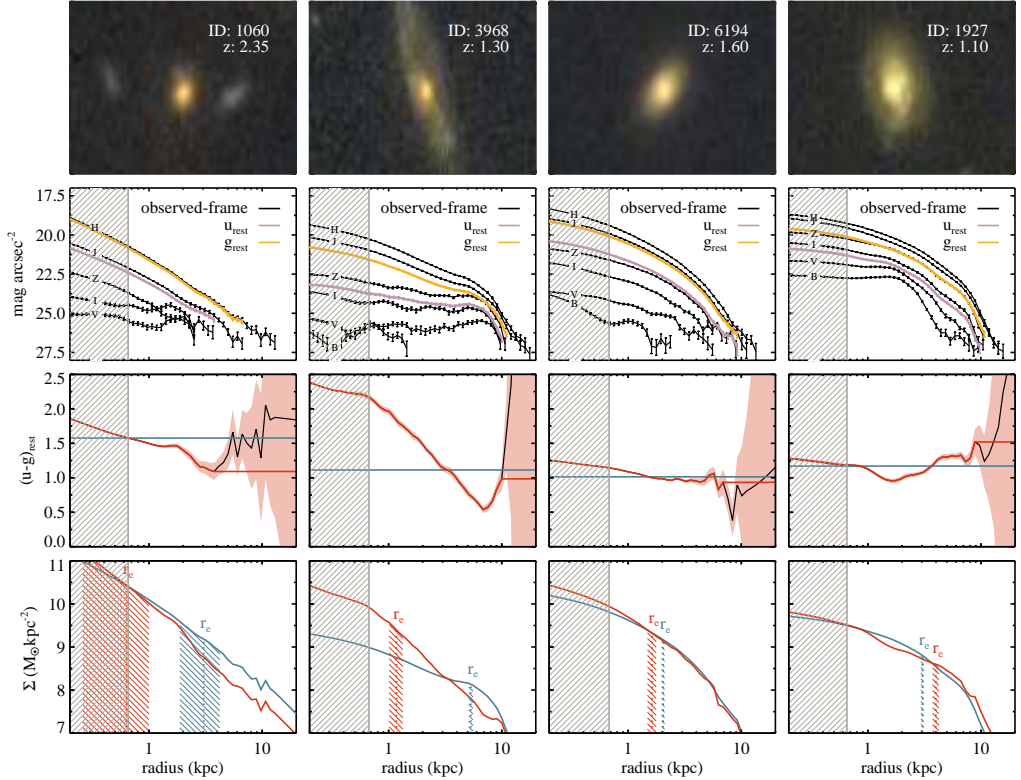


Figure 5.2: Illustration of the conversion of observed surface brightness profiles to stellar mass surface density profiles, for four sample galaxies at $0.5 < z < 2.5$. Top row: color images, composed of rest-frame u_{336} , B_{438} and g_{475} images. Second row: observed-frame residual-corrected surface brightness profiles (shown in greyscale), with rest-frame u and g band profiles overlaid in purple and yellow, respectively. Third row: measured $u - g$ color profiles and average $u - g$ colors (in red and blue, respectively). The grey hatched area indicates the PSF HWHM. Bottom row: resulting surface density profiles, with color coding corresponding to the color profiles in the third row. Effective radii are shown for both profiles; the red and blue hatched areas indicate the $1 - \sigma$ errors. Observed- and rest-frame photometry is generally of very high quality, and provides accurate $u - g$ color profiles out to ~ 10 kpc. The colors at the largest radii, where the flux profiles are not reliable, are extrapolated from the last well-measured color. Half-mass radii are in some cases more than 50% smaller than half-light radii.

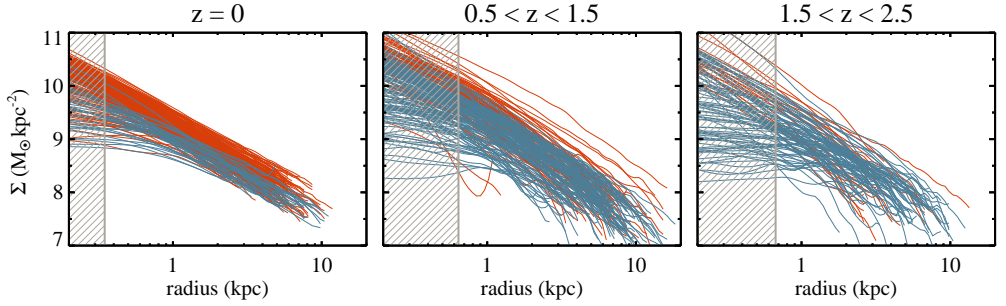


Figure 5.3: Stellar mass surface density profiles of galaxies with $M_* > 10^{10.7} M_\odot$ at $z = 0$, $z \sim 1$, and $z \sim 2$. Individual profiles are shown in blue and red for starforming and quiescent galaxies, respectively. The approximate PSF HWHM in each redshift bin is indicated by the hatched region. The profiles are plotted up to the radius where the errors become significant; they are accurate out to ~ 10 kpc, and down to surface densities of around $10^{7.5} M_\odot \text{ kpc}^{-2}$.

(blue assuming a constant M_*/L , red for radially varying M_*/L). Effective radii obtained by integrating the surface density profiles are shown for both profiles, with the hatched areas indicating the $1 - \sigma$ errors. The difference between assuming a radially constant mass-to-light ratio and actually accounting for M_*/L variations is clear. Radial M_*/L variations can lead to half-mass radii that are more than a factor 5 smaller than rest-frame g band half-light radii, with errors ranging from more than a factor 2 (first column) to smaller than 10% (second through fourth columns). These size differences will be discussed in more detail in the next Section. The surface density profiles of all galaxies in our sample are shown in Figure 5.3, and are also given in Table 5.2. Parameters derived from these profiles are given in Table 5.1.

5.4 MASS-WEIGHTED SIZES

STRUCTURAL PARAMETER DERIVATION

Having constructed stellar mass surface density profiles, we focus our attention on galaxy sizes. Half-mass radii are amongst the most basic galaxy characteristics and are especially important in the context of galaxy evolution, given their close connection to the build-up of stellar mass. Half-light radii, used in all studies of galaxy size evolution, can be strongly influenced by stellar population differences within a given galaxy. The surface density profiles described in the previous Section provide information on the true mass distribution of these galaxies.

Half-mass radii are calculated by integrating the surface density profiles out to a radius of ~ 100 kpc. This corresponds to ~ 12 arcsec for galaxies at $z \sim 1 - 2$, and ~ 90 arcsec for the $z = 0$ galaxies. The errors in the half-mass radii (and other parameters derived from the surface density profiles) are estimated in two ways. Firstly, we estimate the

Table 5.1: Galaxy parameters.

ID ^a	z	M_*^b (M_\odot)	$\log \text{SSFR}^b$ ($\log \text{yr}^{-1}$)	m_u^c (AB mag)	m_g^c (AB mag)	$\nabla u - g^d$	$\nabla \log M_*/L_g^d$	r_u (kpc)	r_g (kpc)	r_{mass} (kpc)	n_u	n_g	n_{mass}
981	1.13	10.97	-10.22	23.65	22.01	-0.41	-0.37	3.17	2.94	2.32	1.56	2.15	2.89
1030	1.10	11.18	-10.85	22.92	21.32	-0.03	-0.03	2.22	1.86	1.52	4.43	5.60	7.39
1043	1.14	11.02	-10.99	23.49	21.83	-0.79	-0.71	3.10	2.20	0.79	1.96	3.10	5.13
1060	2.35	11.17	-10.16	23.84	22.27	-0.59	-0.59	3.11	3.05	0.63	2.64	4.40	5.00
1088	1.72	10.75	-10.12	23.58	22.50	0.18	0.18	0.94	0.91	0.86	3.09	4.71	7.82
1148	1.10	10.99	-10.53	22.99	21.50	-0.19	-0.17	2.07	1.83	1.36	2.01	2.50	3.55
1175	1.09	10.91	-10.15	23.45	21.97	-0.29	-0.26	3.34	2.40	1.78	3.39	3.44	2.92
1190	1.10	11.10	-9.39	22.13	20.91	-0.22	-0.20	5.07	4.96	4.75	1.33	1.52	1.83
1242	1.10	11.31	-10.74	22.48	21.07	-0.15	-0.14	14.56	8.32	8.06	5.38	6.86	5.15
1246	1.10	10.95	-9.23	22.88	21.53	-0.24	-0.21	2.79	2.67	2.23	0.94	1.32	2.64
...

This is a sample of the full table, shown for illustrative purposes.

^aFIREWORKS ID (Wuyts et al., 2008) for $0.5 < z < 2.5$ sources, NVU-VAGC ID (Blanton et al., 2005) for $z < 0.5$ sources.

^bMasses and SSFRs are taken from the FIREWORKS catalog for $0.5 < z < 2.5$ sources, and from the MPA-JHU catalogs for $z < 0.5$ sources (see Section 5.2 for details).

^cTotal apparent magnitudes in rest-frame filters.

^dColor and M_*/L_g gradients are defined as $\Delta(u - g)/\Delta(\log r)$ and $\Delta(\log M_*/L_g)/\Delta(\log r)$, respectively. They are calculated using a linear fit to every profile between the PSF FWHM and the radius at which errors start to dominate (typically 8-10 kpc).

Table 5.2: Stellar mass surface density profiles.

ID ^a	redshift	r_{arcsec} (arcsec)	r_{kpc} (kpc)	μ_u (AB mag arcsec ⁻²)	μ_g (AB mag arcsec ⁻²)	$\log M_*/L_g$ ($\log M_\odot/L_\odot$)	$\log \Sigma$ ($\log M_\odot \text{ kpc}^{-2}$)
981	1.13	0.0180	0.148	21.470 ± 0.0056	19.442 ± 0.0008	0.671 ± 0.1301	10.552 ± 0.1301
981	1.13	0.0198	0.163	21.509 ± 0.0058	19.499 ± 0.0009	0.655 ± 0.1301	10.514 ± 0.1301
981	1.13	0.0216	0.177	21.547 ± 0.0063	19.552 ± 0.0009	0.642 ± 0.1301	10.479 ± 0.1301
981	1.13	0.0240	0.197	21.596 ± 0.0083	19.620 ± 0.0011	0.625 ± 0.1302	10.435 ± 0.1302
981	1.13	0.0264	0.217	21.642 ± 0.0087	19.683 ± 0.0015	0.610 ± 0.1302	10.394 ± 0.1302
981	1.13	0.0288	0.237	21.687 ± 0.0090	19.744 ± 0.0016	0.596 ± 0.1303	10.356 ± 0.1303
981	1.13	0.0318	0.261	21.740 ± 0.0099	19.815 ± 0.0018	0.580 ± 0.1303	10.312 ± 0.1303
981	1.13	0.0348	0.286	21.792 ± 0.0124	19.883 ± 0.0019	0.566 ± 0.1305	10.271 ± 0.1305
981	1.13	0.0384	0.315	21.851 ± 0.0131	19.960 ± 0.0020	0.550 ± 0.1305	10.224 ± 0.1305
981	1.13	0.0426	0.350	21.919 ± 0.0139	20.044 ± 0.0023	0.535 ± 0.1306	10.176 ± 0.1306
...

This is a sample of the full table, shown for illustrative purposes.

^aFIREWORKS ID (Wuyts et al., 2008) for $0.5 < z < 2.5$ sources, NYU-VAGC ID (Blanton et al., 2005) for $z < 0.5$ sources.

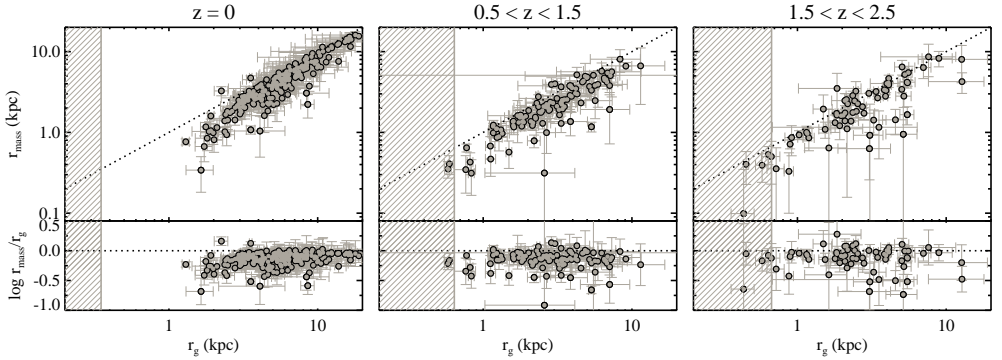


Figure 5.4: Half-mass radii versus rest-frame g band half-light radii, for galaxies with $M_* > 10^{10.7} M_\odot$. The approximate PSF HWHM in each redshift bin is indicated by the hatched region. At all redshifts the half-mass radii of galaxies are on average 25% smaller than their half-light radii. Values as low as $\log r_{mass}/r_g = -0.7$ are found.

uncertainty due to errors in the flux profile by varying the $u - g$ color profiles within their $1 - \sigma$ error ranges, deriving mass profiles based on these new color profiles, and calculating the resulting range of half-mass radii. Secondly, we estimate the effects of PSF variations on our size determinations. This is done by rerunning the entire procedure described in Section 5.3 using twelve different stellar PSFs. The median error in r_{mass} due to these sources is 18%.

In Figure 5.4 the half-mass radii are plotted against half-light radii measured from the rest-frame g band surface brightness profiles. The half-mass radii are generally smaller than the half-light radii: $\langle \log r_{mass}/r_g \rangle \approx -0.12 \pm 0.01$. Overall, the stellar mass distributions of massive galaxies are more concentrated than their rest-frame optical light distributions by about 25%. The overall trend is in agreement with previous studies, which have found that galaxies at these redshifts tend to show negative color gradients, such that their cores are relatively red (e.g., van Dokkum et al. 2010; Szomoru et al. 2011; Guo et al. 2011).

Table 5.3: Differences between mass-weighted and luminosity-weighted parameters.

	$\log r_{mass} - \log r_g$		$\log n_{mass} - \log n_g$	
	median	σ_{NMAD}	median	σ_{NMAD}
$z = 0$	-0.12 ± 0.01	0.08	0.06 ± 0.03	0.31
$0.5 < z < 1.5$	-0.14 ± 0.01	0.11	0.09 ± 0.02	0.20
$1.5 < z < 2.5$	-0.10 ± 0.02	0.13	0.02 ± 0.03	0.19
	$\log M_{mass} - \log M_g^a$		$(u - g)_{mass} - (u - g)_g^b$	
	median	σ_{NMAD}	median	σ_{NMAD}
$z = 0$	0.12 ± 0.01	0.14	0.059 ± 0.004	0.048
$0.5 < z < 1.5$	0.04 ± 0.01	0.06	0.044 ± 0.006	0.048
$1.5 < z < 2.5$	0.02 ± 0.01	0.07	0.043 ± 0.007	0.051

Note: the *mass* subscript indicates parameters derived using the true mass profiles (i.e., with radially varying M_*/L), while the *g* subscript indicates parameters derived using profiles that assume a constant M_*/L profile (i.e., equivalent to the rest-frame *g* band profiles).

^a $\log M_{mass}$ is the total stellar mass derived by summing the resolved mass density information. $\log M_g$ is the total stellar mass based on integrated photometry.

^b $(u - g)_{mass}$ is the mass-weighted color (see Equation 5.4), and $(u - g)_g$ is the luminosity-weighted color.

The median differences between mass-weighted and luminosity-weighted parameters are given in Table 5.3. Mass-weighted Sérsic indices (obtained by fits to the radial surface density profiles) are on average $\sim 5 - 20\%$ larger than luminosity-weighted Sérsic indices. It should be noted that Sérsic indices are much more difficult to accurately constrain than effective radii, due to their sensitivity to systematic uncertainties; errors on our mass-weighted Sérsic indices are approximately twice as large as errors on our mass-weighted effective radii.

We also give the difference between total masses calculated by integrating the stellar mass surface density profiles and total masses from integrated photometry. We find that, on average, masses from resolved photometry are higher than those based on integrated light: the median difference is $5 - 10\%$ at high redshift, and $\sim 30\%$ at $z = 0$. Our low-redshift result is in agreement with results presented by Zibetti et al. (2009), who derive resolved stellar mass maps of nine nearby galaxies with a range of morphologies. These authors find that mass estimates from integrated photometry may miss up to 40% of the total stellar mass compared to estimates obtained by summing resolved mass maps, due to dusty regions being underrepresented in the total flux of galaxies.

This has consequences for integrated galaxy colors, which are often used as a proxy for star formation activity. Dusty, red regions with low flux but high mass densities will be underrepresented in colors based on integrated galaxy photometry. We estimate this effect

using total rest-frame $u - g$ colors. Mass-weighted colors are calculated as follows:

$$(u - g)_{mass} = \frac{\int \frac{f_u(r)}{f_g(r)} \Sigma(r) dr}{\int \Sigma(r) dr}, \quad (5.1)$$

where $f_u(r)$, $f_g(r)$ and $\Sigma(r)$ are the radial u and g band flux density and radial stellar mass surface density profiles, respectively. On average, mass-weighted $u - g$ colors are redder than luminosity-weighted $u - g$ colors by 0.04 – 0.06 magnitudes, indicating that the SSFRs implied by luminosity-weighted $u - g$ colors are slightly overestimated compared to those implied by mass-weighted colors.

SOURCES OF UNCERTAINTY

The stellar mass surface density profiles are generally not very sensitive to the extrapolation of the color profiles towards larger radii, due to the fact that the total flux at $r > 10$ kpc is very low. Furthermore, this source of uncertainty is explicitly included in our errors, since they are estimated by varying the $u - g$ color that is used for the extrapolation. Uncertainty in the shape of the color profile within the PSF HWHM is more difficult to quantify, and may be especially important for the smallest galaxies ($r_g < 1$ kpc). In order to estimate the stability of our derived sizes we have explored several alternative approaches: one in which the inner $u - g$ color is kept fixed to the integrated value within 1 kpc; and one in which the best-fit linear color gradient is extrapolated from the PSF HWHM inward. Neither approach alters our results.

A possible concern is regions with very high dust content, which could potentially obscure stellar light to such a degree that our $u - g \rightarrow M_*/L$ conversion becomes ineffective, simply because all stellar light is extinguished. Very high central dust concentrations may result in an underestimate of the inner mass content of galaxies, and an overestimate of their half-mass radii. Such effects are a significant source of systematic uncertainty in our analysis, and can only be quantified by measuring the light reemitted by dust. This requires infrared imaging at *HST* resolution or better, which will become possible in the near future using ALMA.

The measured shape and radial extent of a galaxy's surface brightness profile are sensitive to the depth to which the galaxy is imaged. A lack of imaging depth can result in

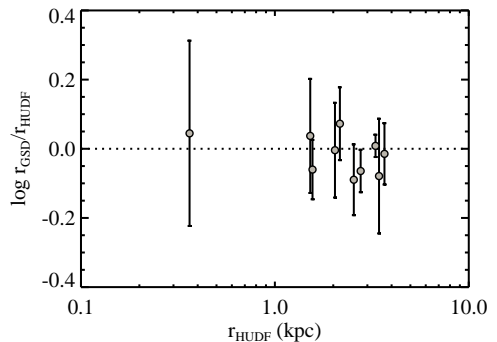


Figure 5.5: Comparison of half-mass radii derived using CANDELS GOODS-South data and HUDF data, for the galaxies with $0.5 < z < 2.5$ and $M_* > 10^{10.7}$ that are found in both datasets. The two datasets agree within the errors.

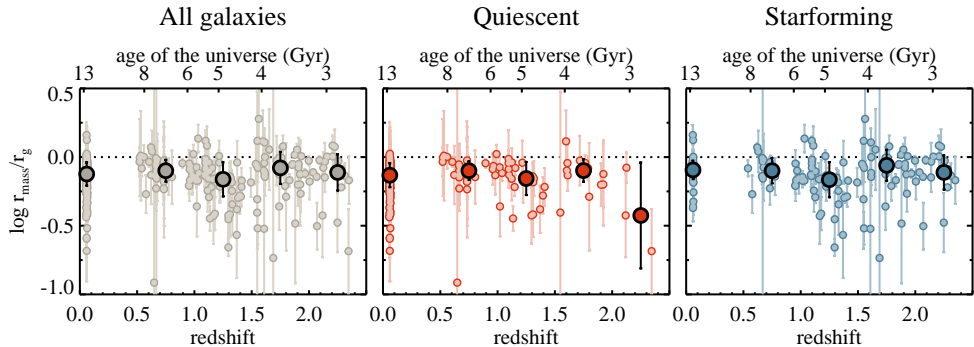


Figure 5.6: The ratio of half-mass size to half-light size, r_{mass}/r_g , as a function of redshift, for galaxies with $M_* > 10^{10.7}$. From left to right are plotted all galaxies, quiescent galaxies, and starforming galaxies. The large symbols indicate the running median, with the error bars indicating the $1 - \sigma$ scatter of the distribution. Our results indicate that, at fixed mass, galaxies have similar r_{mass}/r_g values at all redshifts between $z = 0$ and $z = 2.5$.

errors in sky background estimation, as well as a portion of the galaxy's emission being lost in the background noise. Generally, low-S/N data is likely to introduce systematic effects, such that measured sizes and Sérsic indices are smaller than the true values (e.g., Trujillo et al. 2006; Williams et al. 2010). As a consistency check we therefore compare our results to those based on ultra-deep optical and NIR data acquired over the HUDF (Beckwith et al. 2006; Bouwens et al. 2011). These data are ~ 2 magnitudes deeper in the NIR than the CANDELS data and should therefore be unaffected by these surface brightness effects. We find 11 galaxies with $M_* > 10^{10.7} M_\odot$ and $0.5 < z < 2.5$ which are imaged by both CANDELS and HUDF. The HUDF WFC3 data of one of these galaxies shows some artificial background features, which are the result of the background subtraction process; this galaxy is therefore excluded from the comparison. The HUDF imaging is processed in exactly the same way as described in Section 5.3 for the CANDELS imaging. The resulting half-mass radii are compared to the CANDELS half-mass radii in Figure 5.5. The correspondence is good; HUDF and CANDELS measurements of r_{mass} lie within 1σ of each other, and we find no systematic offset. Thus, based on this subsample of galaxies we conclude that the CANDELS data are sufficiently deep for our purposes.

EVOLUTION WITH REDSHIFT

Figure 5.4 indicates that mass distributions are on average more concentrated than light distributions at all redshifts. We now investigate the redshift evolution of this concentration difference in more detail. In Figure 5.6 we plot r_{mass}/r_g as a function of redshift for all galaxies in our sample, as well as for quiescent and starforming galaxies separately. Quiescent galaxies are defined to have $SSFR < 0.3/t_H$, where t_H is the Hubble time. Individual galaxies are indicated by small circles, and median values for each redshift bin are shown as large,

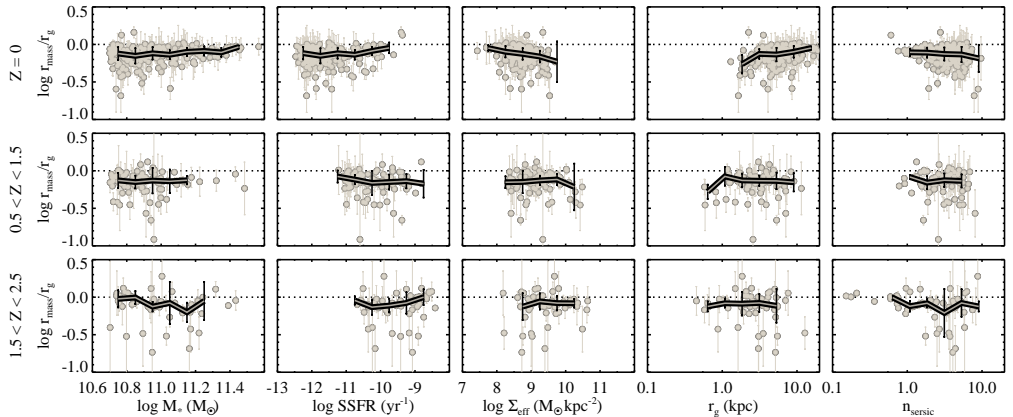


Figure 5.7: The correlations between r_{mass}/r_g and, from left to right: total stellar mass, specific star formation rate, and structural parameters measured in the rest-frame g band (effective surface density, effective radius, and Sérsic index). Individual galaxy measurements are indicated by circles, and running medians are indicated by the thick lines. The error bars on the running medians indicate the $1 - \sigma$ scatter. Each row corresponds to a redshift bin. r_{mass}/r_g correlates weakly, if at all, with starforming activity at both high and low redshift.

darker circles. The error bars on the median values indicate the scatter of the distribution.

Overall, the difference between mass-weighted and luminosity-weighted radius does not seem to evolve with redshift: $\log r_{mass}/r_g = -0.12 \pm 0.01$ at $z = 0$, -0.14 ± 0.01 at $z \sim 1$, and -0.10 ± 0.02 at $z \sim 2$ (see also Table 5.3). Similarly, the values for starforming galaxies are consistent with no evolution with redshift. For quiescent galaxies, there is a hint of decreasing values of $\log r_{mass}/r_g$ at higher redshifts, although the large scatter at $z \sim 2$ means that these results are also consistent with zero redshift evolution.

The lack of evolution with redshift agrees with the color gradients presented in Szomoru et al. (2011). This study showed that the radial color gradients in galaxies with $10^{10} < M_*/M_\odot < 10^{11}$ are nearly constant between $0 < z < 2.5$. This seems counterintuitive, since one would expect bulge growth in galaxies to result in steeper color gradients at lower redshift. However, it should be stressed that the comparison in Figure 5.6 is between galaxies of the same mass. It is therefore not a comparison between high-redshift galaxies and their descendants, but rather a comparison between high-redshift galaxies and their low-redshift analogs. Thus, $z \sim 2$ galaxies have similar color gradients as low redshift galaxies of the same mass. This holds for starforming and quiescent galaxies separately, and for the entire population as a whole.

DEPENDENCE ON GALAXY PARAMETERS

The transition of galaxies from the starforming to the passive population is coupled to changes in almost all aspects of their structure and morphology (e.g., Kauffmann et al. 2003; Toft et al. 2007; Franx et al. 2008; Bell 2008; van Dokkum et al. 2011; Szomoru

et al. 2011; Wuyts et al. 2011; Bell et al. 2012). The growth of a bulge, in particular, implies that color gradients should steepen as galaxies are quenched. We therefore expect some degree of correlation between r_{mass}/r_g and the galaxy parameters that correlate with star forming activity, such as SSFR, size, Sérsic index, and effective surface density. We investigate these correlations in Figure 5.7. Individual galaxies are indicated by small light-colored circles, and the running medians in each panel are indicated by darker lines.

Somewhat surprisingly, the median value of r_{mass}/r_g is close to constant as a function of galaxy parameters in all redshift bins. There is some evidence for a trend between r_{mass}/r_g and galaxy morphology, such that r_{mass}/r_g is smaller for galaxies with low SSFR, small sizes and high Sérsic indices. However, this trend is very weak. Overall, the correlation coefficients at $z \sim 1$ and $z \sim 2$ are very low and not significant ($r \sim 0.01$, $p \sim 0.4$). The exceptions to this are the correlations between $\log r_{mass}/r_g$ and \log SSFR and n_{seraic} , at $z \sim 2$; although these are also quite low, they are significant ($r \sim 0.35$, $p < 0.01$). Similarly, the correlation coefficients at $z = 0$ are low, but significant ($r \sim 0.2 - 0.3$, $p < 0.01$). We conclude that the difference between half-mass size and half-light size correlates very weakly with galaxy structure and star forming activity.

Although the average difference between half-mass and half-light radius is remarkably constant, for some galaxies the difference is up to a factor eight. These large differences warrant closer inspection. In Figure 5.8 we show images and profiles of a number of galaxies with $r_{mass}/r_g < 0.5$. Four representative galaxies have been selected from each redshift bin, and are plotted in order of decreasing SSFR. The flux profile errors of the galaxies shown are typical for the galaxies in this sample. Nearly all of these galaxies are dominated by large central bulges, but also contain extended, blue disks. These large galaxies have very well-measured surface brightness profiles; errors are low, and the profiles are measured accurately out to very large radii. We are therefore confident that the color gradients, although very steep, are real.

This group of galaxies demonstrates the importance of obtaining resolved stellar mass information. Measurements made at rest-frame optical wavelengths severely underestimate the relative importance of the central bulge component in these galaxies, due to the high luminosity of the blue disks surrounding them. As a result, for a sizeable fraction ($\sim 10\%$) of massive galaxies the structure as measured at rest-frame optical wavelengths severely misrepresents the mass distribution in these galaxies.

This population of large, bulge-dominated disk galaxies is very interesting. They have stellar masses up to $\sim 10^{11} M_\odot$ and are distributed across the entire range of measured SSFRs. Moving from high to low SSFR, we can see a progression from Sa or Sb-like systems to objects that look more like S0s and elliptical galaxies. This is most evident at low redshift, where galaxies have large angular sizes. The color difference between the central bulge and extended disk gradually decreases from high- to low-SSFR galaxies. In other words, it seems that we are observing these galaxies during the phase where a central bulge has recently formed and star formation is turning off. It is unclear why other galaxies with similar SSFRs do not contain such large bulges; this may depend on the dark matter halos in which they are located, or may perhaps be due to different quenching processes.

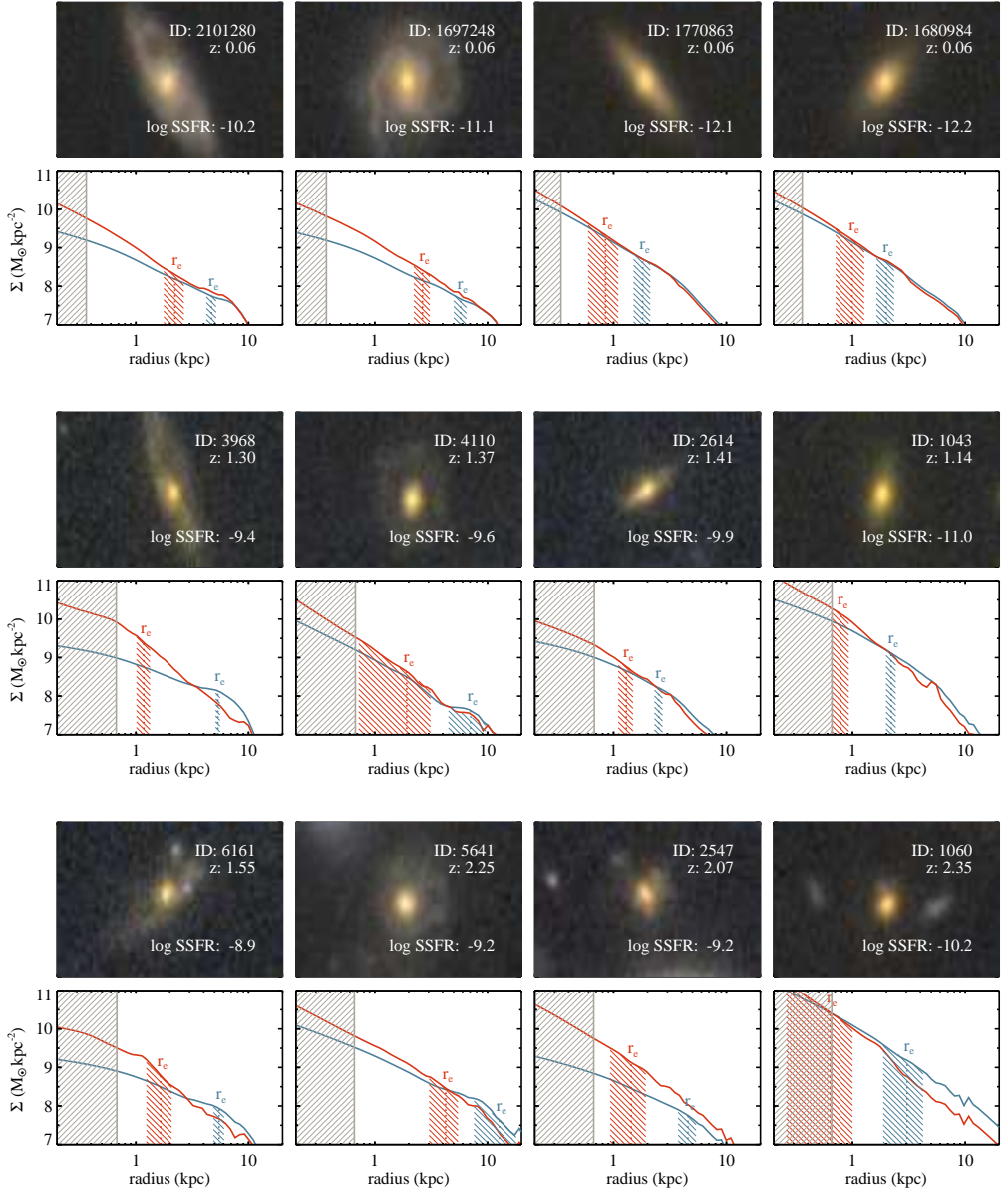


Figure 5.8: A representative selection of galaxies with $r_{mass}/r_g < 0.5$, ordered by SSFR. All galaxies are extended, disk-like galaxies with large central bulges. Measurements in the rest-frame g band result in severely overestimated sizes compared to the half-mass sizes. The color gradients are measured with high precision; the large differences between r_{mass} and r_g are therefore not the result of measurement errors.

5.5 SUMMARY AND CONCLUSIONS

We have presented the first consistently measured stellar mass surface density profiles for individual galaxies at redshifts between $z = 0$ and $z = 2.5$. These profiles have been derived using an empirical relation between rest-frame color and stellar mass-to-light ratio. This simple method does not yield the same detailed information regarding, e.g., stellar ages and dust content as resolved SED-fitting techniques. However, it is robust to variations in stellar population properties; changes in stellar age, metallicity, or dust content shift galaxies roughly along the empirical relation, and are thus implicitly included in our M_*/L determination.

The key advantage of this study compared to previous work at high redshift (e.g., Wuyts et al. 2012; Lanyon-Foster et al. 2012) is the fact that the profiles presented here are deconvolved for PSF smoothing. This is crucial for measurements of high-redshift galaxy structure, since these distant and often physically small galaxies have angular sizes that are in many cases comparable to the *HST* PSF size (e.g., Daddi et al. 2005; Trujillo et al. 2006; Toft et al. 2007; van Dokkum et al. 2008; Szomoru et al. 2010; Cassata et al. 2010; Szomoru et al. 2012). Since our surface density profiles are derived from deconvolved surface brightness profiles, they can be used to correctly measure structural parameters such as sizes and Sérsic indices.

The considerable depth of the data used in this study allows us to probe galaxy fluxes and colors out to large radii. The robustness of the resulting structural parameters has been tested using ultradeep data taken over the HUDF, which overlaps with the CANDELS GOODS-South field. A comparison of galaxy parameters derived using the two datasets confirms that our results are not systematically affected by surface brightness effects.

We have shown that the half-mass radii of galaxies between $z = 0$ and $z = 2.5$ are on average 25% smaller than their rest-frame optical half-light radii. There is significant scatter in this size difference, with some galaxies having half-mass radii that are almost an order of magnitude smaller than their half-light radii. We find that, on average, this size difference does not vary with redshift for galaxies at fixed mass. This holds for the population as a whole, as well as for the quiescent and starforming subpopulations separately. This is an interesting result, as it implies that $z \sim 2$ galaxies have similar color gradients as their low-redshift analogs, despite the fact that these low-redshift galaxies formed at a different epoch, and perhaps through very different formation mechanisms.

There does not seem to be a strong correlation between galaxy morphology or star forming activity and the difference between half-mass size and half-light size. However, we do find that the galaxies with the most extreme size differences are almost all extended disk galaxies with very prominent central bulges. These galaxies range from strongly starforming to almost completely quiescent, and may represent a short transitional phase during which the central bulge is prominent and the starforming disk is very young.

There is significant scatter around the empirical relation used to convert $u - g$ color to M_*/L , which could lead to a systematic underestimate of the mass-to-light ratios in galaxy regions that are relatively metal-rich or old. However, this effect is likely small for moderate stellar population variations. Similarly, very high central dust concentrations may result in

an underestimate of the inner mass content of galaxies, biasing our results towards larger half-mass radii. The high-resolution infrared data needed in order to quantify such dust effects will be available in the (near) future, with instruments such as ALMA.

Inside-out galaxy growth, as described by, e.g., van Dokkum et al. (2010), implies that the growth of the most massive galaxies since $z \sim 2$ is largely due to material being accreted onto the outer regions of these galaxies. The cores of massive galaxies likely formed in short, violent bursts at higher redshift, and should therefore have star formation histories and stellar populations that are quite different from those in the outer regions. The results presented in this Paper broadly agree with such a picture; the central regions of massive galaxies are redder, and therefore likely older, than the outer regions. Using the method presented in this Paper we cannot, however, disentangle dust, age and metallicity gradients; nor can we constrain the star formation histories within our galaxies. First steps towards a better understanding of stellar population variations within high-redshift galaxies have been made by several authors. Results based on photometry of early-type galaxies (e.g., Guo et al. 2011; Gargiulo et al. 2012) indicate that stellar age and metallicity are the dominant drivers of radial color gradients. Studies based on spectroscopic measurements of gravitationally lensed high-redshift galaxies (e.g., Cresci et al. 2010; Jones et al. 2010; Yuan et al. 2011; Queyrel et al. 2012; Jones et al. 2012) have shown that most of these galaxies have negative metallicity gradients. These results seem to be roughly consistent with each other, but are based on very differently selected, and rather small, galaxy samples. A broader, more in-depth analysis of radial stellar population variations, for a well-defined sample of starforming galaxies as well as quiescent galaxies, could provide valuable insights into the processes which have shaped the structure of galaxies today.

REFERENCES

- Abazajian, K. N., Adelman-McCarthy, J. K., Agüeros, M. A., et al. 2009, *ApJS*, 182, 543
- Annis, J., Soares-Santos, M., Strauss, M. A., et al. 2011, arXiv:1111.6619
- Beckwith, S. V. W., Stiavelli, M., Koekemoer, A. M., et al. 2006, *AJ*, 132, 1729
- Bell, E. F., & de Jong, R. S. 2001, *ApJ*, 550, 212
- Bell, E. F. 2008, *ApJ*, 682, 355
- Bell, E. F., van der Wel, A., Papovich, C., et al. 2012, *ApJ*, 753, 167
- Blanton, M. R., Schlegel, D. J., Strauss, M. A., et al. 2005, *AJ*, 129, 2562
- Bouwens, R. J., Illingworth, G. D., Oesch, P. A., et al. 2011, *ApJ*, 737, 90
- Brammer, G. B., van Dokkum, P. G., & Coppi, P. 2008, *ApJ*, 686, 1503
- Brinchmann, J., Charlot, S., White, S. D. M., et al. 2004, *MNRAS*, 351, 1151
- Bruzual, G., & Charlot, S. 2003, *MNRAS*, 344, 1000
- Cameron, E., Carollo, C. M., Oesch, P. A., et al. 2011, *ApJ*, 743, 146
- Cassata, P., Giavalisco, M., Guo, Y., et al. 2010, *ApJ*, 714, L79
- Cresci, G., Mannucci, F., Maiolino, R., et al. 2010, *Nature*, 467, 811
- Daddi, E., Renzini, A., Pirzkal, N., et al. 2005, *ApJ*, 626, 680
- Franx, M., van Dokkum, P. G., Schreiber, N. M. F., et al. 2008, *ApJ*, 688, 770
- Gargiulo, A., Saracco, P., Longhetti, M., La Barbera, F., & Tamburri, S. 2012, arXiv:1207.2295
- Giavalisco, M., Ferguson, H. C., Koekemoer, A. M., et al. 2004, *ApJ*, 600, L93
- Grogin, N. A., Kocevski, D. D., Faber, S. M., et al. 2011, *ApJS*, 197, 35
- Guo, Y., Giavalisco, M., Cassata, P., et al. 2011, *ApJ*, 735, 18
- Jones, T., Ellis, R., Jullo, E., & Richard, J. 2010, *ApJ*, 725, L176
- Jones, T., Ellis, R. S., Richard, J., & Jullo, E. 2012, arXiv:1207.4489
- Kauffmann, G., Heckman, T. M., White, S. D. M., et al. 2003, *MNRAS*, 341, 54
- Koekemoer, A. M., Faber, S. M., Ferguson, H. C., et al. 2011, *ApJS*, 197, 36
- Labbé, I., Rudnick, G., Franx, M., et al. 2003, *ApJ*, 591, L95
- Lanyon-Foster, M. M., Conselice, C. J., & Merrifield, M. R. 2012, *MNRAS*, 3340
- Peng, C. Y., Ho, L. C., Impey, C. D., & Rix, H.-W. 2002, *AJ*, 124, 266
- Queyrel, J., Contini, T., Kissler-Patig, M., et al. 2012, *A&A*, 539, A93
- Szomoru, D., Franx, M., van Dokkum, P. G., et al. 2010, *ApJ*, 714, L244
- Szomoru, D., Franx, M., Bouwens, R. J., et al. 2011, *ApJ*, 735, L22
- Szomoru, D., Franx, M., & van Dokkum, P. G. 2012, *ApJ*, 749, 121
- Taylor, E. N., Franx, M., van Dokkum, P. G., et al. 2009, *ApJS*, 183, 295
- Toft, S., van Dokkum, P., Franx, M., et al. 2005, *ApJ*, 624, L9
- Toft, S., van Dokkum, P., Franx, M., et al. 2007, *ApJ*, 671, 285
- Trujillo, I., Förster Schreiber, N. M., Rudnick, G., et al. 2006, *ApJ*, 650, 18
- van Dokkum, P. G., Franx, M., Kriek, M., et al. 2008, *ApJ*, 677, L5
- van Dokkum, P. G., Whitaker, K. E., Brammer, G., et al. 2010, *ApJ*, 709, 1018
- van Dokkum, P. G., Brammer, G., Fumagalli, M., et al. 2011, *ApJ*, 743, L15
- Williams, R. J., Quadri, R. F., Franx, M., et al. 2010, *ApJ*, 713, 738
- Wuyts, S., Labbé, I., Schreiber, N. M. F., et al. 2008, *ApJ*, 682, 985

- Wuyts, S., Franx, M., Cox, T. J., et al. 2009, ApJ, 700, 799
- Wuyts, S., Förster Schreiber, N. M., van der Wel, A., et al. 2011, ApJ, 742, 96
- Wuyts, S., Förster Schreiber, N. M., Genzel, R., et al. 2012, ApJ, 753, 114
- Yuan, T.-T., Kewley, L. J., Swinbank, A. M., Richard, J., & Livermore, R. C. 2011, ApJ, 732, L14
- Zibetti, S., Charlot, S., & Rix, H.-W. 2009, MNRAS, 400, 1181

INSIGHTS INTO GALAXY SIZE GROWTH FROM SEMI-ANALYTIC MODELS

A major challenge facing the field of galaxy evolution lies in reconciling the observed structural evolution of galaxies with theoretical predictions. The discovery of extremely compact high-redshift galaxies in particular has prompted great efforts to understand their inferred size growth, with varying degrees of success. In this paper we investigate the size growth of quiescent galaxies as predicted by semi-analytical models. We analyze several SAMs with different prescriptions for galaxy physics in order to uncover robust predictions. By selecting galaxies in the same way as is done in observations, i.e., using mass-selected samples which are separated into quiescent and starforming subsamples using multi-color cuts, we can make a consistent comparison between models and observations. We find that the models closely match observed changes in the median sizes of quiescent galaxies: $r_{\text{eff}} \propto (1+z)^{-1.2}$, with very little difference between models. However, the large size difference between starforming and quiescent galaxies that is found in observations is not reproduced by these models. This points to a serious flaw in either the models or observations. On the whole, rapid galaxy size growth is a generic, robust feature, independent of details concerning gas dissipation or disk instabilities. Instead, it is more strongly driven by the underlying growth of dark matter halos and a few simple prescriptions for galaxy sizes. Quiescent and starforming galaxies grow at very similar rates in the models, which can be explained by the fact that newly quenched galaxies dominate the quiescent population in terms of number density. Although changes in the quiescent population are largely driven by the growth of starforming galaxies, we find that galaxies in SAMs still grow significantly in both mass and size after they quench. This growth is such that quiescent galaxies move onto a tight mass-size relation at high masses, regardless of the redshift at which they quenched. At lower masses ($M_* \lesssim 10^{11} M_\odot$), galaxies interact relatively little and consequently remain relatively untouched throughout their further life. As a result of this, at low stellar masses galaxy size correlates with both quenching epoch and mass-weighted age.

6.1 INTRODUCTION

The issue of galaxy size growth has dominated studies of high-redshift galaxy structure ever since the discovery of very small and massive quenched galaxies at $z > 1.5$ about a decade ago (e.g., Daddi et al. 2005; Trujillo et al. 2006; Toft et al. 2007; van Dokkum et al. 2008). Since the discovery of these extreme objects it has been found that both quenched and starforming galaxies are significantly smaller at high redshift compared to low-redshift galaxies of the same stellar mass (e.g., Trujillo et al. 2006; Williams et al. 2010). This size growth is accompanied by evolution in most other structural and morphological features: e.g., an increase in central concentration and surface density, and reddening of stellar populations (e.g., Williams et al. 2010; Szomoru et al. 2011; Bell et al. 2012). This change in average galaxy properties is smooth and continuous, and quite rapid. Perhaps surprisingly, quiescent galaxies have been found to evolve at least as rapidly as starforming galaxies, despite the fact that they have stopped forming new stars.

A robust median growth trend of $r_{\text{eff}} \propto (1+z)^{-1}$ has emerged for quiescent galaxies at fixed stellar mass (e.g., Williams et al. 2010; Damjanov et al. 2011, and references therein). Efforts to understand this trend have mainly focused on growth through minor, gas-poor mergers. Recent simulations have shown that a string of such mergers can transform typical $z = 2$ quiescent galaxies into massive $z = 0$ ellipticals (Naab et al. 2009; Oser et al. 2010; Oser et al. 2012; Oogi & Habe 2013; Bédorf & Portegies Zwart 2013). However, galaxy merger rates from observed pair fractions seem to indicate that minor merging does not occur often enough to drive all of the observed growth (Williams et al. 2011; Newman et al. 2012). Matters are further complicated by the difficulty of linking galaxies observed at different redshifts, and by differences in the criteria used to select galaxy samples.

Thus, although the size growth at fixed mass between $z = 2$ and the present day is quite well-measured, the interpretation of this measurement is not straightforward. One promising possibility lies in the use of semi-analytic models (SAMs). Using these models it is possible to relatively quickly test the effects of different implementations of galaxy physics such as gas dissipation or stellar feedback, and assess the importance of different physical processes for galaxy evolution. Such comparisons between analytic models and observations generally focus on the growth of either pure disks or strongly bulge-dominated galaxies, with the aim of studying specific growth mechanisms such as accretion from halos onto disks or growth due to mergers (e.g., Mo et al. 1999; Somerville et al. 2008; Shankar et al. 2013).

However, separating galaxies by morphology prevents consistent comparisons to observations, since high-redshift galaxies are usually selected based on star formation activity, which can be robustly measured using galaxy colors (Williams et al., 2009). Selecting galaxies by star formation activity not only alters the galaxy samples under consideration, but also changes the physical issue that is addressed. The central question becomes not how disks or bulges form, but rather how galaxies grow while forming stars, and what happens to them once they become inactive. It is clear that simulations must use the same type of galaxy selection as observations in order to answer this question.

In this paper we take a step in that direction by computing the size growth predic-

tions of several SAMs for galaxies which are selected in the same way as observed galaxy samples. Our purpose is not to validate the predictions of SAMs, but rather to use them as toy models for galaxy growth. The models analyzed in this paper are all based on the same dark matter simulation, but differ in the implementation of more detailed physics, such as baryon cooling or the treatment of disk instabilities. The different models thus provide an opportunity to investigate common predictions for a Λ CDM universe, while also highlighting the importance of second-order effects on galaxy structure.

6.2 GALAXY SIZES IN SEMI-ANALYTIC MODELS

We analyze the outputs of two semi-analytic models, both based on the Millenium dark matter simulation (Springel et al., 2005): the Bower et al. (2006) model, which is based on GALFORM (Cole et al., 2000); and the Guo et al. (2011) model, which builds on the models of Springel et al. (2005), Croton et al. (2006) and De Lucia & Blaizot (2007). Output catalogs for these SAMs are available publicly at <http://www.virgo.dur.ac.uk/> and <http://www.mpa-garching.mpg.de/millennium/>.

In terms of structure, galaxies in these SAMs are modeled as a combination of two components: a flat disk and a central bulge. Galaxies initially form as stellar disks, which can then merge or collapse into bulges. Disk growth is calculated following the formalism of Mo et al. (1998). In this formalism diffuse hot halo gas cools into a flat disk under the assumption of angular momentum conservation. Subsequent star formation then transforms this gas disk into a stellar disk, which is assumed to have the same specific angular momentum as the gas disk. Additional material can accrete onto it, changing its mass and angular momentum, and thereby its size.

Bulge formation is implemented in two ways. Firstly, stellar disks can become unstable and fragment if their surface density exceeds some threshold. This threshold is calculated in similar ways in both models, but the subsequent disk fragmentation is treated in different ways. In the Bower et al. (2006) model, when disks become unstable their entire mass is transferred to the central bulge, while Guo et al. (2011) remove matter from the disk until it becomes marginally stable again. This results in a more gradual buildup of bulges and depletion of disks. In either case the resulting bulge size is calculated assuming virial equilibrium.

The second mechanism for bulge growth is through galaxy mergers. There are several possible outcomes for a merger between two galaxies, depending on their mass-ratio. If two equal-mass galaxies merge, all their stellar matter will be transferred into a central bulge. In the case of unequal-mass mergers, all the stellar mass of the lower-mass galaxy is transferred into the massive galaxy's bulge, but the disk of the higher-mass galaxy (if present) is left undisturbed. In both models the presence of gas in the merging galaxies may trigger a central starburst. However, energy loss due to gas dissipation is not implemented in either model; this can result in unrealistically large sizes for intermediate-mass bulge-dominated galaxies (Shankar et al., 2013).

The SAM catalogs provide a disk scalelength and a bulge half-mass radius for each galaxy, as well as total stellar masses and bulge mass fractions. For each galaxy we can thus construct radial stellar mass surface density profiles for the disk and bulge components separately, which we then combine to obtain total stellar mass surface density profiles.

Stellar disks are assumed to be infinitely thin and follow exponential profiles:

$$\Sigma_{*,\text{disk}} = \Sigma_{0,\text{disk}} e^{-r/r_d}, \quad (6.1)$$

where r_d is the disk scalelength. Bulge profiles are calculated by deprojecting the three-dimensional half-mass radius and inserting it into an $n = 4$ Sérsic profile (Sérsic, 1968):

$$\Sigma_{*,\text{bulge}} = \Sigma_{\text{eff,bulge}} e^{[-7.67(r/r_{\text{eff,bulge}})^{-1/4} - 1]}. \quad (6.2)$$

The total mass profile can now be straightforwardly obtained by summing the disk and bulge profiles. The half-mass radius of the galaxy is then calculated by integrating the total mass profile.

It is important to note that the effective radii calculated for the galaxies in these SAMs are based on stellar mass distributions, as opposed to the stellar light distributions used in most observations. Szomoru et al. (2013) have shown that the half-mass radii of massive galaxies are on average 25% smaller than their half-light radii, at all redshifts out to $z = 2.5$. The difference between half-mass radius and half-light radius does not seem to depend on redshift or galaxy properties, and therefore the comparison between observed size evolution from half-light radii to size evolution from model half-mass radii should be affected in the same way at all redshifts and should be independent of the sample of galaxies under consideration. Since in this paper we focus on the relative size difference between different redshifts, this constant factor is not a concern.

6.3 GALAXY SELECTION

In order to make a meaningful comparison between the models and observations we use selection criteria commonly used at high redshift. We split the galaxy catalog into quiescent and starforming subsamples using a two-color selection criterium (e.g., Williams et al. 2009). Our color-color cut is calibrated at each redshift using the SFR information in the Guo et al. (2011) catalog. The effectiveness of this color selection is demonstrated in Figure 6.1, where we show the mean SSFR of galaxies in the $u - r - r - z$ plane, at $z = 0$ and $z = 2$. Our selection box, indicated by the dashed lines, is adjusted to optimally separate starforming and quiescent galaxies.

SSFR-based selections and morphological selections are sometimes used interchangeably, since morphology is known to strongly correlate with SSFR at redshifts up to at least $z \sim 2$ (Szomoru et al. 2011; Bell et al. 2012). In the case of simulations and low-redshift observations it is fairly straightforward to obtain detailed morphological information. At high redshift, however, the difficulty of obtaining reliable morphological information has forced observers to distinguish between galaxy populations using SSFR-based quantities.

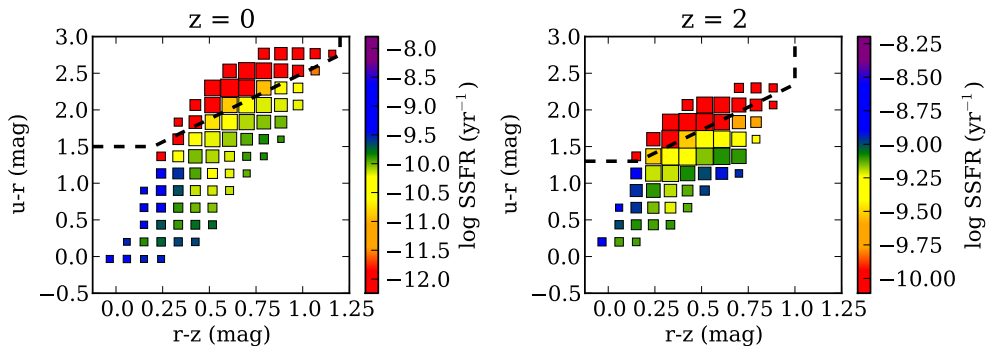


Figure 6.1: $u - r$ versus $r - z$ colors for massive ($10^{10.5} < M_*/M_\odot < 10^{11}$) galaxies from the Guo et al. 2011 SAM catalog, at $z = 0$ and $z = 2$. Color coding indicates SSFR. The dashed lines indicate our quiescent galaxy selection limits. Quiescent galaxies in the models occupy a well-defined region in the urz plane, and can be effectively selected using a two-color selection.

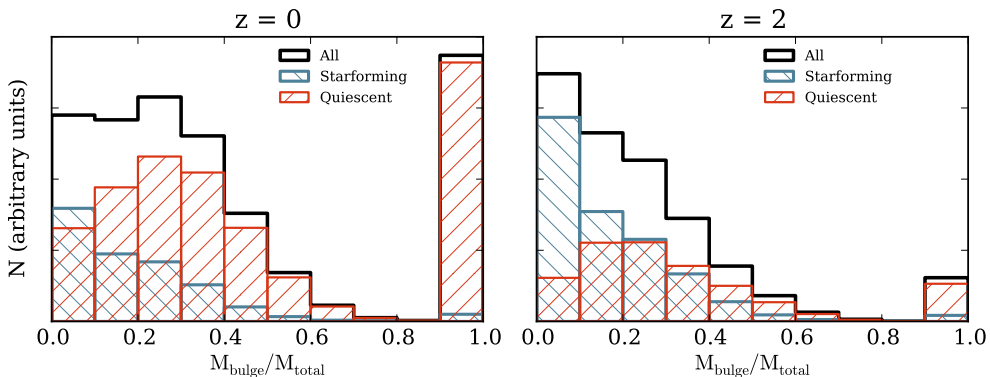


Figure 6.2: The distribution of bulge-to-total mass ratios for quiescent galaxies, starforming galaxies, and all galaxies (red, blue and black histograms, respectively) in the Guo et al. (2011) catalog, with stellar masses $10^{10.5} < M_*/M_\odot < 10^{11}$. The distributions are shown at $z = 0$ and $z = 2$. The distribution of bulge-to-total ratios is very broad, both for quiescent and starforming galaxies. This is the case at all redshifts up to $z = 6$. The median bulge fraction of quiescent galaxies is quite, even at low redshift; at $z = 0$ it is equal to 0.29. It is therefore important to select on star formation activity - not bulge fractions - when comparing model predictions to observations of passive galaxies.

It is important to realize that there is a significant difference between these two selection methods. Although quiescent galaxies are more spheroidal relative to starforming galaxies at all redshifts (i.e., more concentrated, higher Sérsic indices, higher velocity dispersions), they are not necessarily spheroids in an absolute sense. Sérsic indices of quiescent galaxies at $z \sim 2$ are significantly lower than at $z = 0$, and axis ratio distributions suggest that galaxies become more disk-like at high redshift (van der Wel et al. 2011; Chang et al. 2013a;

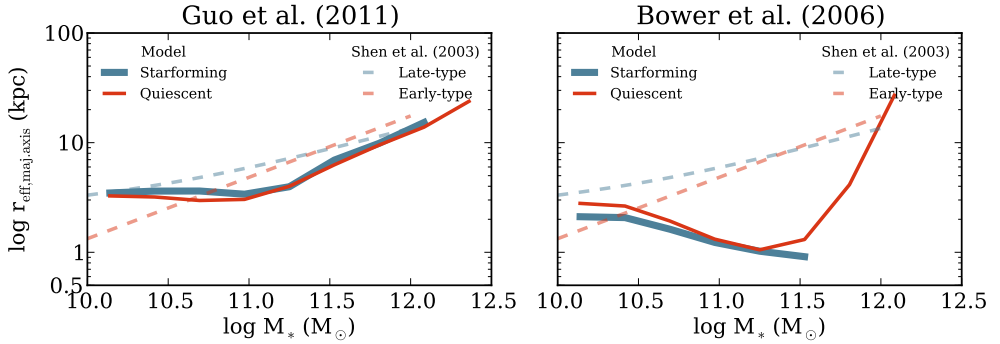


Figure 6.3: Median $z = 0$ mass-size relations for *urz*-selected quiescent (red) and starforming (blue) galaxies in the Guo et al. (2011) and Bower et al. (2006) models. Observations from Shen et al. (2003) are shown as dashed lines (observed values have been corrected from circularized to major-axis radii). Starforming and quiescent galaxies lie on very similar mass-size relations in both models, which is in agreement with observations in this mass range. The observed slope of the mass-size relation is reasonably well reproduced by the Guo et al. (2011) model, but the Bower et al. (2006) model incorrectly produces a negative slope.

Chang et al. 2013b). Thus, the structure of galaxies changes significantly over this redshift range, which can introduce serious biases into samples which are selected by bulge fraction or concentration.

As an illustration we plot the distribution of bulge-to-total mass ratios for galaxies in the Guo et al. (2011) catalog in Figure 6.2. Quiescent galaxies, starforming galaxies, and the entire galaxy sample are shown in red, blue and black, respectively. It is immediately apparent that in these models a selection based on bulge fraction (or, equivalently, Sérsic index) is not equivalent to a selection based on star formation activity. Cuts of $M_{*,\text{bulge}}/M_{*,\text{total}} > 0.3$ or 0.7 result in either enormous contamination from starforming galaxies (for low $M_{*,\text{bulge}}/M_{*,\text{total}}$ cuts) or exclusion of the majority of quiescent galaxies (for high $M_{*,\text{bulge}}/M_{*,\text{total}}$ cuts). Thus, in order to make a meaningful comparison to high-redshift observations, it is very important to use a star formation-based selection method.

6.4 GALAXY GROWTH

THE MASS-SIZE RELATION AT $Z=0$

Before addressing the redshift evolution of galaxy sizes it is worthwhile to look at galaxy masses and sizes at $z = 0$, since the models are calibrated to observations at this redshift. In Figure 6.3 we plot the median mass-size relations of starforming and quiescent galaxies in the Guo et al. (2011) and Bower et al. (2006) models as solid lines (left and right panel, respectively). The purple and yellow lines indicate the mass-size relations for late-type and early-type galaxies from Shen et al. (2003). The Shen et al. (2003) values have been corrected from circularized to major-axis radii using median axis ratios for late-type and early-type

galaxies.

The Guo et al. (2011) model performs quite well, producing mass-size relations at $z = 0$ that are in quite close agreement with observations. The overall trend of increasing stellar mass with increasing galaxy sizes is reproduced fairly well, although the slope at low masses ($M_* < 10^{11} M_\odot$) is too low. The size difference between quiescent and starforming galaxies, which is clearly visible in the data at $M_* < 10^{11} M_\odot$, is completely absent in the model. This may be due to the fact that energy loss due to gas dissipation is not implemented in the model's treatment of mergers. Shankar et al. (2013) show that including this process results in smaller sizes for galaxies with $M_* < 10^{11} M_\odot$. However, this does not significantly increase the size difference between starforming and quiescent galaxies (Shankar 2013, private communication).

The Bower et al. (2006) model predicts a mass-size relation that has a negative slope up to $M_* = 10^{11.5} M_\odot$, and has very large scatter at masses above $10^{11} M_\odot$. This is clearly in contradiction with observations. This problem has been the subject of several studies (e.g., González et al. 2009; Shankar et al. 2010a; Shankar et al. 2010b), and is the result of a combination of factors, including the strength of supernova feedback, the effects of dark matter during galaxy mergers, and the treatment of disk instabilities.

GROWTH AT FIXED MASS

It is clear that SAMs have difficulties in reproducing certain aspects of galaxy structure. The Bower et al. (2006) model, in particular, predicts a relation between stellar mass and size that deviates strongly from observations. As shown by Shankar et al. (2010), the normalization of the Bower et al. (2006) mass-size relation changes with redshift, but the overall shape remains roughly the same. This means that the relative size growth of galaxies might not be strongly affected by issues regarding the shape of the mass-size relation. In Figure 6.4 we compare SAM predictions for galaxy size growth to recent observations by van der Wel et al. (2013, in prep.). We calculate the median effective radii of galaxies with $10^{10.5} < M_*/M_\odot < 10^{11}$, separating them into quiescent and starforming samples as described in Section 6.3 (top panels), and into pure bulges and pure disks (bottom panels). Model values are shown as solid lines, while the data points indicate observations from van der Wel et al. (2013, in prep.). These authors have separated their galaxies using a UVJ color selection, which is comparable to the urz selection we use in this paper. The α values of power-law fits of the form $r_{\text{eff}} \propto (1+z)^\alpha$ are provided for each subsample.

The models are remarkably consistent in their predictions; quiescent galaxies grow as $\approx (1+z)^{-1.2}$, well within the range of values measured in observations (e.g., Williams et al. 2010; Damjanov et al. 2011, and many others). The similarity of the predictions of the two models provides important clues regarding the drivers of galaxy size growth; the processes leading to rapid galaxy size growth must be fairly generic and fundamental. The most obvious of these is the dark matter simulation on which the two SAMs are based, which strongly influences the merging behaviour of halos and galaxies. Secondly, the basic prescriptions for galaxy sizes are very similar: gas cooling and subsequent star formation follow roughly the

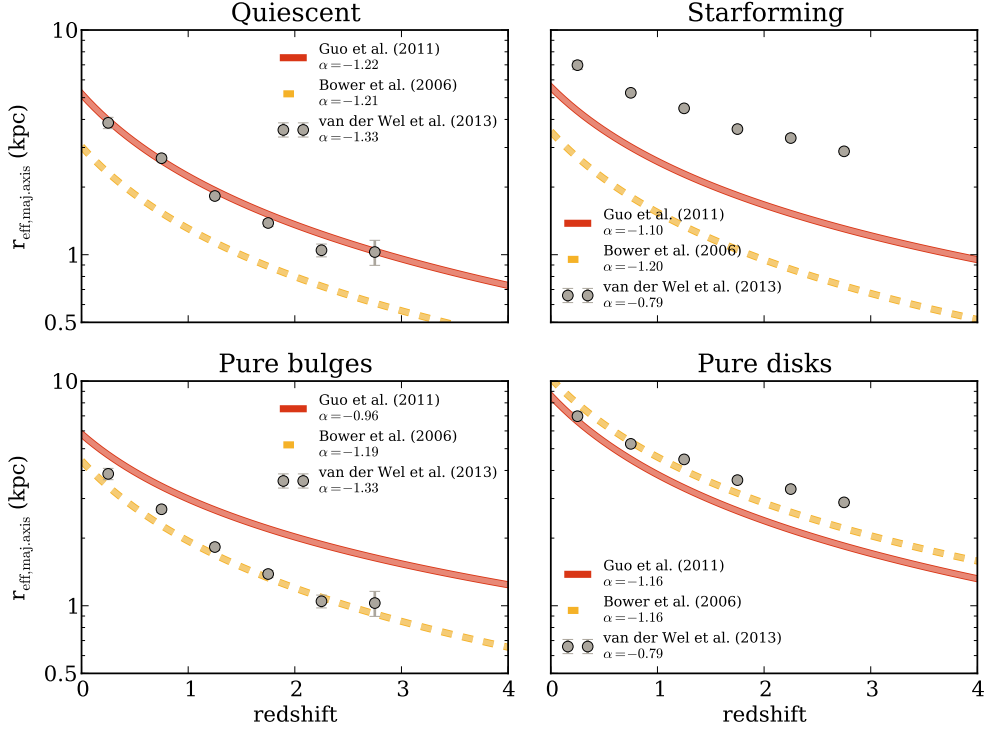


Figure 6.4: Top panels: median size evolution of quiescent and starforming galaxies with stellar masses $10^{10.5} < M_*/M_\odot < 10^{11}$. Red (solid) and yellow (dashed) lines indicate predictions from the Guo et al. (2011) and Bower et al. (2006) models, and observed values from van der Wel et al. 2013 are indicated by the grey data points. Error bars indicate the errors on the median values. Best-fit α parameters from $(1+z)^\alpha$ power law fits are shown. The models robustly predict $\alpha \approx -1.2$ for quiescent galaxies, which is in good agreement with observations. The growth of starforming galaxies is somewhat overestimated in the models, and the sizes of starforming galaxies are on average a factor $\sim 2-4$ too small. Bottom panels: median size evolution of pure bulge and pure disk galaxies in the same mass range. In the Guo et al. (2011) model bulges grow more slowly than quiescent galaxies. In the Bower et al. (2006) model there is very little difference, possibly due to the more rapid action of disk instabilities in this SAM. Pure disk galaxies grow at a rate that is very close to that of starforming galaxies.

same formalism, and the calculation of bulge sizes is based on the same virial arguments. However, disk rotation velocities are calculated in slightly different ways, and the Guo et al. (2011) model treats gas disks and stellar disks separately. Furthermore, disk instabilities act on very different timescales in the two models. As pointed out in Section 6.4, these differences have considerable consequences for observables such as the slope and scatter of the mass-size relation, as well as the absolute sizes of galaxies, but they do not seem to strongly affect zeroth order galaxy growth.

Both models predict that starforming galaxies grow at a rate that is very similar to that of quiescent galaxies: in the models starforming galaxies grow as $\approx (1+z)^{-1.15}$, which is

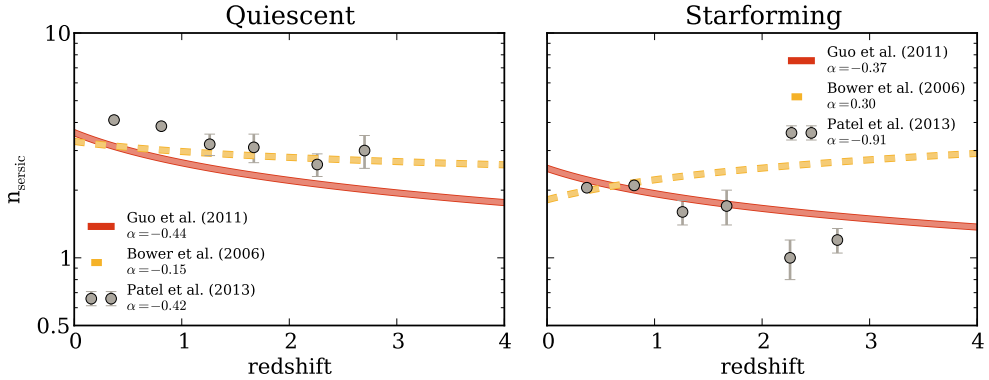


Figure 6.5: Evolution in the mean Sérsic index of galaxies with stellar masses $10^{10.5} < M_*/M_{\odot} < 10^{12}$. Red (solid) and yellow (dashed) lines indicate predictions from the Guo et al. (2011) and Bower et al. (2006) models, and observed values from Patel et al. (2013) are indicated by the grey data points. Error bars indicate the errors on the median values. Best-fit α parameters from $(1+z)^{\alpha}$ power law fits are shown. The Guo et al. (2011) model performs very well, predicting Sérsic indices that are very close to observations both in terms of their absolute value and their relative increase with time. The Bower et al. (2006) model correctly predicts the increase in Sérsic index for quiescent galaxies, but does not match the observations for starforming galaxies.

consistent with observations (e.g., Dahlen et al. 2007; Nagy et al. 2011; Mosleh et al. 2012;). In principle there is no reason that these two types of galaxies should grow at similar rates, since the processes that contribute to their build-up are quite different. However, the number density of quiescent galaxies increases by almost an order of magnitude from $z = 2$ to $z = 0$, which means that the quiescent population is always dominated by recently quenched galaxies (e.g., van der Wel et al. 2009; Carollo et al. 2013). Even if galaxies completely stop growing after they quench, the quiescent population as a whole will still grow in size, simply because it is fed with ever-larger starforming galaxies. The degree to which this mechanism dominates is dependent on the size difference between starforming and quiescent galaxies. Figure 6.4 shows that this difference is too small in the models, which may point to a problem in the treatment of the structural transformation that accompanies quenching.

We illustrate the changes in galaxy morphology in Figure 6.5, where we show the change in the mean Sérsic index of quiescent and starforming galaxies. The models are indicated by red (solid) and yellow (dashed) lines, and observations from Patel et al. (2013) are shown as grey datapoints. The model Sérsic indices have been calculated by fitting Sérsic profiles to the 1-D surface density profiles of all the galaxies. Observations show that galaxy Sérsic indices increase quite strongly with time, both for starforming and quiescent galaxies. The Guo et al. (2011) model predicts a rate of increase in the Sérsic indices of quiescent galaxies that is remarkably close to the observations, but underpredicts the change for starforming galaxies. Similarly, the Bower et al. (2006) model performs reasonably well for quiescent galaxies, but very poorly for starforming galaxies. In both models Sérsic indices tend to be low compared to observations; this is most likely simply due to the fact that in

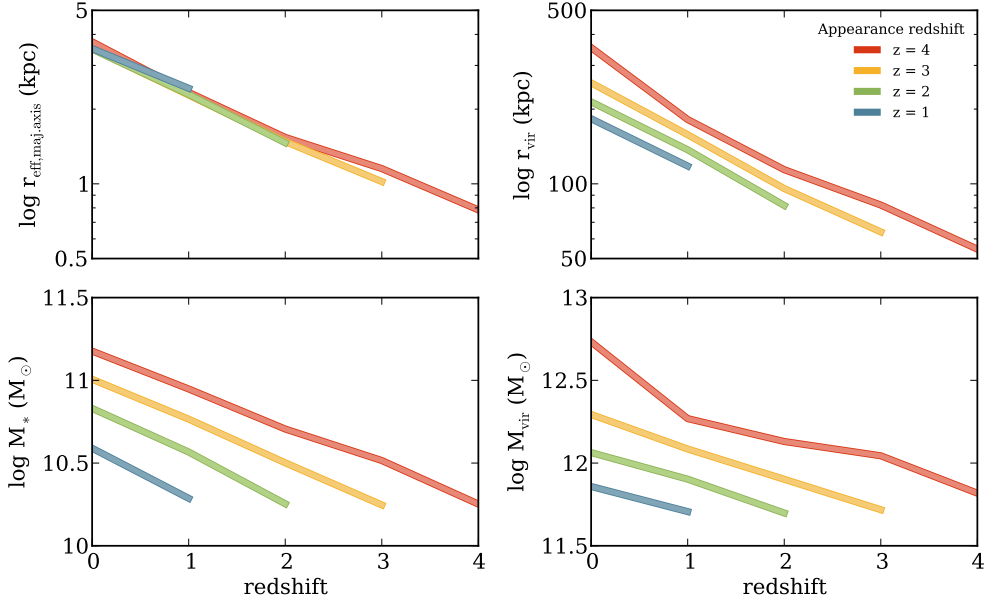


Figure 6.6: Growth in median size, virial radius, stellar mass, and virial mass for starforming galaxies, measured by tracing the descendants of $10^{10} M_{\odot}$ galaxies down to low redshift. Each color corresponds to galaxies which crossed the $10^{10} M_{\odot}$ mass threshold at different redshifts. For clarity, galaxies which quench before $z = 0$ are not shown. Galaxy sizes evolve at almost the same rate as the virial radii of their parent halos: $r_{\text{eff}} \propto (1+z)^{-1.2}$, and $r_{\text{vir}} \propto (1+z)^{-1.3}$. Stellar masses increase slightly faster than virial masses: $M_* \propto (1+z)^{-1.7}$, and $M_{\text{vir}} \propto (1+z)^{-1.2}$.

the models the maximum Sérsic index is $n = 4$ (for a pure bulge), while observed values can be much higher.

THE GROWTH OF STARFORMING GALAXIES

Newly quenched galaxies make up the bulk of the quiescent population; understanding changes in the population of quiescent galaxies therefore becomes a matter of understanding the growth of starforming galaxies. A very naive expectation is that the sizes of stellar disks scale as the virial radii of their parent halos. We investigate this simple assumption by tracking the growth of starforming galaxies. We select populations of starforming galaxies with stellar masses of $10^{10} M_{\odot}$ and identify their descendants down to $z = 0$. This allows us to measure the actual growth of starforming galaxies. Stellar half-mass sizes and virial radii of these galaxies and their parent halos are plotted in Figure 6.6. For clarity, only galaxies which remain unquenched until $z = 0$ are shown. This has no influence on our results; galaxies which quench at earlier redshifts follow almost identical growth tracks to those which survive until $z = 0$.

Stellar mass and size (left panels) very closely follow virial mass and size (right panels).

Galaxies which form later tend to have lower masses for their size (i.e., lower effective densities), but the rate of size and mass growth is independent of stellar mass. In fact, the most striking aspect of Figure 6.6 is that in these models the relative growth in mass and size of star-forming galaxies is very similar, regardless of the stellar mass of these galaxies or the redshift at which they quench. Starforming galaxies grow in size at a rate that is very close to the rate at which their parent halo virial radii increase: $r_{\text{eff}} \propto (1+z)^{-1.2}$, and $r_{\text{vir}} \propto (1+z)^{-1.3}$. Stellar masses increase slightly faster than virial masses: $M_* \propto (1+z)^{-1.7}$, and $M_{\text{vir}} \propto (1+z)^{-1.2}$. Thus, to first order, individual starforming galaxies simply grow in lockstep with their parent halos.

GALAXY SIZES AND QUENCHING

As noted in Section 6.4, the SAMs considered in this paper predict very similar mass-size relations for starforming and quiescent galaxies. This is at odds with observations, especially at $z > 0$ (see Figure 6.4). Observed starforming galaxies are on average a factor $\sim 2 - 3$ larger than quiescent galaxies at the same stellar mass, while in the models this size difference is on the order of $\sim 10\%$. Apparently galaxy sizes in the models are unaffected by quenching processes. The inclusion of gas dissipation effects during gas-rich mergers (Shankar et al., 2013) does not seem to resolve this problem.

In any case, the lack of size decrease during quenching may have serious consequences for conclusions regarding galaxy structure and galaxy sizes. It implies that no significant structural changes occur during quenching, which is at odds with observed correlations between star formation activity and galaxy structure (e.g., Bell et al. 2012). Relative growth trends should not be strongly affected by this fundamental flaw, but absolute sizes, concentrations, and other parameters should be considered extremely uncertain.

6.5 THE FATE OF QUENCHED GALAXIES

Although the quenching of starforming galaxies contributes significantly to the evolution of the median size of quiescent galaxies, it is very unlikely that quenched galaxies undergo no changes at all. The absence of a significant number of very old, compact galaxies at $z = 0$ means that most, if not all, quiescent galaxies must evolve significantly between $z > 2$ and $z = 0$ (Taylor et al., 2010). We investigate this evolution by selecting galaxies at the moment they quench, and then linking these galaxies to their descendants at lower redshift.

In Figure 6.7 we plot the median evolution in size, virial radius, stellar mass, and virial mass for populations of galaxies quenched at different redshifts. After quenching, "passive" galaxies strongly grow in both size and mass. The rate of stellar mass growth is roughly independent of quenching redshift, although lower-mass galaxies tend to grow slightly more slowly than massive galaxies. Virial mass and size growth are similarly independent of quenching redshift. Galaxy size growth, on the other hand, is slow for recently quenched galaxies, and speeds up as galaxies become older. This results in a negative corre-

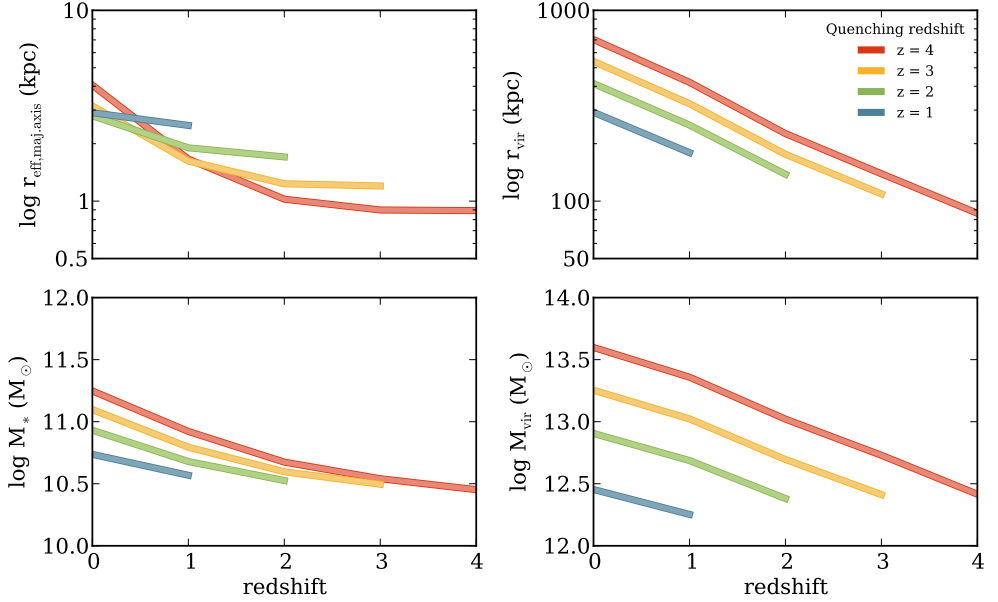


Figure 6.7: Growth in median size, virial radius, stellar mass, and virial mass for galaxies quenched at different redshifts. Both in the Guo and Bower models galaxies grow quite strongly in stellar mass after quenching, at a rate that is mostly independent of quenching redshift. Concurrent with this mass growth, galaxies sizes increase and virial radii and masses increase. At all redshifts older galaxies tend to be more massive and are located in larger halos. This is not the case for galaxy sizes; at high redshift the oldest galaxies tend to be the smallest, while between $z = 0$ and $z = 1$ older galaxies tend to be the largest.

lation between galaxy age and galaxy size at high redshift, which becomes positive between $z = 1$ and $z = 0$.

In order to disentangle the growth in mass and in size, we plot the $z = 0$ mass-size relations for galaxies quenched at different redshifts in Figure 6.8. The solid lines indicate the present-day median mass-size relations for galaxies quenched at different redshifts. At high masses, galaxies of different ages fall onto the same mass-size relation. This same behaviour can be seen at higher redshifts (lower panels). High-mass galaxies undergo a relatively large amount of mergers, which move them onto a common mass-size relation, regardless of when they were quenched. At low masses, however, galaxy growth is dominated by disk instabilities, and mergers play a minor role (e.g., Guo et al. 2011; Shankar et al. 2013). These galaxies therefore tend to remain at the same mass and size after they quench, which results in a clear trend of decreasing size with increasing quenching redshift.

The models analysed in this paper robustly predict that the scatter in age decreases with redshift (at $M_* < 10^{10.5}$). This seems to contradict observations, which show that there is little variation in the scatter up to $z = 2$ (e.g., Newman et al. 2012). However, it is important to realize that observations of the mass-size relation at high redshift are generally

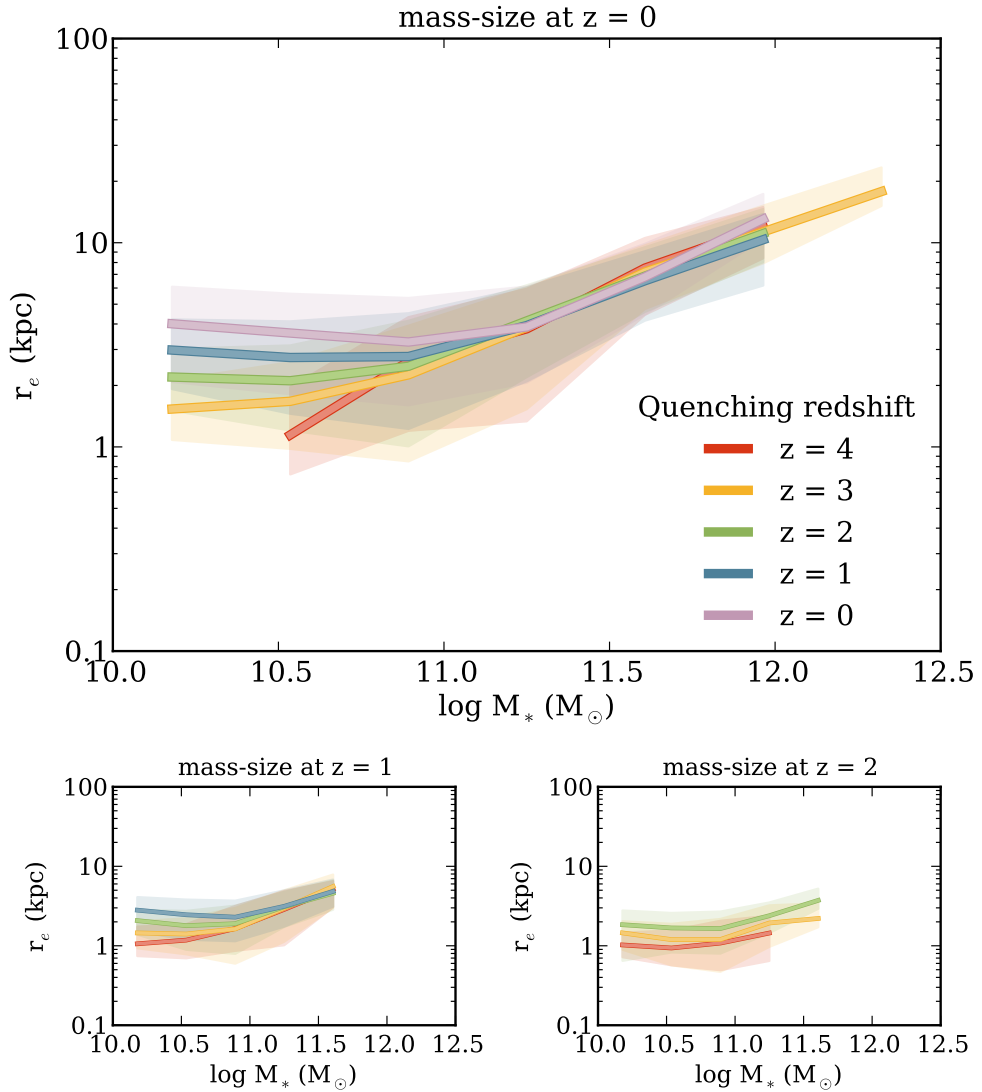


Figure 6.8: Running median of size as a function of stellar mass at $z = 0$ (top panel) and higher redshifts (lower panels) for galaxies quenched at different redshifts. At high masses ($M_* > 10^{11} M_\odot$) galaxies from different epochs lie on a tight mass-size relation. At low masses, however, there is a correlation between quenching redshift and median galaxy size: galaxies which quench early are small compared to galaxies which have quenched late.

only complete down to $M_* \approx 10^{10.5} M_\odot$. Furthermore, power-law fits in the mass-size plane are typically constrained to $M_* > 10^{11} M_\odot$. In this region the models predict no changes in the scatter. Galaxy samples with mass limits around $10^{10} M_\odot$ or lower are needed to properly test this prediction.

It should be noted that the SAMs considered in this paper do not include gas dissipation effects during mergers. As shown in Shankar et al. (2013), including such effects results in smaller galaxy sizes for low-mass ($M_* \sim 10^{10} M_\odot$) galaxies. Since gas fractions increase with redshift, the oldest quenched galaxies should be affected more strongly by this effect than more recently quenched galaxies. Therefore, including gas dissipation will only strengthen the age-size trend visible in Figure 6.8, while leaving high-mass galaxies unaffected.

Although it is obvious from Figure 6.8 that galaxies of different ages have different median sizes at fixed mass, the high number density of galaxies quenched at the lowest redshifts (i.e., the purple and blue lines) may completely wash out this trend in observations. We investigate this in Figure 6.9, by plotting the mean quenching redshift and mass-weighted age in bins of stellar mass and size. Although the age-size correlation is not as obvious as in Figure 6.8, there is clearly a trend. This result is in rough agreement with observations by van der Wel et al. (2009), although the strength of the correlation is weaker in the models, especially at high stellar masses. This may be due to the small size difference between starforming and quiescent galaxies in the models; since the initial spread in sizes of old and newly quenched galaxies is smaller, it takes fewer mergers to wash out the age-size correlation as galaxies move along the mass-size relation.

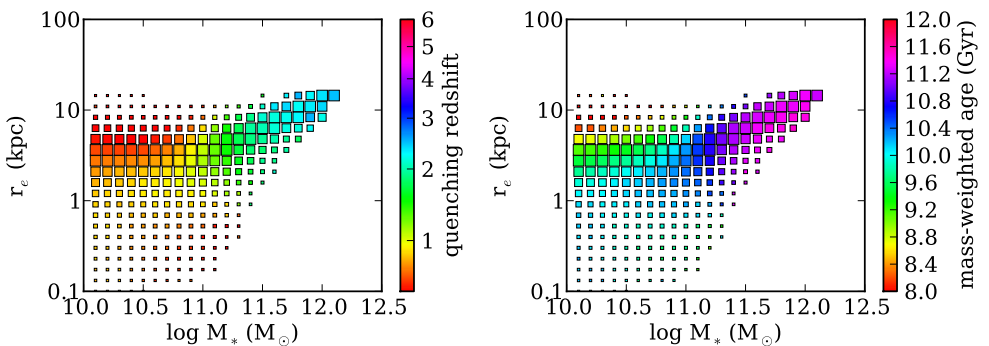


Figure 6.9: Mean quenching redshifts and mass-weighted ages for quiescent galaxies at $z = 0$, as a function of stellar mass and size. High-mass galaxies are on average older and have quenched earlier than low-mass galaxies. At low masses there is a trend between age with size, such that smaller galaxies are on average older than larger galaxies.

6.6 CONCLUSIONS

In this paper we have analysed galaxy size growth as predicted by semi-analytic models. A comparison between different models allows us to identify the aspects of galaxy evolution that are robust to changes in physics implementations, and extract generic predictions regarding galaxy growth. By selecting model galaxies in the same way as is done in observations we can make consistent comparisons between the two. We have compared the growth of model galaxies at fixed mass to recent observations, finding that both SAMs closely match observed quiescent galaxy size growth, despite differences in the exact implementations of disk and bulge assembly. Size growth $\propto (1+z)^{-1}$ seems to be a generic property of these models, driven by the underlying Λ CDM cosmology and very basic assumptions regarding the structure of galaxy bulges and disks.

Starforming galaxies grow at a rate comparable to quiescent galaxies, which can be explained by the fact that recently quenched galaxies dominate the number density of quiescent galaxies at all redshifts. Therefore the bulk of the average size growth of quiescent galaxies is driven by the growth of starforming galaxies. By tracking the growth of populations of starforming galaxies over time we have shown that these galaxies grow almost in lockstep with their parent halos. Thus the size growth of starforming galaxies is very simply tied to the growth of dark matter halos. An important issue is that the size difference between starforming and quiescent galaxies in the models is almost negligible, while in observations this difference is quite large (a factor $\sim 2 - 4$). This may simply be due to the lack of energy loss due to gas dissipation during gas-rich galaxy mergers, but could also point to severe deficiencies in our understanding of the mechanisms that cause quenching. It is unclear how this issue may be resolved.

Galaxies continue to grow quite rapidly after they quench, increasing in mass and size at a rate comparable to starforming galaxies. The mechanisms by which quiescent galaxies grow depend on galaxy mass. Massive galaxies undergo repeated mergers, which force them onto a tight mass-size relation at $M_* > 10^{11} M_\odot$. At lower masses, quiescent galaxy growth is more strongly driven by disk instabilities instead of mergers. Consequently, low-mass quiescent galaxies tend to remain relatively stationary in the mass-size plane. This results in a strong anticorrelation between galaxy age and galaxy size at $M_* < 10^{11} M_\odot$.

REFERENCES

- Bédorf, J., & Portegies Zwart, S. 2013, *MNRAS*, 431, 767
- Bell, E. F., van der Wel, A., Papovich, C., et al. 2012, *ApJ*, 753, 167
- Bower, R. G., Benson, A. J., Malbon, R., et al. 2006, *MNRAS*, 370, 645
- Carollo, C. M., Bschorr, T. J., Renzini, A., et al. 2013, arXiv:1302.5115
- Chang, Y.-Y., van der Wel, A., Rix, H.-W., et al. 2013, *ApJ*, 762, 83
- Chang, Y.-Y., van der Wel, A., Rix, H.-W., et al. 2013, arXiv:1305.6931
- Cole, S., Lacey, C. G., Baugh, C. M., & Frenk, C. S. 2000, *MNRAS*, 319, 168
- Croton, D. J., Springel, V., White, S. D. M., et al. 2006, *MNRAS*, 365, 11
- Daddi, E., Renzini, A., Pirzkal, N., et al. 2005, *ApJ*, 626, 680
- Dahlen, T., Mobasher, B., Dickinson, M., et al. 2007, *ApJ*, 654, 172
- Damjanov, I., Abraham, R. G., Glazebrook, K., et al. 2011, *ApJ*, 739, L44
- De Lucia, G., & Blaizot, J. 2007, *MNRAS*, 375, 2
- González, J. E., Lacey, C. G., Baugh, C. M., Frenk, C. S., & Benson, A. J. 2009, *MNRAS*, 397, 1254
- Guo, Q., White, S., Boylan-Kolchin, M., et al. 2011, *MNRAS*, 413, 101
- Mo, H. J., Mao, S., & White, S. D. M. 1998, *MNRAS*, 295, 319
- Mo, H. J., Mao, S., & White, S. D. M. 1999, *MNRAS*, 304, 175
- Mosleh, M., Williams, R. J., Franx, M., et al. 2012, *ApJ*, 756, L12
- Naab, T., Johansson, P. H., & Ostriker, J. P. 2009, *ApJ*, 699, L178
- Nagy, S. R., Law, D. R., Shapley, A. E., & Steidel, C. C. 2011, *ApJ*, 735, L19
- Newman, A. B., Ellis, R. S., Bundy, K., & Treu, T. 2012, *ApJ*, 746, 162
- Oogi, T., & Habe, A. 2013, *MNRAS*, 428, 641
- Oser, L., Ostriker, J. P., Naab, T., Johansson, P. H., & Burkert, A. 2010, *ApJ*, 725, 2312
- Oser, L., Naab, T., Ostriker, J. P., & Johansson, P. H. 2012, *ApJ*, 744, 63
- Patel, S. G., van Dokkum, P. G., Franx, M., et al. 2013, *ApJ*, 766, 15
- Sérsic, J. L. 1968, *Atlas de galaxias australes* (Cordoba, Argentina: Observatorio Astronómico, 1968)
- Shankar, F., Marulli, F., Bernardi, M., et al. 2010, *MNRAS*, 403, 117
- Shankar, F., Marulli, F., Bernardi, M., et al. 2010, *MNRAS*, 405, 948
- Shankar, F., Marulli, F., Bernardi, M., et al. 2013, *MNRAS*, 428, 109
- Shen, S., Mo, H. J., White, S. D. M., et al. 2003, *MNRAS*, 343, 978
- Somerville, R. S., Barden, M., Rix, H.-W., et al. 2008, *ApJ*, 672, 776
- Springel, V., White, S. D. M., Jenkins, A., et al. 2005, *Nature*, 435, 629
- Szomoru, D., Franx, M., Bouwens, R. J., et al. 2011, *ApJ*, 735, L22
- Szomoru, D., Franx, M., van Dokkum, P. G., et al. 2013, *ApJ*, 763, 73
- Taylor, E. N., Franx, M., Glazebrook, K., et al. 2010, *ApJ*, 720, 723
- Toft, S., van Dokkum, P., Franx, M., et al. 2007, *ApJ*, 671, 285
- Trujillo, I., Förster Schreiber, N. M., Rudnick, G., et al. 2006, *ApJ*, 650, 18
- Trujillo, I., Feulner, G., Goranova, Y., et al. 2006, *MNRAS*, 373, L36
- van der Wel, A., Bell, E. F., van den Bosch, F. C., Gallazzi, A., & Rix, H.-W. 2009, *ApJ*,

698, 1232

van der Wel, A., Rix, H.-W., Wuyts, S., et al. 2011, ApJ, 730, 38

van Dokkum, P. G., Franx, M., Kriek, M., et al. 2008, ApJ, 677, L5

Williams, R. J., Quadri, R. F., Franx, M., van Dokkum, P., & Labbé, I. 2009, ApJ, 691, 1879

Williams, R. J., Quadri, R. F., Franx, M., et al. 2010, ApJ, 713, 738

Williams, R. J., Quadri, R. F., & Franx, M. 2011, ApJ, 738, L25

CONCLUSIONS

The study of galaxy evolution is central to our understanding of the composition and evolution of the universe. However, linking observations to theory is significantly impeded by many uncertainties, both observational and theoretical. Three issues have been addressed in this thesis: the accuracy and interpretation of measurements of the sizes of high-redshift galaxies; the more general determination of galaxy structure and the discrepancy between light distributions and stellar mass distributions; and the interpretation of observed evolutionary trends in the context of galaxy formation models.

Our main conclusions are the following:

- On average, the effective radii of quiescent galaxies at $z \sim 2$ are only ~ 1 kpc (with a significant spread towards smaller and larger sizes). These small sizes are not the result of surface brightness-dependent biases.
- Quiescent galaxies at $z \sim 2$ are structurally quite similar to present-day elliptical galaxies; their morphologies are smooth and follow $n \approx 4$ Sérsic profiles.
- A comparison of the surface brightness profiles of high-redshift quiescent galaxies to those of low-redshift ellipticals suggests that quiescent galaxy growth occurs in an inside-out fashion.
- The average size difference between quiescent galaxies at $z = 2$ and $z = 0$ is not a reflection of the growth of individual galaxies. The growth of high-redshift quiescent galaxies may be as low as half of this average size difference, with the remaining part driven by the addition of large, recently quenched galaxies to the quiescent population.
- Galaxy structure correlates with star formation activity at all redshifts up to $z = 2$, such that starforming galaxies are more disk-like and more extended than quiescent galaxies.
- The overwhelming majority of galaxies has negative radial color gradients such that the cores of galaxies are redder than the outskirts. These color gradients indicate the presence of mass-to-light ratio gradients.
- The mass distributions of galaxies are on average 25% smaller than their rest-frame optical light distributions. The difference between mass-weighted structure and light-weighted structure is independent of redshift and galaxy properties.
- Semi-analytic models robustly predict a rapid increase in the sizes of quiescent galaxies, at a rate that is close to observations. This evolution is largely driven by the growth

and subsequent quenching of starforming galaxies, which evolve in lockstep with their parent halos.

- Galaxies continue to grow in mass and size after quenching. This growth is such that high-mass galaxies lie on a tight mass-size relation, due to repeated merger events. Fewer mergers occur at lower masses, as a result of which the scatter in the mass-size plane is higher.

Galaxy structure can currently be measured accurately, and at rest-frame optical wavelengths, up to $z \approx 2 - 3$. Over the past years it has become clear that, although the $z = 2$ universe is different in many respects, many of the most important galaxy relations were already in place. In the coming years it will become possible to extend these studies to higher redshift, using K band data from either space-based instruments such as the James Webb Telescope, or from adaptive optics-assisted ground-based telescopes. This will open up an interesting epoch to structural measurements, where starforming galaxies still dominated the galaxy population at high-mass.

Our theoretical understanding of the universe is rapidly improving. Both simulations and semi-analytic models are becoming more sophisticated, with the inclusion of complicated gas-based physics and more realistic treatments of star formation. Despite these improvements, many basic observables are still poorly reproduced, especially at high redshift. It is clear that our understanding is still lacking on many basic levels, partially due to the difficulty of comparing precise simulated quantities to more vaguely defined observed properties. Cross-pollination between observers and theorists is of key importance in order to progress in this respect.

Although trends such as size evolution can be measured with good precision and accuracy, selection of galaxy samples for such measurements is not straightforward. The ideal would be to follow the changes in individual galaxies over time. Unfortunately, making a link between progenitor galaxies and their descendants is not trivial. Currently most observational studies are based on mass-limited galaxy samples, since stellar mass is relatively easy to measure and correlates well with many other galaxy properties. However, since galaxies grow with time, redshift trends based on samples selected at constant stellar mass are not equivalent to actual galaxy evolution. Some progress has been made using galaxy samples selected at constant (cumulative) number density. This method is effective at very high stellar masses, where the rank order of galaxies tends to change very little. Finding a reliable way to trace real galaxy growth over a larger mass range is one of the key challenges still facing this field.

CURRICULUM VITAE

I was born on January 6, 1983 in Rehovot, Israel, to an Israeli mother and a Dutch father. When I was 10 months old we moved to Groningen, in the Netherlands, where I spent most of my childhood. When I was 13 years old we moved to Santa Cruz, California. I completed three years at Santa Cruz High School before we moved back to Groningen, where I graduated from the Praedinius Gymnasium in 2000. I spent a year traveling through Europe and Thailand, after which, in 2002, I started studying architecture at the Technische Universiteit Delft. After less than a year I felt a mounting desire to enter the scientific world, and made the choice to switch to astronomy at the Universiteit Leiden.

During my time as a student in Leiden I worked on a variety of interesting research projects. For my bachelor's thesis I studied the possibility of detecting high-velocity stars in the Milky Way using the GAIA satellite (with Dr. Anthony Brown and Dr. Yuri Levin). I obtained my bachelor's degree in 2007. The following year I worked on measuring the rotation curve of a galaxy using the SAURON integral-field spectrograph (with Dr. Annemarie Weijmans and Prof. dr. Tim de Zeeuw). Finally, for my master's thesis I analyzed the effects of measurement biases on future weak lensing surveys (with Dr. Henk Hoekstra).

I was fortunate enough to be selected to participate in two Honours Classes during this time. The first class had as a subject the earliest life on Earth, and was aimed at a multidisciplinary group of students from the Universiteit Leiden and the Vrije Universiteit Amsterdam. As part of this class we traveled to western Australia to investigate 3.5 billion year old fossils of bacterial life. The second class revolved around the possibilities of replicating the photosynthesis processes used by plants and algae for large-scale energy production, and culminated in a week-long workshop at the Lorentz Center at the Universiteit Leiden. Besides these activities, I worked at the science faculty's public outreach office, where I helped organize visits to the university for local high school children.

After obtaining my master's degree in August 2009 I began my doctoral research at the Sterrewacht Leiden, working with Prof. dr. Marijn Franx and Prof. dr. Pieter van Dokkum (Yale University, USA). During this time I attended several conferences, schools, and workshops, and had the opportunity to present my work at a number of institutes. During the first two years of my doctoral work I was a teaching assistant for the "Sterrenkundig Practicum 2" bachelor's course, where I helped students learn the basic skills needed for doing astronomical research, and accompanied them on observing trips to the Isaac Newton Telescope on La Palma (Spain). After this I was a teaching assistant for the "Stralingsprocessen" course, for which I led the problem solving sessions.

My interests have always ranged far and wide. I will not be continuing my astronomical research career, but will instead seek out opportunities outside the academic world.

ACKNOWLEDGEMENTS

Completing a PhD thesis is a long and difficult process, but fortunately it is not something you have to do completely by yourself. Many people have contributed to this work, directly and indirectly, for which I am very grateful.

I am lucky to have been able to work with some very talented people, from whom I have learned a lot. Over the past four years I have learned many valuable lessons from my supervisors, Marijn Franx and Pieter van Dokkum. Marijn's talent to identify issues which seem at first glance to be minor details, but more often than not turned out to be crucially important, is something which continually amazes me. Pieter has been an inexhaustible source of good ideas, and the enjoyment he gets out of scientific research is extremely infectious. Both have taught me to always keep a critical eye on my work, and have impressed upon me the supreme importance of a clear narrative when communicating my results.

These four years would not have been anywhere near as enjoyable if it weren't for all my wonderful colleagues, both in Leiden and abroad. Shannon, Jesse, Adam, Mattia, Willem, Ryan, Moein, and Maaïke have made the galaxies group a great environment to work in, both scientifically and socially. I also want to acknowledge my coauthors, with whom I have greatly enjoyed working. I want to thank Rachel, Tomer, Joel, Nhung, and Erica for making my visits to Yale (as well as our many meetings in Leiden and elsewhere) unforgettable. And I want to thank all my colleagues at the Sterrewacht for many memorable lunches, borrels and coffee breaks.

I am very grateful to all my friends in Rotterdam, Amsterdam and elsewhere, for providing much-needed diversions from work. It is easy to lose touch with everyday life when working on galaxies all day, and I feel fortunate to have such a stimulating group of friends who have always been there to keep my feet on solid ground.

I want to thank my parents, Arpad and Ettie, who have always given me their full support, even when my motives might have been unclear. Without them I would have never gotten to where I am today.

And finally, I thank Hoi Kee. Living with an astronomer is not always easy, and I am supremely grateful for her love, understanding, and patience. Her support and good advice have been invaluable to me.

